

# Helical Organic and Inorganic Polymers

So Hirata,<sup>\*,†</sup> Yasuteru Shigeta,<sup>‡</sup> Sotiris S. Xantheas,<sup>¶</sup> and Rodney J. Bartlett<sup>||</sup>

<sup>†</sup>*Department of Chemistry, University of Illinois at Urbana-Champaign, Urbana, Illinois 61801, USA*

<sup>‡</sup>*Center for Computational Sciences, University of Tsukuba, Tsukuba, Ibaraki 305-8577, Japan*

<sup>¶</sup>*Advanced Computing, Mathematics and Data Division, Pacific Northwest National Laboratory, Richland, Washington 99352, USA*

<sup>§</sup>*Department of Chemistry, University of Washington, Seattle, Washington 98195, USA*

<sup>||</sup>*Quantum Theory Project, University of Florida, Gainesville, Florida 32611, USA*

E-mail: sohirata@illinois.edu

## Abstract

Despite being a staple of synthetic plastics and biomolecules, helical polymers are scarcely studied with Gaussian-basis-set *ab initio* electron-correlated methods on an equal footing with molecules. This article introduces an *ab initio* second-order many-body Green's-function [MBGF(2)] method with nondiagonal, frequency-dependent Dyson self-energy for infinite helical polymers using screw-axis-symmetry-adapted Gaussian-spherical-harmonics basis functions. Together with the Gaussian-basis-set density-functional theory for energies, analytical atomic forces, translational-period force, and helical-angle force, it can compute correlated energy, quasiparticle energy bands, structures, and vibrational frequencies of an infinite helical polymer, which smoothly converge at the corresponding oligomer results. These methods can handle incommensurable structures, which have an infinite translational period and are hard to characterize by any other method, just as efficiently as commensurable structures. We apply them to polyethylene (2/1 helix), polyacetylene (Peierls' system), and polytetrafluoroethylene (13/6 helix) to establish the quantitative accuracy of MBGF(2)/cc-pVDZ in simulating

their (angle-resolved) ultraviolet photoelectron spectra, and of B3LYP/cc-pVDZ or 6-31G\*\* in reproducing their structures, infrared and Raman band positions, phonon dispersions, and (coherent and incoherent) inelastic neutron scattering spectra. We then predict the same properties for infinitely catenated chains of nitrogen or oxygen and discuss their possible metastable existence under ambient conditions. They include planar zigzag polyazene  $(\text{N}_2)_x$  (Peierls' system), 11/3-helical isotactic polyazane  $(\text{NH})_x$ , 9/4-helical isotactic polyfluoroazane  $(\text{NF})_x$ , and 7/2-helical polyoxane  $(\text{O})_x$  as potential high-energy-density materials.

## 1 Introduction

In both chemistry and physics, there is a strong, persistent interest in catenated forms of nitrogen and oxygen, which are only metastable thermodynamically and thus extremely hard to synthesize, detect, or isolate.<sup>1-6</sup> There are multiple reasons for this interest. These elements, which are abundant as atmospheric diatoms, may exist in extended covalently bonded structures under high pressure of planetary interior, which are often predicted to be metallic or even superconducting.<sup>7-10</sup> The fact that they are thermodynamically unstable yet have an appreciable lifetime makes them an ideal candidate for high-energy-density materials (HEDM)<sup>3-6</sup> used as explosives and propellants. They also serve as essential synthetic reagents.<sup>11</sup> However, the interest may ultimately be spurred by the dramatic change<sup>12</sup> in the nature of chemical bonds upon going from stable organic polymers to their isoelectronic inorganic counterparts.<sup>13</sup>

The rapidly decreasing stability of longer catenated nitrogen and oxygen bonds can be rationalized by their bond strengths. The N–N and N=N bonds have binding energies much less than one third and two thirds, respectively, of the N≡N bond, and the O–O bond much less than one half of the O=O bond.<sup>5</sup> These are, in turn, caused by the lone-pair-lone-pair repulsions, which are stronger than the lone-pair-bond-pair or bond-pair-bond-pair repulsions.<sup>14</sup> Consequently, catenated nitrogen and oxygen bonds tend to favor the *gauche* conformation,<sup>14-16</sup> which separates neighboring lone pairs often at the expense of the extra stabilization brought to by the  $\pi$ -electron conjugation of planar structures.

The preferred *gauche* conformation may, in turn, suggest the helical polymeric forms of nitrogen<sup>17</sup> and oxygen<sup>18,19</sup> or the *cubic gauche* (cg) form<sup>20,21</sup> of nitrogen allotrope, in the infinite catenation limit. The latter was achieved synthetically under high pressure by Eremets *et al.*<sup>22,23</sup> Furthermore, intrachain hydrogen bonds may<sup>24</sup> or may not<sup>25</sup> stabilize the helical chains.

However, infinite helical chains have scarcely been computationally explored by *ab initio* electron-correlated methods<sup>26–32</sup> in spite of the ubiquity of helical conformations in both synthetic polymers (e.g., polypropylene, polytetrafluoroethylene, and carbon nanotubes) and biopolymers (e.g., DNA, collagens, and  $\alpha$  helix).<sup>33,34</sup> This, in turn, is caused by the dearth of *ab initio* computational machinery capable of treating infinite chains under helical periodic boundary conditions (see, however, pioneering empirical or semiempirical methods<sup>35–37</sup> and *ab initio* method<sup>38–52</sup> including Gaussian-basis-set DFT).

On the one hand, molecular methods and software can be applied to longer helical oligomers to extract bulk properties.<sup>53</sup> However, not only are such calculations saddled with slowly decaying terminal effects and inefficient, but they have difficulties determining the equilibrium helical angle or quasiparticle energy bands as a function of wave vector. On the other hand, three-dimensional solid-state methods and software can handle a crystalline phase of helical polymers. This too is not ideal, as it imposes severe constraints on the helical angle so that the translational repeat unit does not become too large. For example, polytetrafluoroethylene adopts a 13/6 helical conformation<sup>54</sup> in the translational notation,<sup>55</sup> meaning that the three-dimensional translational periodic unit must contain at least 13 CF<sub>2</sub> groups per chain (see, e.g., Ref.<sup>56</sup> for a calculation using such a large translational unit) as opposed to just one CF<sub>2</sub> rototranslational repeat unit under helical periodic boundary conditions. It would be exceedingly difficult to optimize the helical angle using a method exploiting linear translational symmetry. Furthermore, there is no *a priori* reason for a helix to adopt a commensurable structure,<sup>57</sup> and it is possible that the translational period is infinity. Also, solid-state and molecular methods often use disparate basis sets and incompatible approximations, creating a gap in computational characterization between the short- and long-chain limits.

The objective of this study is three-fold:

First, we introduce an *ab initio* second-order many-body Green’s-function [MBGF(2)] method<sup>58–88</sup> with nondiagonal, frequency-dependent Dyson self-energy for infinite helical polymers. By using screw-axis-symmetry-adapted Gaussian-spherical-harmonics basis functions, the method expands the Bloch factor of a crystal orbital as a linear combination of these functions centered in the single smallest rototranslational (i.e., physical) repeat unit.<sup>89</sup> Together with the screw-axis-symmetry-adapted Gaussian-basis-set density-functional theory (DFT) for analytical gradients,<sup>52</sup> it permits the determination of smooth, continuous quasiparticle energy bands and density of states (DOS), following the optimization of all structural parameters including helical angle and translational period. These results can be directly compared with those obtained from the Gaussian-basis-set *ab initio* electron-correlated and DFT calculations for molecules.

Second, we apply these methods to three experimentally most thoroughly characterized hydrocarbon or fluorocarbon polymers: polyethylene (CH<sub>2</sub>)<sub>x</sub>, polyacetylene (C<sub>2</sub>H<sub>2</sub>)<sub>x</sub>, and polytetrafluoroethylene (CF<sub>2</sub>)<sub>x</sub>. These calculations establish the quantitative accuracy of the MBGF(2) method with the cc-pVDZ basis set for valence bands and electronic DOS and of DFT using the Becke3–Lee–Yang–Parr (B3LYP) hybrid functional with the cc-pVDZ or 6-31G\*\* basis set for the structure parameters, phonon dispersion, and phonon DOS, as judged by the comparison with their crystallographies, (angle-resolved) ultraviolet photoelectron spectra, infrared (IR) and Raman band positions, and (coherent or incoherent) inelastic neutron scattering (INS) spectra.

Third, we predict the structure parameters, phonon dispersion, phonon DOS, valence bands, and electronic DOS of infinite nitrogen and oxygen polymers. The polymers considered in this study are linear, zigzag, planar all-*trans* polyazene (N<sub>2</sub>)<sub>x</sub>, helical isotactic polyazane (NH)<sub>x</sub>, helical isotactic polyfluoroazane (NF)<sub>x</sub>, and helical polyoxane (O)<sub>x</sub>. They are nitrogen or oxygen analogues of polyacetylene, polyethylene, polytetrafluoroethylene, and polyethylene, respectively. We discuss their thermodynamic and kinetic stability and thus possible metastable existence under ambient conditions. We present the predicted IR and Raman band positions, INS spectra, and photoelectron spectra of these hypothetical polymers with the aim of assisting in their identification.



## 2 Methods

### 2.1 Hybrid density-functional method for helical polymers

One of the present authors recently reported a Gaussian-basis-set hybrid DFT method for energies and analytical energy gradients of a closed-shell infinite helical polymer, in which the quadrature derivatives were shown to persist in the translational-period and helical-angle gradients even in the limit of an infinitely dense grid.<sup>52</sup> See Refs.<sup>38,41,42,44,47,48,50,51</sup> for earlier Gaussian-basis-set crystal-orbital methods for helices. The formalism encompasses the spin-restricted Hartree–Fock (HF) method for helical polymers, furnishing a reference wave function for MBGF(2) described in Sec. 2.2. We succinctly summarize the salient parts of the formalism.

The  $n$ th rototranslational (physical) repeat unit<sup>89</sup> is axially translated by period or “rise”<sup>90</sup>  $a$  as it is rotated counterclockwise by angle or “twist”<sup>90</sup>  $\varphi$  to form the  $(n+1)$ th unit cell. An  $m/n$  helix in the translational notation<sup>55</sup> (an  $m_n$  helix in the rotational notation<sup>55</sup>) means that  $m$  repeat units make  $n$  complete turns and, therefore,  $\varphi = 2\pi n/m$ . The  $I$ th atomic coordinates of the  $n$ th unit  $(X_{I(n)}, Y_{I(n)}, Z_{I(n)})$  are then related to those in the zeroth unit cell  $(X_{I(0)}, Y_{I(0)}, Z_{I(0)})$  by

$$X_{I(n)} = X_{I(0)} + na, \quad (1)$$

$$Y_{I(n)} = Y_{I(0)} \cos n\varphi - Z_{I(0)} \sin n\varphi, \quad (2)$$

$$Z_{I(n)} = Y_{I(0)} \sin n\varphi + Z_{I(0)} \cos n\varphi, \quad (3)$$

where the chain is along the  $x$  axis.

In our formalism, we use three sets of atom-centered Gaussian basis functions,  $\{\chi_{\nu(n)}(\mathbf{r})\}$ ,  $\{\tilde{\chi}_{\nu(n)}(\mathbf{r})\}$ , and  $\{\bar{\chi}_{\nu(n)}(\mathbf{r})\}$ , where  $\nu(n)$  denotes the  $\nu$ th contracted Gaussian basis function in the  $n$ th unit cell. (In practice, however, only one Gaussian basis set, such as 6-31G\*\* or cc-pVDZ, needs to be specified.) The first set,  $\{\chi_{\nu(n)}(\mathbf{r})\}$ , consists of Gaussian basis functions with Cartesian six  $d$  and ten  $f$  functions (if applicable) defined in the laboratory Cartesian coordinates; its members are not reoriented according to the screw-axis symmetry, but only their centers are translated-rotated

along the chain. The second set,  $\{\tilde{\chi}_{v(n)}(\mathbf{r})\}$ , is composed of screw-axis-symmetry-adapted (i.e., re-orienting) Gaussian basis functions with Cartesian six  $d$  and ten  $f$  functions; its members in the  $n$ th unit cell are oriented in the  $n$ th cell's Cartesian coordinates, whose  $y$  and  $z$  axes are rotated counterclockwise by angle  $n\varphi$  (relative to the zeroth cell). The third set,  $\{\bar{\tilde{\chi}}_{v(n)}(\mathbf{r})\}$ , is the same as the second set except that it has spherical five  $d$  and seven  $f$  functions (if applicable). The corresponding molecular integrals and expansion coefficients are decorated by a tilde and/or overbar.

Since the Bloch theorem<sup>91</sup> should hold only for a screw-axis-symmetry-adapted basis set, the generalized eigenvalue equation to be solved for the crystal-orbital coefficients,  $\bar{\tilde{C}}_{vp}(k)$ , and orbital energy,  $\epsilon_p(k)$ , is given by

$$\sum_{\nu} \bar{\tilde{F}}_{\mu\nu}(k) \bar{\tilde{C}}_{\nu p}(k) = \sum_{\nu} \bar{\tilde{S}}_{\mu\nu}(k) \bar{\tilde{C}}_{\nu p}(k) \epsilon_p(k), \quad (4)$$

where  $p$  is an energy band index,  $k$  is a wave vector,  $\bar{\tilde{F}}_{\mu\nu}(k)$  and  $\bar{\tilde{S}}_{\mu\nu}(k)$  are the  $\mu\nu$ th element of the Kohn–Sham (KS) Hamiltonian (or Fock) dynamical matrix and overlap dynamical matrix, respectively, whereas  $\mu$  and  $\nu$  label screw-axis-symmetry-adapted Gaussian basis functions with spherical  $d$  and  $f$  functions (the third basis set). These matrices are formed by transformation of the corresponding matrices,  $\tilde{F}_{\mu\nu}(k)$  and  $\tilde{S}_{\mu\nu}(k)$ , in the screw-axis-symmetry-adapted Gaussian basis functions with Cartesian  $d$  and  $f$  functions (the second basis set).

$$\bar{\tilde{F}}_{\mu\nu}(k) = \sum_{\mu', \nu'} Q_{\mu\mu'} Q_{\nu\nu'} \tilde{F}_{\mu'\nu'}(k), \quad (5)$$

$$\bar{\tilde{S}}_{\mu\nu}(k) = \sum_{\mu', \nu'} Q_{\mu\mu'} Q_{\nu\nu'} \tilde{S}_{\mu'\nu'}(k). \quad (6)$$

See Ref.<sup>52</sup> for the transformation matrix,  $Q_{\mu\mu'}$ . The crystal-orbital coefficients in the the second basis set are obtained as

$$\tilde{C}_{vm}(k) = \sum_{\nu'} \bar{\tilde{C}}_{\nu'm}(k) Q_{\nu'\nu}. \quad (7)$$

The dynamical (i.e., reciprocal-space) matrices are constructed from the corresponding, real-

space matrices by

$$\tilde{F}_{\mu\nu}(k) = \sum_{n=-S}^S \tilde{F}_{\mu(0)\nu(n)} e^{2\pi i n k / K}, \quad (8)$$

$$\tilde{S}_{\mu\nu}(k) = \sum_{n=-S}^S \tilde{S}_{\mu(0)\nu(n)} e^{2\pi i n k / K}, \quad (9)$$

for wave vector index (integer) in the range of  $0 \leq k < K$ , summing over unit cells in the range of  $-S \leq n \leq S$ , where  $K$  is the number of wave vector sampling points in the reciprocal unit cell and  $S$  is the so-called short-range Namur lattice-sum cutoff.<sup>92</sup>  $\tilde{F}_{\mu(0)\nu(n)}$  and  $\tilde{S}_{\mu(0)\nu(n)}$  stand for, respectively, the KS Hamiltonian (or Fock) and overlap matrix elements between the  $\mu$ th Gaussian basis function in the zeroth unit cell and the  $\nu$ th Gaussian basis function in the  $n$ th unit cell, the latter being reorientated by angle  $n\varphi$ .

The latter matrices in the basis of the screw-axis-symmetry-adapted (i.e., reorienting) Gaussian basis functions are, in turn, obtained by transformation of those in the basis of non-reorienting Gaussian basis functions,  $\{\chi_{\nu(n)}(\mathbf{r})\}$ , in the first basis set:

$$\tilde{F}_{\mu(0)\nu(n)} = \sum_{\nu'} R_{\nu\nu'}(n) F_{\mu(0)\nu'(n)}, \quad (10)$$

$$\tilde{S}_{\mu(0)\nu(n)} = \sum_{\nu'} R_{\nu\nu'}(n) S_{\mu(0)\nu'(n)}, \quad (11)$$

where, for instance, the overlap matrix element in the right-hand side is defined by

$$S_{\mu(0)\nu(n)} = \int d\mathbf{r} \chi_{\mu(0)}^*(\mathbf{r}) \chi_{\nu(n)}(\mathbf{r}), \quad (12)$$

with  $\chi_{\nu(n)}(\mathbf{r})$  being the  $\nu$ th Gaussian basis function in the  $n$ th unit cell in the laboratory Cartesian coordinates. Such an integral can be computed by the standard algorithms.<sup>93</sup> See Ref.<sup>52</sup> for the evaluation of  $F_{\mu(0)\nu'(n)}$ , which can include the multipole-expansion correction.<sup>92</sup> The transformation matrix,  $R_{\nu\nu'}(n)$ , is also given in the same article.<sup>52</sup>

With  $R_{\nu\nu'}(n)$ , the crystal-orbital coefficients in the first basis set are then obtained by transfor-

mation,

$$C_{vp}(k; n) = \sum_{v'} \tilde{C}_{v'p}(k) R_{v'v}(n). \quad (13)$$

Note that  $C_{vp}(k; n)$  are no longer translationally invariant and vary with the unit-cell index  $n$ .

See Ref.<sup>52</sup> for a complete formulation of the hybrid DFT energies and analytical gradients for infinite helical polymers. Quadrature derivatives are essential for analytical gradients with respect to the translational period and helical angle.

## 2.2 Second-order many-body Green's-function method for helical polymers

In a closed-shell infinite helical polymer, whose Bloch orbitals are expanded by  $n$  basis functions per rototranslational (physical) repeat unit,<sup>89</sup> its one-particle many-body Green's function<sup>58–88</sup> is an  $n$ -by- $n$  matrix defined by its elements as

$$\begin{aligned} G_{pq}(\omega; k) = & \sum_{\mu} \frac{\langle \Psi_{N,0} | \hat{p}_k^\dagger | \Psi_{N-1,\mu} \rangle \langle \Psi_{N-1,\mu} | \hat{q}_k | \Psi_{N,0} \rangle}{\omega - E_{N,0} + E_{N-1,\mu}} \\ & + \sum_{\mu} \frac{\langle \Psi_{N,0} | \hat{q}_k | \Psi_{N+1,\mu} \rangle \langle \Psi_{N+1,\mu} | \hat{p}_k^\dagger | \Psi_{N,0} \rangle}{\omega - E_{N+1,\mu} + E_{N,0}}. \end{aligned} \quad (14)$$

Here,  $\Psi_{N,0}$  is the exact, ground-state wave function with  $N$  electrons having the exact energy  $E_{N,0}$ ,  $\Psi_{N\pm 1,\mu}$  is the exact,  $\mu$ th-state wave function with  $N \pm 1$  electrons and exact energy  $E_{N\pm 1,\mu}$ , and  $\hat{p}_k^\dagger$  and  $\hat{q}_k$  are electron creation and annihilation operators, respectively, in the  $p$ th and  $q$ th energy bands with wave vector  $k$ . The Green's function diverges whenever  $\omega$  coincides with an exact electron-binding energy.

Replacing the exact wave functions and energies in Eq. (14) by their corresponding quantities of a mean-field method, such as the HF method, we obtain the zeroth-order Green's function. It simplifies to

$$G_{pq}^{(0)}(\omega; k) = \frac{\delta_{pq}}{\omega - \epsilon_p(k)}, \quad (15)$$

where  $\epsilon_p(k)$  is the mean-field one-electron energy of the  $p$ th energy band with wave vector  $k$  obtained by solving Eq. (4). Starting with this reference Green's function as the zeroth order, we expand the exact Green's function of Eq. (14) in the so-called Feynman–Dyson perturbation series.<sup>88</sup>

Before doing so, let us define an  $n$ -by- $n$  matrix known as the Dyson self-energy,  $\Sigma(\omega; k)$ , by the equation,

$$\mathbf{G}(\omega; k) = \mathbf{G}^{(0)}(\omega; k) + \mathbf{G}^{(0)}(\omega; k)\Sigma(\omega; k)\mathbf{G}(\omega; k). \quad (16)$$

We seek  $\omega$ 's that make the exact Green's function divergent, which is where the determinant of its inverse becomes zero.

$$0 = |\{\mathbf{G}(\omega; k)\}^{-1}| \quad (17)$$

$$= |\{\mathbf{G}^{(0)}(\omega; k)\}^{-1} - \Sigma(\omega; k)| \quad (18)$$

$$= |\omega\mathbf{1} - \boldsymbol{\epsilon}(k) - \Sigma(\omega; k)|. \quad (19)$$

The roots of this equation are, in turn, the solutions of the  $n$ -by- $n$  matrix eigenvalue equation,

$$\{\boldsymbol{\epsilon}(k) + \Sigma(\omega_q; k)\}\mathbf{U}_q(k) = \omega_q(k)\mathbf{U}_q(k), \quad (20)$$

where  $\boldsymbol{\epsilon}(k)$  is the diagonal matrix of  $\epsilon_p(k)$ ,  $\omega_q(k)$  is the  $q$ th eigenvalue, and  $\mathbf{U}_q(k)$  is the  $q$ th eigenvector. One can view this equation, known as the inverse Dyson equation, as an effective one-electron equation, akin to the Hartree–Fock–Roothaan or Kohn–Sham equation, with  $\Sigma(\omega_q; k)$  serving as the one-electron correlation potential, which is nonlocal and frequency-dependent. Owing to the frequency-dependence, there are much more than  $n$  roots in this  $n$ -by- $n$  matrix eigenvalue equation, and these roots,  $\omega_q(k)$ , form the exact quasiparticle energy bands as a function of wave vector  $k$  for Koopmans' as well as non-Koopmans' (satellite or shake-up) states. The corresponding eigenvector  $\mathbf{U}_q(k)$  defines a Dyson orbital.<sup>94</sup>

There are widely used approximations to the self-energy. In the diagonal approximation,<sup>95</sup> we neglect all the off-diagonal elements of  $\Sigma(\omega_q; k)$ , turning the matrix eigenvalue equation into a polynomial equation,

$$\epsilon_q(k) + \Sigma_{qq}(\omega_q; k) = \omega_q(k), \quad (21)$$

whose Dyson orbital becomes just the orbital of the reference mean-field method; i.e.,  $U_q(k)$  is a unit vector. In the diagonal, frequency-independent approximation,<sup>95–98</sup> the electron-binding energy is obtained by a one-time evaluation of the left-hand side of the following equation:

$$\epsilon_q(k) + \Sigma_{qq}(\epsilon_q; k) = \omega_q(k), \quad (22)$$

at the expense of losing roots for non-Koopmans' states. This approximation is equivalent to the  $\Delta\text{MP}n$  method for  $1 \leq n \leq 3$ .<sup>87,88,99</sup> The use of neither approximation is denoted the “full” self-energy in this article.

The residue of the Green's function gives the weight of one-electron character in the electron-detachment or attachment transition, to which photoelectron cross section is proportional. Using the following relationship implied by Eq. (19),

$$G_{qq}(\omega; k) = \frac{1}{U_q^\dagger(k) \{ \omega \mathbf{1} - \epsilon(k) - \Sigma(\omega; k) \} U_q(k)}, \quad (23)$$

we can evaluate the residue as<sup>94</sup>

$$\begin{aligned} & \text{Res}_{\omega_q} G_{qq}(\omega; k) \\ &= \lim_{\omega \rightarrow \omega_q} (\omega - \omega_q) G_{qq}(\omega; k) \end{aligned} \quad (24)$$

$$= \lim_{\omega \rightarrow \omega_q} \frac{\omega - \omega_q}{\mathbf{U}_q^\dagger(k) \{ \omega \mathbf{1} - \boldsymbol{\epsilon}(k) - \boldsymbol{\Sigma}(\omega; k) \} \mathbf{U}_q(k)} \quad (25)$$

$$= \lim_{\omega \rightarrow \omega_q} \frac{(\partial/\partial\omega)(\omega - \omega_q)}{(\partial/\partial\omega) \mathbf{U}_q^\dagger(k) \{ \omega \mathbf{1} - \boldsymbol{\epsilon}(k) - \boldsymbol{\Sigma}(\omega; k) \} \mathbf{U}_q(k)} \quad (26)$$

$$= \left\{ 1 - \mathbf{U}_q^\dagger(k) \frac{\partial \boldsymbol{\Sigma}(\omega; k)}{\partial \omega} \Big|_{\omega=\omega_q} \mathbf{U}_q(k) \right\}^{-1}. \quad (27)$$

In Eq. (26), L'Hôpital's rule was used. The derivatives of  $\mathbf{U}_q$  need not be taken in Eq. (27) by virtue of the Hellmann–Feynman theorem.

In the diagonal approximation, Eq. (27) simplifies<sup>94</sup> to

$$\text{Res}_{\omega_q} G_{qq}(\omega; k) = \left\{ 1 - \frac{\partial \Sigma_{qq}(\omega; k)}{\partial \omega} \Big|_{\omega=\omega_q} \right\}^{-1}, \quad (28)$$

which can still discern Koopmans' roots from non-Koopmans' ones. In the diagonal, frequency-independent approximation, only Koopmans' roots exist, and therefore,

$$\text{Res}_{\omega_q} G_{qq}(\omega; k) = 1. \quad (29)$$

We adopt the second-order Feynman–Dyson perturbation approximation to the self-energy,<sup>88</sup>

$$\boldsymbol{\Sigma}(\omega; k) \approx \boldsymbol{\Sigma}^{(1)}(\omega; k) + \boldsymbol{\Sigma}^{(2)}(\omega; k). \quad (30)$$

With the canonical HF reference, which corresponds to the Møller–Plesset partitioning of the Hamiltonian, the first-order correction vanishes:

$$\Sigma_{pq}^{(1)}(\omega; k) = 0. \quad (31)$$

The second-order correction is given by

$$\begin{aligned} \Sigma_{pq}^{(2)}(\omega; k) = & \sum_j^{\text{occ.}} \sum_{a,b}^{\text{vir.}} \sum_{k_j, k_b} \frac{2\langle q(k)a(k_a)|j(k_j)b(k_b)\rangle\langle p(k)a(k_a)|j(k_j)b(k_b)\rangle^* - \langle q(k)a(k_a)|j(k_j)b(k_b)\rangle\langle j(k_j)a(k_a)|p(k)b(k_b)\rangle^*}{\omega + \epsilon_j(k_j) - \epsilon_a(k_a) - \epsilon_b(k_b)} \\ & + \sum_{i,j}^{\text{occ.}} \sum_b^{\text{vir.}} \sum_{k_j, k_b} \frac{2\langle i(k_i)p(k)|j(k_j)b(k_b)\rangle\langle i(k_i)q(k)|j(k_j)b(k_b)\rangle^* - \langle i(k_i)p(k)|j(k_j)b(k_b)\rangle\langle j(k_j)q(k)|i(k_i)b(k_b)\rangle^*}{\omega + \epsilon_b(k_b) - \epsilon_i(k_i) - \epsilon_j(k_j)}, \end{aligned} \quad (32)$$

where  $i$  and  $j$  run over occupied (valence) energy bands,  $a$  and  $b$  over virtual (conduction) energy bands,  $p$  and  $q$  stand for any energy band, and  $k_j$  and  $k_b$  run over  $K$  evenly spaced wave vector sampling points in the reciprocal unit cell, whereas  $k_a$  and  $k_i$  are, in turn, determined by the momentum conservation law:

$$k + k_j \equiv k_a + k_b \pmod{K}, \quad (33)$$

$$k_i + k_j \equiv k + k_b \pmod{K}. \quad (34)$$

Each bracket denotes a two-electron integral (in the Mulliken notation) in the basis of crystal (Bloch) orbitals, which is obtained by transformation of the same in the Gaussian basis set. Using  $\mu$ ,  $\nu$ ,  $\kappa$ , and  $\lambda$  as labels for the Gaussian basis functions in the first basis set (i.e., defined in the laboratory Cartesian coordinates), we can write the transformation as

$$\begin{aligned} & \langle p(k_p)q(k_q)|r(k_r)s(k_s)\rangle \\ &= \frac{1}{K} \sum_{\mu, \nu, \kappa, \lambda} \sum_{m_1=-S}^S \sum_{m_2=-L}^L \sum_{m_3=m_2-S}^{m_2+S} \\ & \times C_{\mu p}^*(k_p; 0) C_{\nu q}(k_q; m_1) C_{\kappa r}^*(k_r; m_2) C_{\lambda s}(k_s; m_3) \\ & \times e^{2\pi i(m_1 k_q - m_2 k_r + m_3 k_s)/K} \langle \mu(0) \nu(m_1) | \kappa(m_2) \lambda(m_3) \rangle, \end{aligned} \quad (35)$$

where  $S$  and  $L$  stand for the short- and long-range lattice-sum cutoffs according to the Namur



protocol,<sup>92</sup> and  $K$  is the number of wave vector sampling points, and

$$\langle \mu(0) \nu(m_1) | \kappa(m_2) \lambda(m_3) \rangle = \iint d\mathbf{r}_1 d\mathbf{r}_2 \frac{\chi_{\mu(0)}^*(\mathbf{r}_1) \chi_{\nu(m_1)}(\mathbf{r}_1) \chi_{\kappa(m_2)}^*(\mathbf{r}_2) \chi_{\lambda(m_3)}(\mathbf{r}_2)}{|\mathbf{r}_1 - \mathbf{r}_2|}. \quad (36)$$

The above integral can be evaluated by the standard algorithms<sup>93</sup> since the Gaussian basis functions  $\chi_{\nu(m)}(\mathbf{r})$  are defined in the laboratory Cartesian coordinates, whereas  $C_{\nu q}(k_q; m)$  is given by Eq. (13).

The derivative of the self-energy needed for computing the residue [Eq. (27)] is obtained analytically as

$$\begin{aligned} \frac{\partial \Sigma_{pq}^{(2)}(\omega; k)}{\partial \omega} = & - \sum_j^{\text{occ.}} \sum_{a,b}^{\text{vir.}} \sum_{k_j, k_b} \frac{2 \langle q(k) a(k_a) | j(k_j) b(k_b) \rangle \langle p(k) a(k_a) | j(k_j) b(k_b) \rangle^* - \langle q(k) a(k_a) | j(k_j) b(k_b) \rangle \langle j(k_j) a(k_a) | p(k) b(k_b) \rangle^*}{\{\omega + \epsilon_j(k_j) - \epsilon_a(k_a) - \epsilon_b(k_b)\}^2} \\ & - \sum_{i,j}^{\text{occ.}} \sum_b^{\text{vir.}} \sum_{k_j, k_b} \frac{2 \langle i(k_i) p(k) | j(k_j) b(k_b) \rangle \langle i(k_i) q(k) | j(k_j) b(k_b) \rangle^* - \langle i(k_i) p(k) | j(k_j) b(k_b) \rangle \langle j(k_j) q(k) | i(k_i) b(k_b) \rangle^*}{\{\omega + \epsilon_b(k_b) - \epsilon_i(k_i) - \epsilon_j(k_j)\}^2}. \end{aligned} \quad (37)$$

Also, as we compute  $\Sigma^{(2)}(\omega; k)$ , we simultaneously obtain the second-order many-body perturbation [MBPT(2)] correction to energy per unit cell as<sup>96–98,100–112</sup>

$$E^{(2)} = \frac{1}{K} \sum_{i,j}^{\text{occ.}} \sum_{a,b}^{\text{vir.}} \sum_{k_i, k_j, k_a} \frac{2 \langle i(k_i) a(k_a) | j(k_j) b(k_b) \rangle \langle i(k_i) a(k_a) | j(k_j) b(k_b) \rangle^* - \langle i(k_i) a(k_a) | j(k_j) b(k_b) \rangle \langle j(k_j) a(k_a) | i(k_i) b(k_b) \rangle^*}{\epsilon_i(k_i) + \epsilon_j(k_j) - \epsilon_a(k_a) - \epsilon_b(k_b)}, \quad (38)$$

where  $k_b$  is determined by the momentum conservation law:

$$k_i + k_j \equiv k_a + k_b \pmod{K}. \quad (39)$$

Equations (32), (37), and (38) are expressed in the forms that are conducive to parallelized summation loops over the crystal-orbital (band) index  $b$  and wave-vector index  $k_b$ .

The computational cost is dominated by the integral transformation of Eq. (35), which is carried out as four consecutive quarter transformations. Their nominal cost scales as  $O(N^5 S^2 L K)$ , where  $N$  is the number of basis functions,  $S$  and  $L$  are the short- and long-range lattice-sum cutoffs of the Namur protocol, and  $K$  is the number of wave vectors. However, this cost function may only serve as an upper limit because integrals in the Gaussian basis functions are aggressively distance-based

screened with only a few percent of the total number evaluated and stored. Furthermore, the value of  $K$  used in the MBGF(2) step is smaller than that in the preceding HF step by a factor of  $n$  in the mod- $n$  approximation adopted here.<sup>110,111</sup>

See Ref.<sup>88</sup> for a comprehensive treatise of MBGF( $n$ ) at any  $n$ .

### 3 Results and Discussion

#### 3.1 Polyethylene, $(\text{CH}_2)_x$

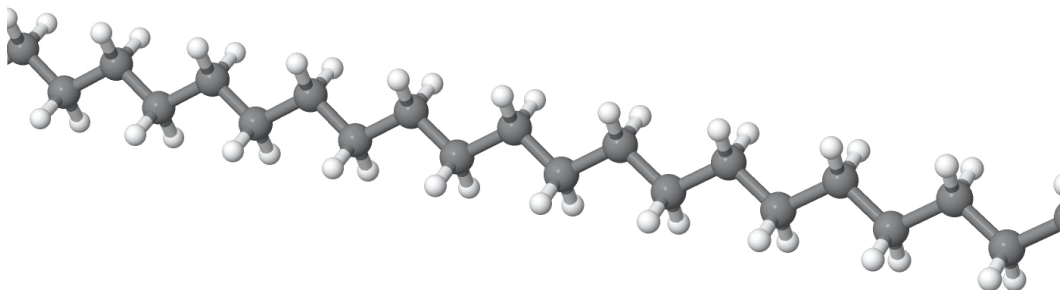


Figure 1: Polyethylene,  $(\text{CH}_2)_x$ .

Polyethylene (Fig. 1) is the one of the most produced plastics. It is thermodynamically and air stable. It is a linear zigzag chain with the  $\text{C}_2\text{H}_4$  translational repeat unit or a 2/1 helix with the  $\text{CH}_2$  rototranslational (physical) repeat unit with the helical angle of  $\varphi = 180^\circ$ .<sup>89</sup> Its electronic,<sup>113,114</sup> structural,<sup>115</sup> and vibrational<sup>116–121</sup> properties have been thoroughly characterized experimentally. They are also computationally reproduced accurately.<sup>98,111,122</sup>

In this subsection, therefore, we briefly confirm the predictive accuracy of the B3LYP/cc-pVDZ and 6-31G\*\* methods for structures, IR and Raman band positions, and phonon dispersions and phonon DOS as well as of MBGF(2)/cc-pVDZ for valence electronic bands and DOS. The B3LYP functional<sup>123</sup> is the version that used the VWN5 functional.<sup>124</sup> All calculations were performed under the helical periodic boundary conditions employing POLYMER,<sup>125</sup> with  $S = 8$ ,  $L = 12$ ,  $K = 48$  and the frozen-core and mod-6 approximations for MBGF(2)<sup>110,111</sup> using a  $\text{CH}_2$  group as the rototranslational (physical) repeat unit. During the latter calculation, we also obtained the MBPT(2)

correction to the energy per unit cell. See Sec. 2 for the details of these methods and the definitions of the computational parameters (such as  $S$ ,  $L$ , and  $K$ ). Harmonic force constants were computed for up to the ninth nearest neighbor  $\text{CH}_2$  groups by the supercell method,<sup>126</sup> using NWChem.<sup>127</sup>

The phonons of the 2/1 helix of polyethylene are optically active at the phase angles of  $\theta = 0$  and  $180^\circ$  in the phonon dispersion for a  $\text{CH}_2$  rototranslational (physical) repeat unit<sup>89</sup> (i.e., in the extended-zone scheme<sup>128</sup>). This may be understood as they all map onto  $\theta = 0$  in the phonon dispersion for a  $\text{C}_2\text{H}_4$  translational repeat unit (in the true-zone scheme<sup>128</sup>). With these phase angles, the phonons have null linear momenta and can satisfy the momentum conservation law with photons with minuscule linear momenta during their optical (de)excitations. See Sec. 3.3 for a more general discussion on the IR/Raman selection rules and various Brillouin-zone schemes of an infinite helical polymer.

INS spectroscopy obeys completely different selection rules.<sup>129</sup> Since thermal neutrons have linear momenta comparable to those of phonons, INS probes phonons of all momenta (phase angles). The scattering cross section is by far the largest for hydrogen motions because a momentum transfer is the most facile between particles with near-equal masses. Incoherent INS spectroscopy, therefore, measures the phonon DOS weighted by hydrogen amplitudes. Coherent INS spectroscopy can further discern the momentum transfer of each transition and report the phonon dispersion curves as a function of the phonon momentum.

Table 1: Structural parameters of  $(\text{CH}_2)_x$  and  $\text{C}_2\text{H}_4$ .

Method	$(\text{CH}_2)_x$					$\text{C}_2\text{H}_4^a$		
	$r(\text{CC})$	$r(\text{CH})$	$a(\text{CCC})$	$a(\text{HCH})$	$\varphi^b$	$r(\text{CC})$	$r(\text{CH})$	$a(\text{HCH})$
B3LYP/6-31G**	1.534 Å	1.100 Å	113.6°	105.9°	180.0°	1.330 Å	1.087 Å	116.3°
B3LYP/cc-pVDZ	1.533 Å	1.107 Å	113.7°	105.8°	180.0°	1.334 Å	1.095 Å	116.5°
Observed <sup>c</sup>	1.533 Å	1.07 Å	111.9°	107°	180.0°	1.339 Å	1.086 Å	117.6°

<sup>a</sup>Ethylene. <sup>b</sup>The helical angle [Eqs. (1)–(3)]. <sup>c</sup>The polyethylene structure from Teare.<sup>130</sup> The ethylene structure from Herzberg.<sup>131</sup>

Table 1 compiles the internal coordinates of the equilibrium structure of polyethylene and its monomer, ethylene, determined by the B3LYP/cc-pVDZ and 6-31G\*\* methods. The basis-set dependence is negligible and the bond lengths and angles are reproduced within a few hundredths

of one Ångstrom and a few degrees, respectively, of the experimental data. The methods can, therefore, be considered predictive for structures.

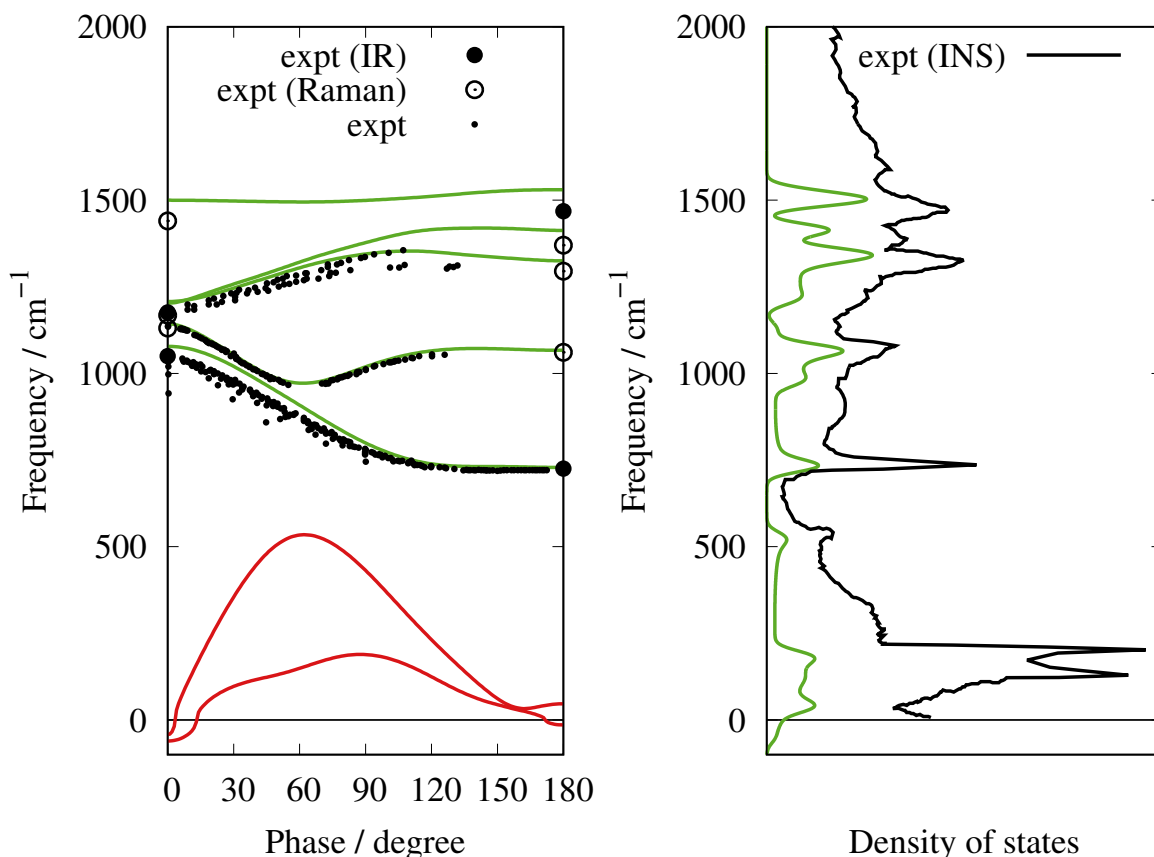


Figure 2: Phonon dispersion curves and DOS of  $(\text{CH}_2)_x$  computed by B3LYP/6-31G\*\* in the extended-zone scheme (i.e., corresponding to a  $\text{CH}_2$  group as the repeat unit). The DOS is convoluted with a Gaussian of a FWHM of  $40 \text{ cm}^{-1}$ . The experimental phonon dispersion curves from Snyder and Schachtschneider.<sup>120</sup> The IR data from Krimm *et al.*<sup>116</sup> and from Nielsen and Holland.<sup>118</sup> The Raman data from Nielsen and Woollett<sup>117</sup> and from Brown.<sup>119</sup> The incoherent inelastic neutron scattering (INS) spectrum from Parker.<sup>121</sup>

Figure 2 compares the calculated phonon dispersion and phonon DOS with the observed IR and Raman band positions<sup>116,118,119</sup> and INS spectrum.<sup>121</sup> Phonon dispersion curves deduced from experimental data of *n*-alkanes are also overlaid.<sup>120</sup> As established already,<sup>122</sup> B3LYP/6-31G\*\* reproduces the nonmonotonic shapes of the phonon dispersions in the fingerprint region remarkably well. The calculated phonon DOS (without the hydrogen-amplitude weighting in this case) also provides unmistakable assignments of all major peaks in the observed INS spectrum.<sup>121</sup> The errors in the calculated peak positions are insignificant in light of the intrinsic difficulty of determining

thermal neutron energies precisely.

Note that the distance-based truncation of the force-constant matrices results in a loss of the strict translational and rotational invariance, causing the acoustic branches (the red curves in Fig. 2) to not converge exactly at zero frequencies at  $\theta = 0$  and  $180^\circ$  as they should theoretically. The errors can reach  $61i \text{ cm}^{-1}$  at  $\theta = 0$  and  $47 \text{ cm}^{-1}$  at  $\theta = 180^\circ$  despite the fact that force constants for up to the ninth nearest neighbor  $\text{CH}_2$  groups on both sides of the zeroth unit cell were taken into account. Since polyethylene is fully established to have a planar zigzag backbone in its equilibrium structure, an imaginary frequency of this size does not imply a saddle point of the potential energy surface.

Table 2: Vibrational frequencies (in  $\text{cm}^{-1}$ ) of  $(\text{CH}_2)_x$ .

Irrep. <sup>a</sup> ; phase; activity	B3LYP/6-31G**	Observed <sup>b</sup>
$A_g$ ; $\theta = 0$ ; Raman	3008.7	2848
	1499.7	1440
	1142.9	1131
$B_{1g}$ ; $\theta = \varphi$ ; Raman	1412.4	1370
	1066.6	1061
$B_{2g}$ ; $\theta = \varphi$ ; Raman	1324.7	1295
$B_{3g}$ ; $\theta = 0$ ; Raman	3026.1	2883
	1207.2	1168
$A_u$ ; $\theta = 0$ ; IR	1078.0	1050
$B_{1u}$ ; $\theta = \varphi$ ; IR	3072.8	2919
	728.6	725
$B_{2u}$ ; $\theta = \varphi$ ; IR	3023.6	2851
	1530.0	1468
$B_{3u}$ ; $\theta = 0$ ; IR	1202.6	1176

<sup>a</sup>Isomorphic to the  $D_{2h}$  point group.  $\varphi$  is the helical angle. <sup>b</sup>The IR data from Krimm *et al.*<sup>116</sup> and from Nielsen and Holland.<sup>118</sup> The Raman data from Nielsen and Woollett<sup>117</sup> and from Brown.<sup>119</sup>

Table 2 makes a more detailed comparison of the calculated and observed frequencies of the IR and Raman bands. Without scaling of frequencies,<sup>122</sup> the calculated and observed data in the fingerprint region agree with each other within  $62 \text{ cm}^{-1}$  or usually much more closely. Since the observed bands are separated from one another more widely, reliable assignments can be made on the basis of the calculated phonon frequencies and symmetry alone. However, unsurprisingly, the C–H stretching modes at *ca.*  $3000 \text{ cm}^{-1}$  suffer from much greater errors in excess of  $100 \text{ cm}^{-1}$ .

This is well understood to be caused by anharmonicity,<sup>132</sup> which also engenders numerous Fermi resonances, limiting the utility of this spectral region for structural characterization. See Ref.<sup>132</sup> for anharmonic phonon dispersion of polyethylene. For our purpose, the B3LYP/6-31G\*\* method is considered predictive for vibrational spectra also.

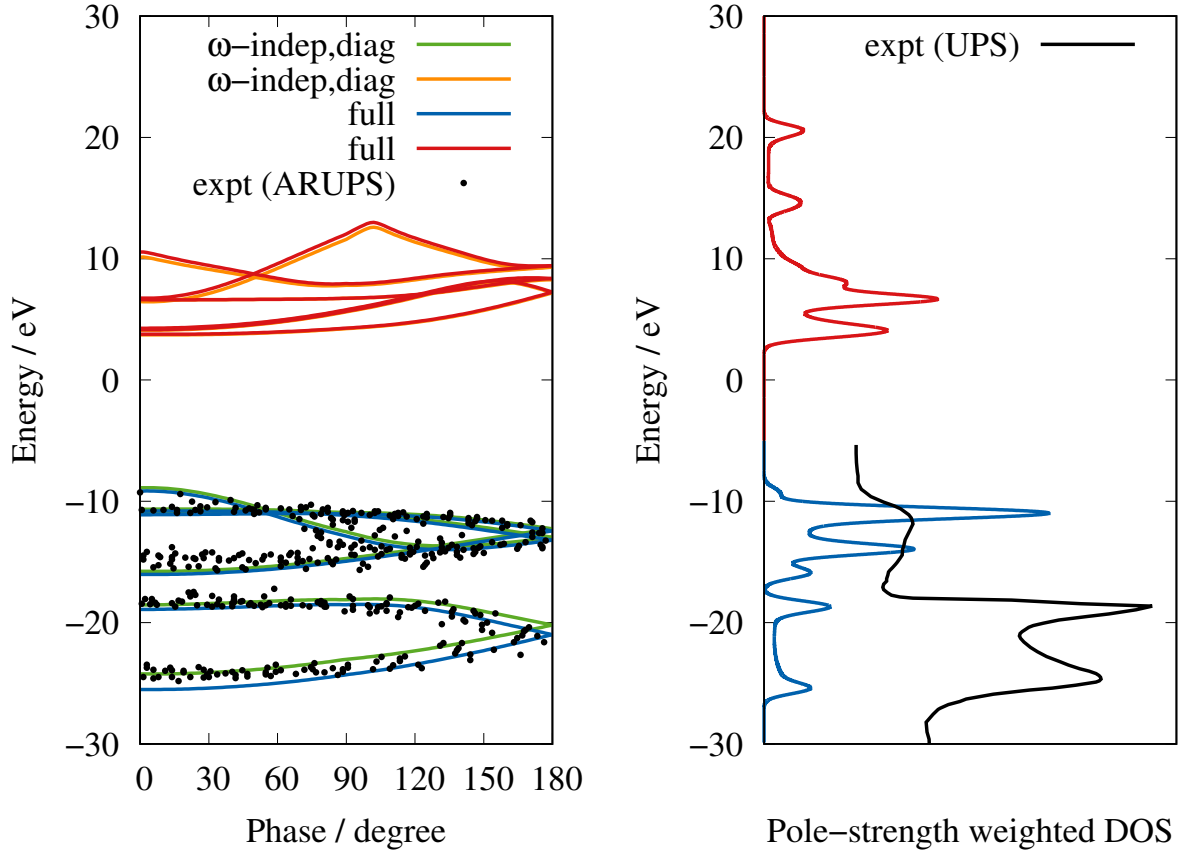


Figure 3: Electronic energy bands and DOS of  $(\text{C}_2\text{H}_4)_x$  computed by MBGF(2)/cc-pVDZ in the true-zone scheme (i.e., corresponding to a  $\text{C}_2\text{H}_4$  group as the repeat unit). The phase angle is equal to  $ka$  when  $k$  is the wave vector and  $a$  is the translational period. Here, ‘ $\omega$ -indep,diag’ stands for the diagonal, frequency-independent approximation to the self-energy [Eq. (22)], whereas ‘full’ for the use of the nondiagonal, frequency-dependent self-energy [Eq. (20)]. The DOS is weighted by the pole strength of Eq. (27) and convoluted with a Gaussian of a full-width-half-maximum (FWHM) of 1 eV. The ARUPS from Ueno *et al.*<sup>114</sup> The UPS from Pireaux *et al.*<sup>113</sup>

Figure 3 shows the calculated quasiparticle energy bands overlaid with the ones measured by angle-resolved ultraviolet photoelectron spectroscopy (ARUPS).<sup>114</sup> In the same figure, the electronic DOS is compared with the ultraviolet photoelectron spectrum (UPS).<sup>113</sup> The calculation was performed at the MBGF(2)/cc-pVDZ level with the diagonal and frequency-independent approxi-

mations (synonymous with the  $\Delta$ MP2 method<sup>99</sup>) or without any approximation to the self-energy (labeled “full” in Fig. 3). The impact of the diagonal and frequency-independent approximations is minimal and the two types of calculated energy bands agree accurately with each other. Without shifting vertically, the calculated valence bands agree with the ones obtained by ARUPS within the experimental error bars. The electronic DOS explains every major peak in the observed UPS quantitatively, although the peak intensities are not reproduced. The valence band edge at  $-9.2$  eV is much lower than the air oxidation potential of  $5.2$  eV,<sup>133</sup> and thus polyethylene is air stable. For valence bands, the MBGF(2)/cc-pVDZ method is predictive.

Experimentally, the fundamental band gap of polyethylene is  $8.0$  eV,<sup>134</sup> with the valence and conduction band edges located at  $-8.5$  and  $-0.5$  eV, respectively. The valence band edge will be lowered to  $-9.6$  eV for an isolated polyethylene chain in a vacuum, according to an extrapolation of the experimental data of oligomers (see p.169 of Ref. <sup>135</sup>). (The lowering by  $1.1$  eV is a dielectric effect of the bulk material.) The band gap of an isolated polyethylene chain in a vacuum is, therefore, estimated to be  $9.1$  eV (assuming the constancy of the conduction band edge at  $-0.5$  eV). The MBGF(2)/cc-pVDZ method (with “full” self-energy) predicts the band gap of  $13.1$  eV with the valence band edge at  $-9.1$  eV and conduction band edge at  $4.1$  eV. Given the good agreement of the calculated and observed valence bands, this large error is ascribed exclusively to the calculated conduction bands being too high. This, in turn, is likely due (primarily) to the inadequacy of the basis set (cc-pVDZ) in describing diffuse orbitals. In our theoretical model of a single chain in a vacuum, the converged (i.e., infinite-basis-set) conduction band edge should be at least as low as zero. If we assumed this, the calculated band gap would become  $9.1$  eV, which is more in line with the observed value of  $9.1$  eV. Nonetheless, MBGF(2)/cc-pVDZ cannot be considered predictive for fundamental band gaps or conduction bands.

Table 3 underscores the thermodynamic stability of polyethylene; its binding energy per  $\text{C}_2\text{H}_4$  group is  $23.6$  to  $29.6$  kcal/mol relative to its monomer, ethylene. Figure 4 plots the energy per  $\text{C}_2\text{H}_4$  group as a function of the lattice constant (translational period). It may be viewed as a reaction energy profile of simultaneous dissociation of polyethylene into an infinite number of

Table 3: Binding energy (in kcal/mol) of  $(\text{C}_2\text{H}_4)_x$ .

Method	Binding energy <sup>a</sup>
B3LYP/cc-pVDZ	23.6
MBPT(2)/cc-pVDZ	29.6

<sup>a</sup>The energy difference between the unit-cell energy of  $(\text{C}_2\text{H}_4)_x$  and the energy of  $\text{C}_2\text{H}_4$  in their respective B3LYP/cc-pVDZ-optimized geometries.

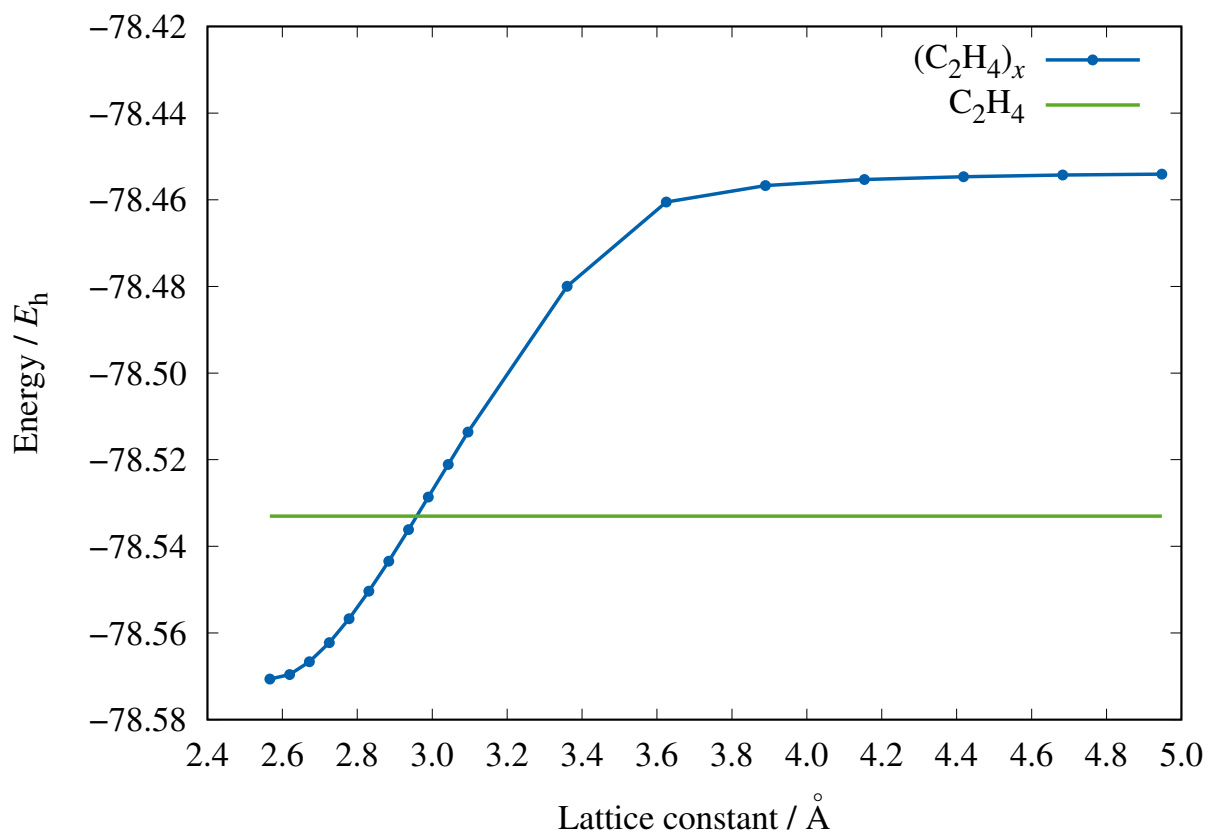


Figure 4: Unit-cell energy of  $(\text{C}_2\text{H}_4)_x$  as a function of the lattice constant computed by B3LYP/cc-pVDZ.



isolated ethylene molecules without geometrical relaxation in the latter. The energy of ethylene in its equilibrium geometry is indicated by a green line. While such a reaction pathway is unrealistic, the curve serves as a benchmark of highly stable polymers in comparison with other less stable ones discussed later. The figure shows that not only is the dissociation of polyethylene highly endothermic, it also faces a steep activation barrier partly because the unit-cell structure of  $(C_2H_4)_x$  differs significantly from the planar ethylene molecules.

### 3.2 Polyacetylene, $(C_2H_2)_x$

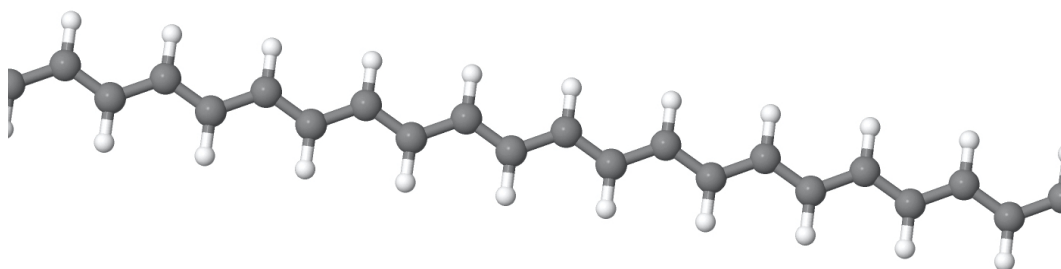


Figure 5: Polyacetylene,  $(C_2H_2)_x$ .

Polyacetylene<sup>136–140</sup> (Fig. 5) is a paradigm of organic conductive polymers,<sup>133</sup> and its geometrical, vibrational, and electronic structures are thoroughly studied. It is thermodynamically stable, although unsubstituted linear oligoenes are increasingly unstable with chain length.<sup>141,142</sup> It is also unstable to air because of its low ionization potential. There are four stereoregular isomers of polyacetylene:<sup>48</sup> *trans*-transoid (all-*trans*), *cis*-transoid, *trans*-cisoid, and *cis*-cisoid, with the former two being a linear planar structure, whereas the latter two being a helix.<sup>143</sup> Only the linear planar *trans*-transoid<sup>136,144–146</sup> and *cis*-transoid<sup>147–150</sup> isomers have been observed. The *cis*-transoid form thermally isomerizes to the more stable *trans*-transoid form. In this study, we focus on the *trans*-transoid isomer, which is most thoroughly characterized experimentally.<sup>136,137,151–155</sup>

There are many DFT and *ab initio* studies of polyacetylene.<sup>47,48,96,97,101,102,106–109,111,143,156–167</sup> Some of them revealed that nonhybrid DFT (i.e., not hybridized with the HF exchange) is incapable of reproducing Peierls' distortion, predicting too small a bond-length alternation and nearly

metallic electronic structure without doping.<sup>48,106,161,163,164,166</sup> HF theory, in contrast, exaggerates the bond-length alternation and fundamental band gap, whereas hybrid DFT and MBPT(2) tend to strike a good balance.<sup>48,97,106,111</sup>

Here, we applied B3LYP/cc-pVDZ and 6-31G\*\* for structures and phonon dispersion and DOS with  $S = 4$ ,  $L = 6$ , and  $K = 24$  using a  $C_2H_2$  group as the translational repeat unit. We also performed MBGF(2)/cc-pVDZ calculations with the frozen-core and mod-3 approximations.<sup>110,111</sup>

Table 4: Structural parameters of  $(C_2H_2)_x$  and  $C_2H_2$ .

Method	$(C_2H_2)_x$					$C_2H_2^a$	
	$r(C=C)^b$	$r(C-C)^b$	$r(CH)$	$a(CCC)$	$a(C=CH)$	$r(C\equiv C)$	$r(CH)$
B3LYP/6-31G**	1.368 Å	1.427 Å	1.091 Å	124.5°	118.5°	1.206 Å	1.066 Å
B3LYP/cc-pVDZ	1.371 Å	1.429 Å	1.097 Å	124.5°	118.4°	1.210 Å	1.073 Å
Observed <sup>c</sup>	1.36 Å	1.44 Å	...	...	...	1.203 Å	1.063 Å

<sup>a</sup>Acetylene. <sup>b</sup>Peierls' distortion. <sup>c</sup>The polyacetylene structure from Yannoni and Clarke.<sup>152</sup> The acetylene structure from Kuchitsu.<sup>168</sup>

The calculated equilibrium structures of all-*trans* polyacetylene and acetylene are compared with the observed<sup>152,168</sup> in Table 4. The B3LYP hybrid functional with either basis set correctly predicts the bond-length alternation, satisfying Peierls' theorem.<sup>48,106</sup> All measured bond lengths are reproduced by the calculation within 0.01 Å. The B3LYP/cc-pVDZ or 6-31G\*\* methods are, therefore, predictive for the structures of Peierls' systems, while nonhybrid DFT models are not.<sup>48,106,161,163,164,166</sup>

Table 5: Vibrational frequencies (in  $cm^{-1}$ ) of  $(C_2H_2)_x$ .

Irrep. <sup>a</sup> ; phase; activity	B3LYP/6-31G**	Observed <sup>b</sup>
$A_g$ ; $\theta = 0$ ; Raman	3138.8	2990
	1541.0	1457
	1328.1	1294
	1155.0	1066
$B_g$ ; $\theta = 0$ ; Raman	921.8	884
$A_u$ ; $\theta = 0$ ; IR	1060.9	1012
$B_u$ ; $\theta = 0$ ; IR	3151.9	3013
	1203.7	1170

<sup>a</sup>Isomorphic to the  $C_{2h}$  point group. <sup>b</sup>The IR data from Shirakawa and Ikeda<sup>136</sup> and from Takeuchi *et al.*<sup>153</sup> The Raman data from Kuzmany<sup>151</sup> and from Takeuchi *et al.*<sup>153</sup>

Figure 6 plots the calculated phonon dispersion curves and phonon DOS in comparison with the

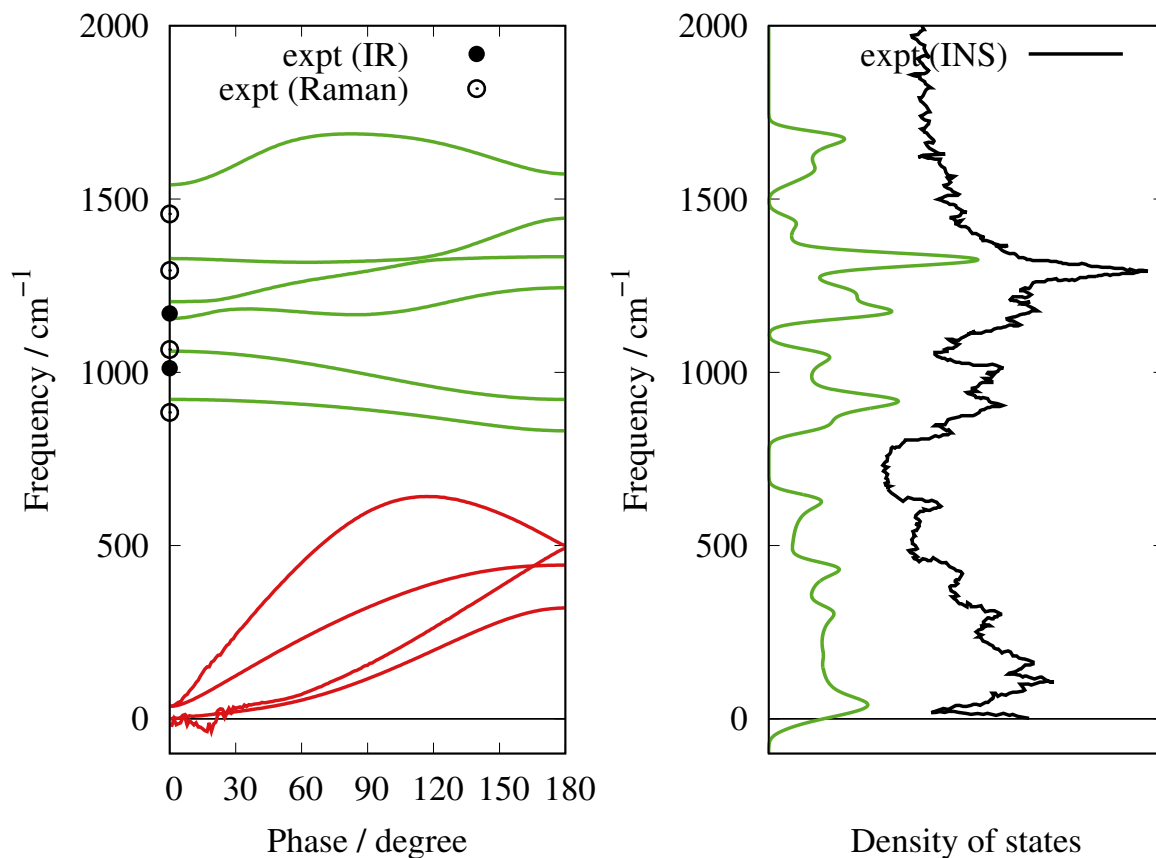


Figure 6: Phonon dispersion curves and DOS of  $(\text{C}_2\text{H}_2)_x$  computed by B3LYP/6-31G\*\*. The DOS is convoluted with a Gaussian of a FWHM of 40 cm<sup>-1</sup>. The IR data from Shirakawa and Ikeda<sup>136</sup> and from Takeuchi *et al.*<sup>153</sup> The Raman data from Kuzmany<sup>151</sup> and from Takeuchi *et al.*<sup>153</sup> The INS spectrum from Hirata *et al.*<sup>155</sup>

IR and Raman band positions<sup>136,151,153</sup> and INS spectrum.<sup>155</sup> Table 5 compiles the calculated and observed frequencies of the optically active phonons, which occur at the phase angle  $\theta = 0$ . While the calculated frequencies are systematically higher than the observed by a few percent, the level of agreement is good enough for reliable band assignments for all modes. They include the C=C and C-C stretching modes at 1457 and 1066  $\text{cm}^{-1}$ , respectively, whose correct description must be predicated on a proper account of Peierls' distortion. The overall shapes of the phonon dispersion curves are in excellent agreement with the ones calculated with an accurate force field determined by a hybrid experimental-computational approach.<sup>167</sup> All major peaks in the INS spectrum can also be unambiguously ascribed to the peaks in the phonon DOS. The B3LYP/6-31G\*\* method is, therefore, predictive for the vibrational spectra of Peierls' systems. The numerical noise in the acoustic-mode frequencies at  $\theta = 0$  is no more than 36  $\text{cm}^{-1}$ , when up to the fifth nearest neighbor  $\text{C}_2\text{H}_2$  groups are included in the normal-mode analysis.

Figure 7 draws the quasiparticle energy bands calculated by MBGF(2)/cc-pVDZ using two types of the self-energy. The impact of the frequency-independent and diagonal approximations to the self-energy is generally small, but it is greater for lower-lying valence bands and higher-lying conduction bands. This is understood by Eq. (32): In a higher-lying conduction band, the denominator of the first term can approach zero, where approximating  $\omega$  by  $\epsilon_i(k_i)$  can have a large effect. In a lower-lying valence band, the second term has the same propensity for a near-zero denominator. In more physical terms, the higher-lying (lower-lying) the conduction (valence) band, the greater the overlap between multi-electron and one-electron bands and the involvements of non-Koopmans' states, which cannot be described by the frequency-independent, diagonal approximation. The two major peaks in the calculated DOS occur at  $-10.6$  and  $-16.0$  eV. They correspond well with the observed peaks in the UPS at  $-10.0$  and  $-15.9$  eV. The MBGF(2)/cc-pVDZ method is predictive for valence bands with accuracy of a few tenths of an electronvolt.

The calculated valence band edge is located at  $-5.5$  eV. Its proximity to the air oxidation potential of 5.2 eV is consistent with the air instability of polyacetylene and its oligomers. The measured values of the fundamental band gap fall in the range of 1.4–1.8 eV,<sup>169</sup> as compared with the calcu-

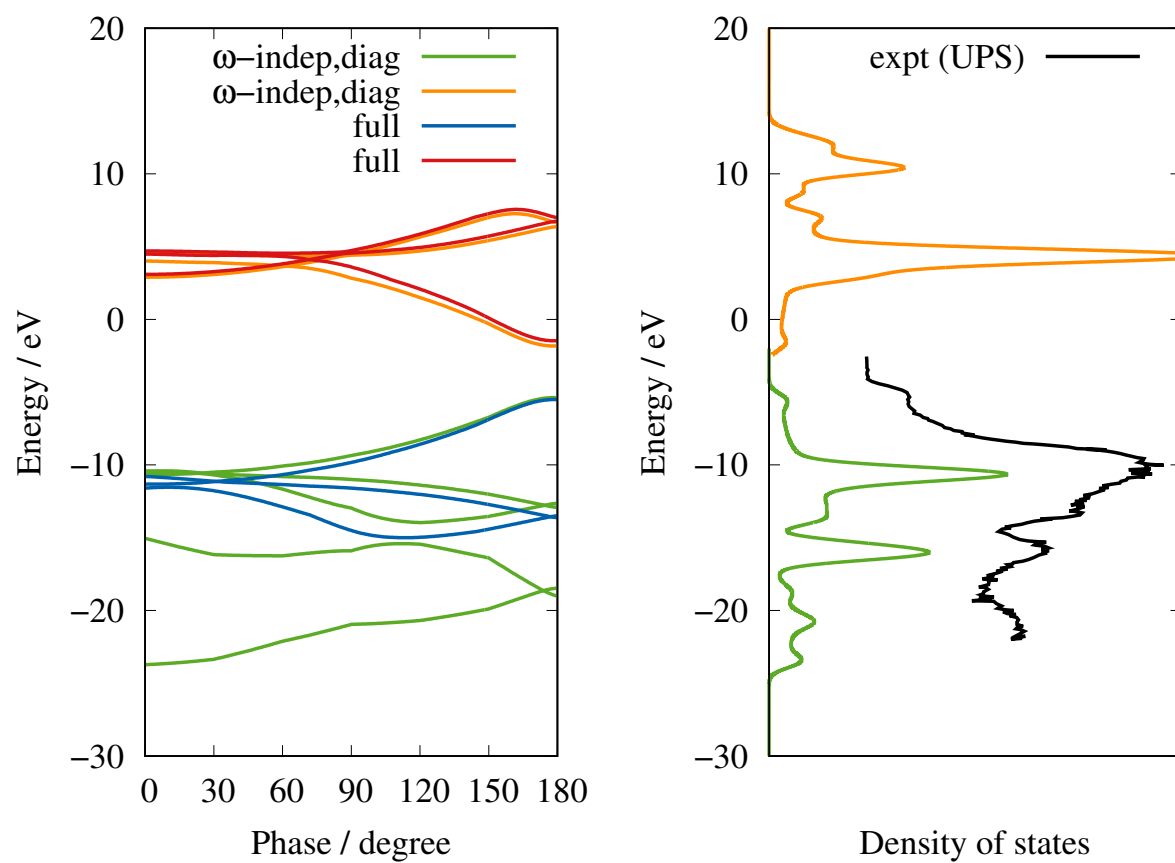


Figure 7: Electronic energy bands and DOS of  $(\text{C}_2\text{H}_2)_x$  computed by MBGF(2)/cc-pVDZ. The DOS is convoluted with a Gaussian of a FWHM of 1 eV. The UPS from Kamiya *et al.*<sup>154</sup>

lated value of 4.1 eV. The overestimation is again chiefly due to conduction bands being too high. In polyethylene (Sec. 3.1), the calculated conduction band edge is overestimated by *ca.* 4.6 eV. In polyacetylene, it is too high by *ca.* 2.2–2.6 eV only. In both cases, this is because of the inability of the compact basis set in describing diffuse conduction bands. The degree of overestimation is less in polyacetylene since its lower-lying conduction bands are made of conjugated  $\pi^*$  orbitals, which are relatively less diffuse. Nonetheless, the MBGF(2)/cc-pVDZ method is not predictive for band gaps or conduction bands.

The nonhybrid DFT models are well known<sup>48,106,161,163,164,166</sup> to predict zero or near-zero fundamental band gap for polyacetylene, violating Peierls’ theorem, owing to the incomplete cancellation of self-interaction. Hybridizing the exchange functional with a HF exchange alleviates this problem, sometimes yielding accurate band gaps for a variety of solids. However, the predicted band gaps sensitively depend on the weight of the admixed HF exchange and their agreement with the experimental values should be judged more or less arbitrary. We, therefore, relied on MBGF(2)/cc-pVDZ for energy bands, which is predictive for valence bands (but not for conduction bands or band gaps due to the inadequate basis set), while we used B3LYP for structures, vibrations, and thermodynamics only.

Table 6: Binding energy (in kcal/mol) of  $(\text{C}_2\text{H}_2)_x$ .

Method	Binding energy <sup>a</sup>
B3LYP/cc-pVDZ	49.5
MBPT(2)/cc-pVDZ	47.5

<sup>a</sup>The energy difference between the unit-cell energy of  $(\text{C}_2\text{H}_2)_x$  and the energy of  $\text{C}_2\text{H}_2$  in their respective B3LYP/cc-pVDZ-optimized geometries.

Table 6 indicates that polyacetylene is thermodynamically stable with the binding energy per  $\text{C}_2\text{H}_2$  unit cell of 47.5–49.6 kcal/mol relative to its monomer, acetylene. Figure 8 suggests that a complete dissociation of polyacetylene into acetylenes will likely face an activation barrier higher than the energy difference between the product and reactant because of a large change in the structure from the polymer unit cell to the monomer.

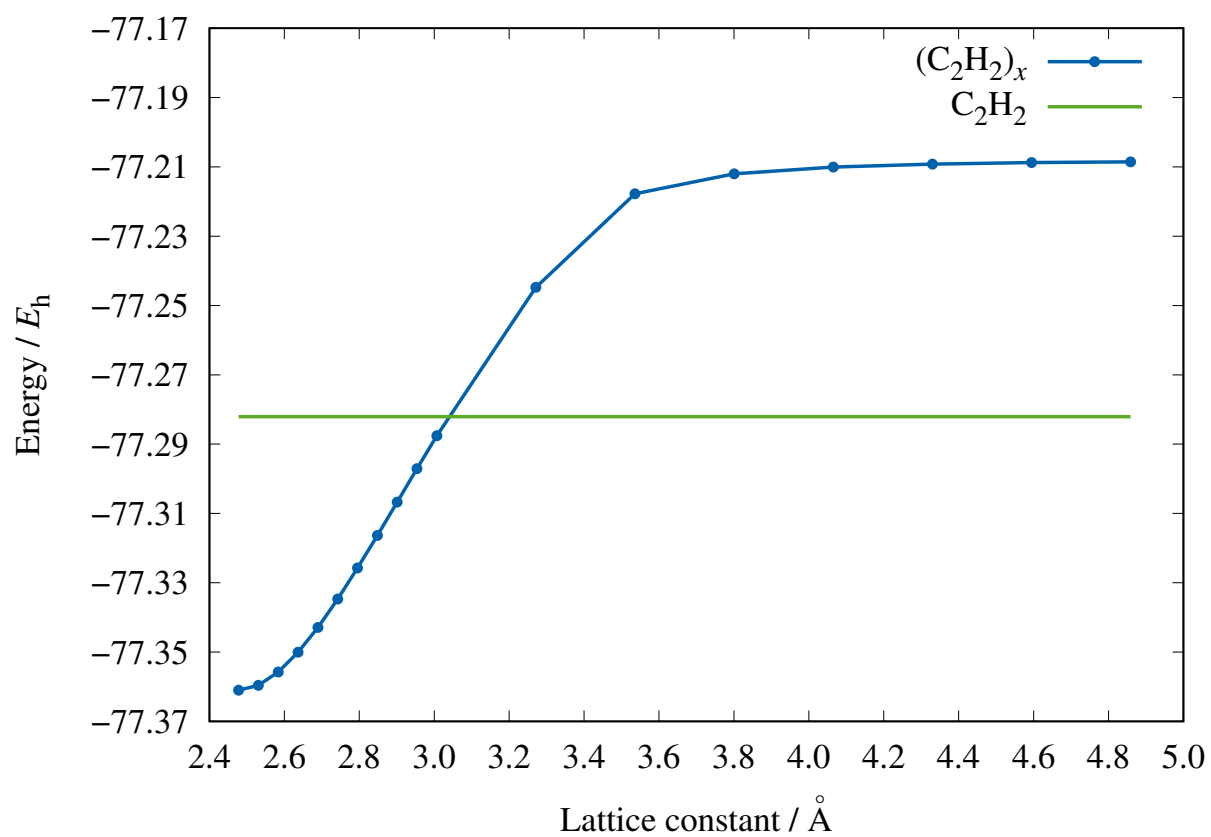


Figure 8: Unit-cell energy of  $(\text{C}_2\text{H}_2)_x$  as a function of the lattice constant computed by B3LYP/cc-pVDZ.

### 3.3 Polytetrafluoroethylene, $(\text{CF}_2)_x$

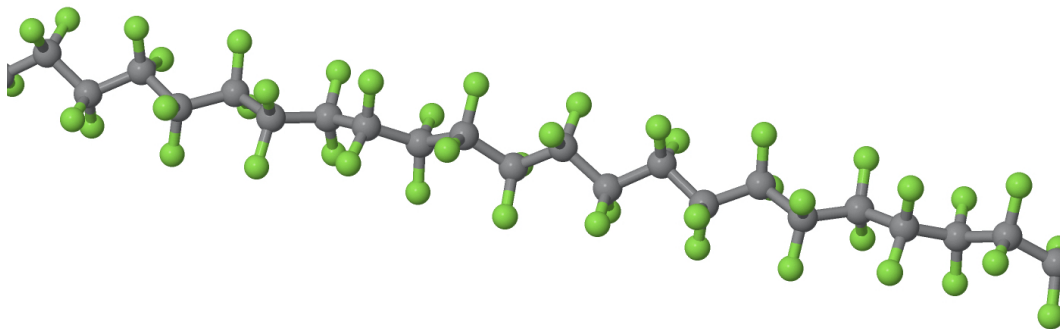


Figure 9: Polytetrafluoroethylene,  $(\text{CF}_2)_x$ .

Polytetrafluoroethylene (Fig. 9) adopts a 13/6 helical structure (phase II) at low temperature and pressure,<sup>54</sup> meaning that 13  $\text{CF}_2$  groups make six complete turns with the helical angle of  $\varphi = 6 \times 360^\circ / 13 = 166.2^\circ$ . At  $19^\circ\text{C}$ , it undergoes a phase transition to a slightly more relaxed 15/7 helix (phase IV) with helical angle of  $\varphi = 7 \times 360^\circ / 15 = 168.0^\circ$ .<sup>55</sup> Crystal structures of various phases were interrogated experimentally<sup>54,57,170,171</sup> and computationally.<sup>56,172–174</sup> Bunn and Howells,<sup>54</sup> who first determined the helical conformation of this polymer, argued that its cylindrical profile permits axial rotation and translation of chains relative to one another far below melting points, contributing to its super low friction. The primary source of the low friction is, however, its low polarizability and thus weak dispersion forces of the system containing “hard” fluorine atoms. It is thermodynamically and chemically stable.<sup>175</sup>

Table 7: Structural parameters of  $(\text{CF}_2)_x$  and  $\text{C}_2\text{F}_4$ .

Method	$(\text{CF}_2)_x$						$\text{C}_2\text{F}_4^a$		
	$r(\text{CC})$	$r(\text{CF})$	$a(\text{CCC})$	$a(\text{FCF})$	$d(\text{CCCC})$	$\varphi^b$	$r(\text{CC})$	$r(\text{CF})$	$a(\text{FCF})$
B3LYP/6-31G**	1.562 Å	1.353 Å	113.3°	109.4°	163.0°	165.8°	1.326 Å	1.325 Å	113.7°
B3LYP/cc-pVDZ	1.567 Å	1.353 Å	113.0°	109.1°	161.7°	164.7°	1.329 Å	1.324 Å	113.3°
Observed (13/6) <sup>c</sup>	(1.53 Å)	(1.33 Å)	116° <sup>d</sup>	(108°)		166.2° <sup>d</sup>	1.311 Å	1.319 Å	112.4°

<sup>a</sup>Tetrafluoroethylene. <sup>b</sup>The helical angle [Eqs. (1)–(3)]. <sup>c</sup>The polytetrafluoroethylene structure (in parentheses) consistent with the X-ray diffraction data of Weeks *et al.*<sup>57</sup> The tetrafluoroethylene structure from Hellwege and Hellwege.<sup>176</sup> <sup>d</sup>Bunn and Howells.<sup>54</sup>

X-ray photoelectron spectroscopic, UPS, and electron energy loss spectroscopic studies were reported.<sup>135,156,177–183</sup> Miyamae *et al.*<sup>181</sup> obtained the valence band structures by ARUPS, but the observed topmost valence band was in poor agreement with the HF/STO-3G calculation of Seki



*et al.*,<sup>180</sup> which assumed a planar zigzag conformation. Yoshimura *et al.*<sup>184</sup> reevaluated the ARUPS data to bring it into more accurate agreement with a simulation. See also Refs.<sup>135,156,158,178–180,183,185–190</sup> for other band-structure calculations.

Generally, three types of Brillouin zone are considered for a helix:<sup>128</sup> In the true-zone scheme, the translational repeat unit ( $C_{13}F_{26}$  in the case of 13/6-helical polytetrafluoroethylene) is taken as the real-space unit cell. In the extended-zone scheme, the rototranslational (physical) repeat unit ( $CF_2$ ) is the real-space unit cell.<sup>89</sup> In the semi-extended-zone scheme, two rototranslational repeat units ( $C_2F_4$ ) forms the real-space unit cell. The last scheme is introduced here because of the structural similarity of polytetrafluoroethylene ( $\varphi \approx 166^\circ$ ) with polyethylene ( $\varphi = 180^\circ$ ), whose true-zone scheme is based on a  $C_2H_4$  group.

The selection rules of the IR and Raman transitions in an infinite helical polymer were deduced by Higgs.<sup>191</sup> Phonons in a helix are optically active if the phase angle ( $\theta$ ) between adjacent unit-cell oscillators in the extended-zone scheme is equal to zero,  $\varphi$ , or  $2\varphi$ , where  $\varphi$  is the helical angle. More detailed IR and Raman activities can be decided on the basis of isomorphism with a point group. For example, the line group of the 13/6 chain of polytetrafluoroethylene is isomorphic to the  $D_{13}$  point group. Its phonons with vibrational phase angle of  $\theta = 0$  transform as  $A_1$  or  $A_2$ , which are Raman or IR active, respectively. The phonons at  $\theta = \varphi$  transform as  $E_1$ , which are both IR and Raman active, whereas those at  $\theta = 2\varphi$  transform as  $E_2$ , which are Raman active.

The IR spectra of polytetrafluoroethylene was measured by Liang and Krimm.<sup>192</sup> Koenig and Boerio<sup>193</sup> and Peacock *et al.*<sup>194</sup> reported the Raman spectra. Coherent INS spectra were observed by Twisleton and White,<sup>195</sup> following a measurement by LaGarde *et al.*<sup>196</sup> Hannon *et al.*<sup>197</sup> performed a normal-mode analysis with empirical force fields, using three helix models: 13/6, 15/7, and planar zigzag. The most complete vibrational analysis was carried out by Piseri *et al.*,<sup>128</sup> who also reported coherent INS spectra and established IR and Raman band assignments.

In this study, we ran the B3LYP/cc-pVDZ and 6-31G\*\* calculations for structures, phonon dispersions, and phonon DOS and the MBGF(2)/cc-pVDZ calculations in the frozen-core and mod-6 approximations<sup>110,111</sup> for quasiparticle energy bands and electronic DOS with  $S = 8$ ,  $L = 12$ ,

and  $K = 48$ . A rototranslational (physical) repeat unit used was a  $\text{CF}_2$  group. Up to the eighth nearest neighbor  $\text{CF}_2$  groups were considered in the phonon dispersion calculation.

Table 7 compares the optimized geometries of polytetrafluoroethylene and its monomer, tetrafluoroethylene, with the observed.<sup>54,57,176</sup> The B3LYP method with either basis set reproduces bond lengths and bond angles within a few hundredths of one Ångstrom and a few degrees, respectively, of the experimental values, and is deemed predictive for structures. The helical angle ( $\varphi$ ) is calculated to be  $164.7\text{--}165.8^\circ$ , which are closer to  $166.2^\circ$  of the 13/6 helix (low-temperature conformation) than to  $168.0^\circ$  of the 15/7 helix (high-temperature conformation). The calculated  $\varphi$ , however, does not precisely correspond to any commensurable structure.

In the 13/6-helical conformation, the fluorine atoms are not farthest apart from one another.<sup>54</sup> It was argued that the steric repulsion between the fluorine atoms is compensated for by having a larger CCC angle of  $116^\circ$  than the corresponding angle of  $112^\circ$  in polyethylene since it is energetically harder to stretch the C–C bond.<sup>54</sup> This argument is not supported by our calculations: The CCC angles are roughly the same ( $113^\circ$ ) between polyethylene and polytetrafluoroethylene, but the C–C bond is noticeably longer in the latter. Rather, the helical angle of  $166^\circ$  may be chosen by nature to stagger (at least slightly) the fluorine atoms not only with the first but also with the second nearest neighbor  $\text{CF}_2$  groups (see Fig. 1 of Ref.<sup>128</sup>).

Comparison of the calculated and observed frequencies of the IR and Raman bands<sup>192,193</sup> is made in Table 8. Without any alteration to the assignment *F-II* of Piseri *et al.*,<sup>128</sup> the calculated frequencies agree excellently with the observed with the mean absolute deviation of  $17\text{ cm}^{-1}$ . Figure 10 plots the phonon dispersion curves and phonon DOS alongside the IR and Raman band positions and INS spectrum.<sup>195</sup> Note that the INS spectrum is due to coherent scattering with a specific scattering angle of  $36^\circ$  and does not necessarily reflect the phonon DOS if the dispersions are large. Nonetheless, the calculated DOS is consistent with the INS spectrum, both displaying broad peaks in the same frequency domains. The B3LYP/6-31G\*\* method is predictive for vibrations.

In a helical polymer, three zero-frequency acoustic modes are expected: two at  $\theta = 0$  (longi-

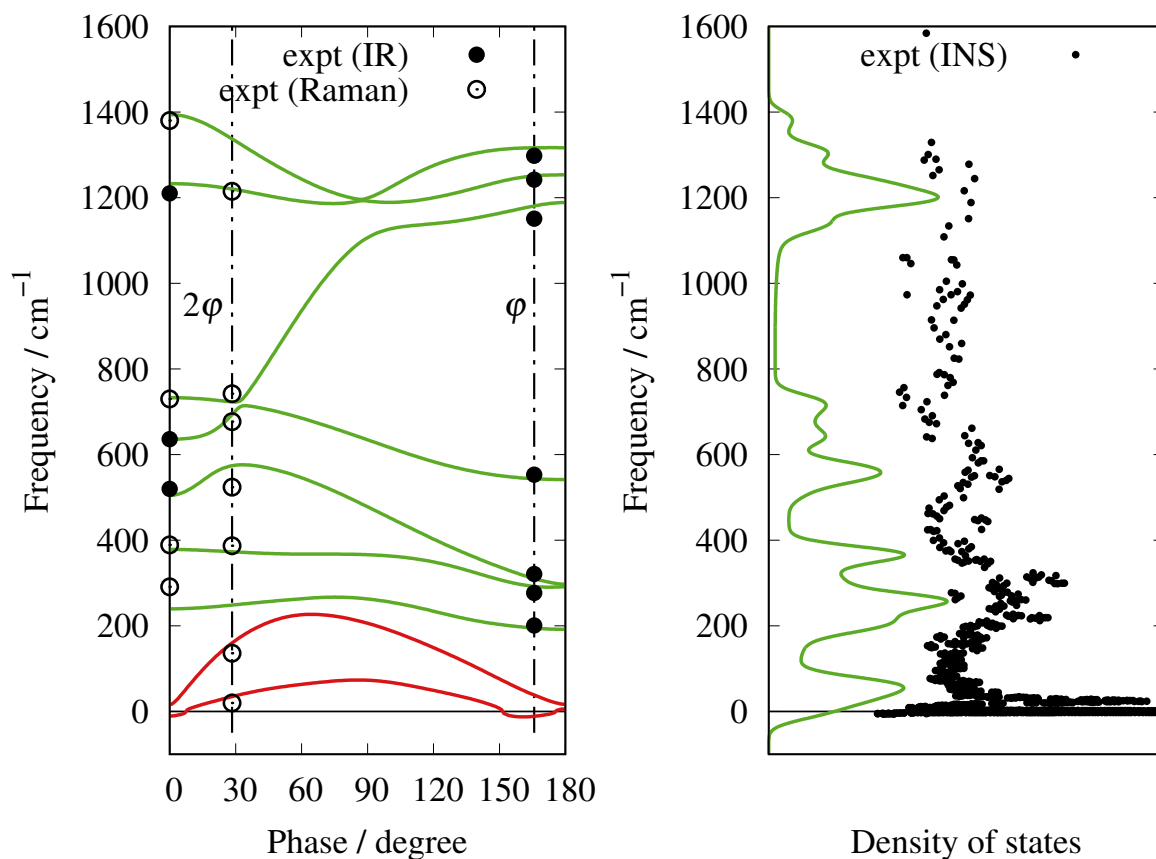


Figure 10: Phonon dispersion curves and DOS of  $(\text{CF}_2)_x$  computed by B3LYP/6-31G\*\* in the extended-zone scheme (i.e., corresponding to a  $\text{CF}_2$  group as the repeat unit). Phonons are optically active when the phase angle of adjacent  $\text{CF}_2$  oscillators is zero,  $\varphi$  (helical angle), or  $2\varphi$ , which are indicated by dotted-dashed lines. The DOS is convoluted with a Gaussian of a FWHM of  $40 \text{ cm}^{-1}$ . The coherent INS spectrum (the scattering angle of  $36^\circ$ ) from Twisleton and White.<sup>195</sup>

Table 8: Vibrational frequencies (in  $\text{cm}^{-1}$ ) of  $(\text{CF}_2)_x$ .

Irrep. <sup>a</sup> ; phase; activity	B3LYP/6-31G**	Observed <sup>b</sup>
$A_1$ ; $\theta = 0$ ; Raman	1394.2	1380
	733.0	730
	378.5	389
	239.8	291
$A_2$ ; $\theta = 0$ ; IR	1232.8	1210
	635.8	636
	504.7	520
$E_1$ ; $\theta = \varphi$ ; IR, Raman	1316.6	1298
	1251.0	1242
	1180.7	1151
	543.5	553
	310.5	321
	292.1	277
	194.8	201
	38.3	...
$E_2$ ; $\theta = 2\varphi$ ; Raman	1337.4	...
	1220.3	1215
	723.1	742
	693.2	677
	573.9	524
	373.0	387
	248.6	...
	160.0	136
	34.7	20

<sup>a</sup>Isomorphic to the  $D_{13}$  point group.  $\varphi$  is the helical angle. <sup>b</sup>Based on the assignment  $F$ -II of Piseri *et al.*<sup>128</sup> The IR data ( $A_2$ ,  $E_1$ ) from Liang and Krimm.<sup>192</sup> The Raman data ( $A_1$ ,  $E_2$ ) from Koenig and Boerio.<sup>193</sup>

tudinal and spinning) and one at  $\theta = \varphi$  (transverse). Their frequencies are calculated to be  $11i$ ,  $16$ , and  $11i \text{ cm}^{-1}$ , respectively. The imaginary frequencies of these sizes are numerical errors caused by the distance-based truncation of the force-constant matrices and do not imply a saddle point on the potential energy surface. They are relatively small for polytetrafluoroethylene likely because of the absence of hydrogens, whose small masses may amplify numerical errors in the reciprocal-mass-weighted force constants.

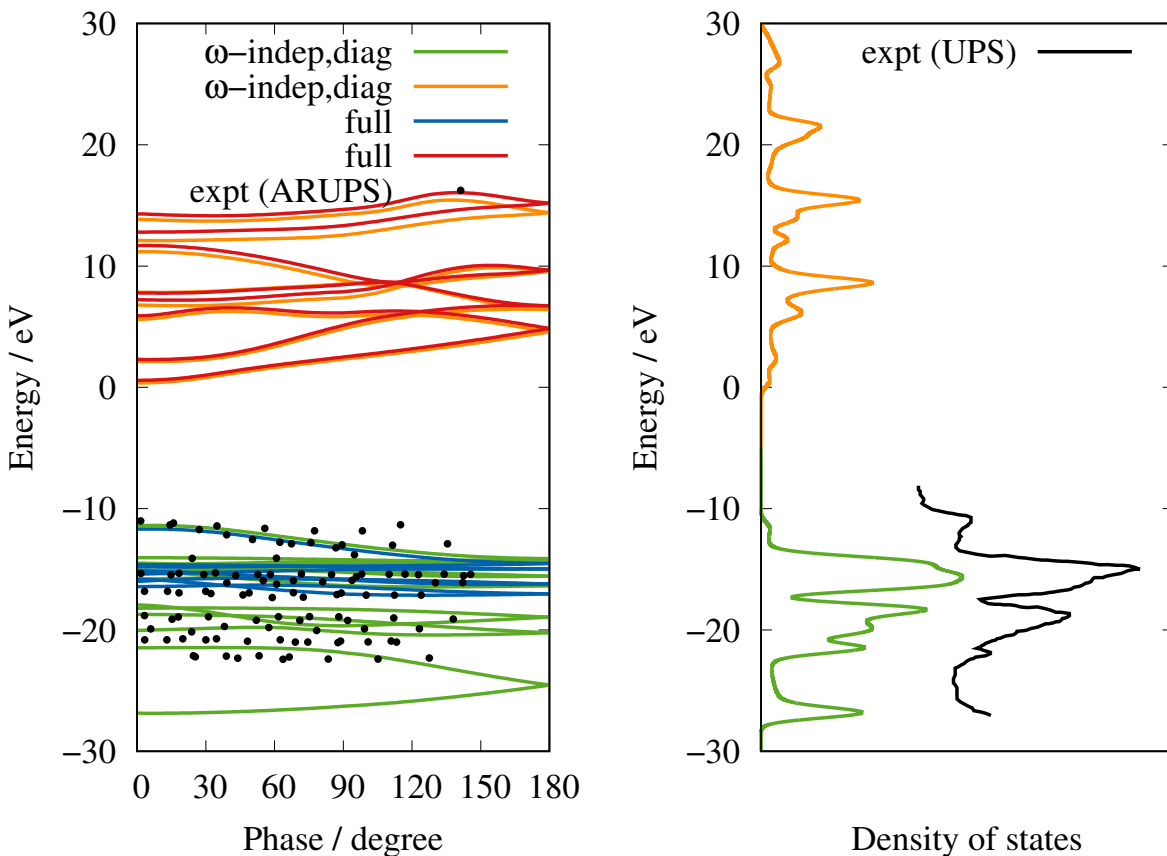


Figure 11: Electronic energy bands and DOS of  $(\text{C}_2\text{F}_4)_x$  computed by MBGF(2)/cc-pVDZ in the semi-extended-zone scheme (i.e., corresponding to a  $\text{C}_2\text{F}_4$  group as the repeat unit). The DOS is convoluted with a Gaussian of a FWHM of 1 eV. The ARUPS and UPS were measured originally by Miyamae *et al.*<sup>181</sup> and then recalibrated by Yoshimura *et al.*<sup>184</sup>

Figure 11 compares the MBGF(2)/cc-pVDZ quasiparticle energy bands and DOS with the experimental data obtained by ARUPS and UPS.<sup>181,184</sup> They are in accurate agreement with each other, regardless of the approximations used in the self-energy. The two highest peaks in the UPS are observed at  $-15.0$  and  $-18.8 \text{ eV}$ , which are in good accord with the calculated peaks in the

convoluted DOS at  $-15.6$  and  $-18.3$  eV, respectively. Therefore, the MBGF(2)/cc-pVDZ method is predictive for valence bands with accuracy of *ca.* 0.5 eV. The reinterpretation of the experimental data by Yoshimura *et al.*<sup>184</sup> is supported by our calculations.

The fundamental band gap of an isolated polytetrafluoroethylene chain in a vacuum is estimated to be 11.9 eV with the valence band edge at  $-11.7$  eV and conduction band edge at 0.2 eV.<sup>135</sup> These values were deduced from an extrapolation of the UPS and vacuum UV absorption spectra of oligomers, and differ from the ones in the bulk material (e.g., the valence band edge of the bulk is located at  $-10.6 \pm 0.1$  eV).<sup>135</sup> The large band gap is consistent with the good insulation and low friction of polytetrafluoroethylene, and the deep valence band edge explains its chemical and air stability. In our MBGF(2)/cc-pVDZ calculation using the “full” self-energy, the valence and conduction band edges are located at  $-11.7$  and 0.6 eV, respectively, with the predicted band gap of 12.3 eV, which is in reasonable agreement with the observed (11.9 eV). As in polyethylene, the valence band edge is accurately reproduced (within 0.1 eV of the observed in this case). The conduction band edge of polytetrafluoroethylene is overestimated by only 0.4 eV in contrast to an overestimation by 4.7 eV in polyethylene. This is understandable because the electron-attached states of fluorine-rich molecules should be describable reasonably well by the cc-pVDZ basis set. Nevertheless, the predictive accuracy of the MBGF(2)/cc-pVDZ method for conduction bands and band gaps cannot be claimed generally.

Table 9: Binding energy (in kcal/mol) of  $(\text{C}_2\text{F}_4)_x$ .

Method	Binding energy <sup>a</sup>
B3LYP/cc-pVDZ	32.7
MBPT(2)/cc-pVDZ	41.9

<sup>a</sup>The energy difference between the unit-cell energy of  $(\text{C}_2\text{F}_4)_x$  and the energy of  $\text{C}_2\text{F}_4$  in their respective B3LYP/cc-pVDZ-optimized geometries.

Table 9 attests to the thermodynamic stability of polytetrafluoroethylene against dissociation into its monomers. An unrelaxed dissociation reaction energy profile illustrated in Fig. 12 also suggests the existence of a barrier to dissociation that is higher than the energy difference between product and reactant, adding to its kinetic stability. This, in turn, may be partly due to the large

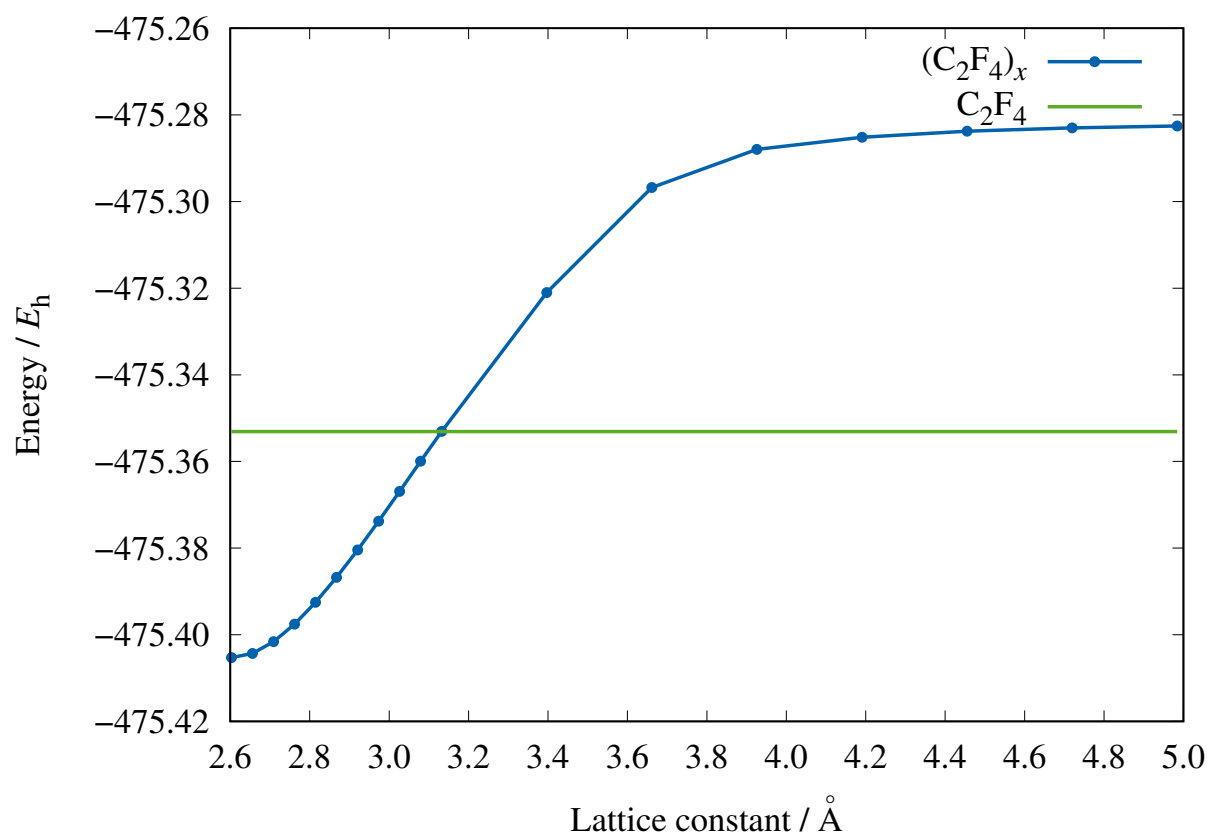


Figure 12: Unit-cell energy of  $(C_2F_4)_x$  as a function of the lattice constant computed by B3LYP/cc-pVDZ.

structural change from the  $sp^3$ -bonded  $C_2F_4$  in the polymer to  $sp^2$ -bonded planar tetrafluoroethylene.

### 3.4 Polyazene, $(N_2)_x$

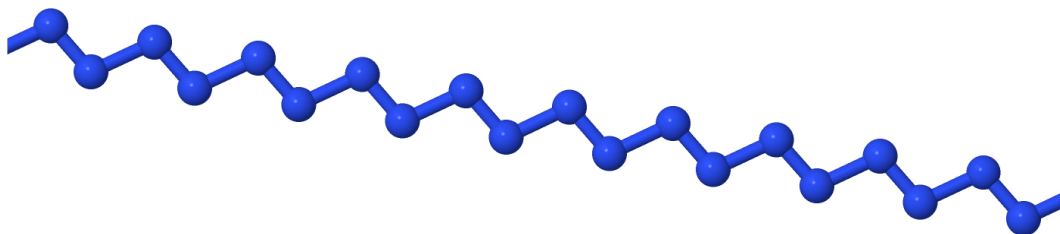


Figure 13: Polyazene,  $(N_2)_x$ .

As an infinitely catenated chain of nitrogen, we consider all-*trans* polyazene (Fig. 13). Since it is isoelectronic with all-*trans* polyacetylene (Sec. 3.2), we sought its possible metastable structure in a planar zigzag conformation with alternating N–N and N=N bonds. We also examined other conformations with no avail (see below). The B3LYP/cc-pVDZ and 6-31G\*\* calculations were performed for the structures, phonon dispersions, and phonon DOS with  $S = 4$ ,  $L = 6$ , and  $K = 24$  using a  $N_2$  group as the translational repeat unit. The MBGF(2)/cc-pVDZ calculations for the quasiparticle energy bands and electronic DOS additionally used the frozen-core and mod-3 approximations.<sup>110,111</sup> Quantitative accuracy of these methods has been established for the organic polymers in Secs. 3.1–3.3.

There are two approaches to realizing longer catenated chains of nitrogen under ambient conditions. One is the chemistry (bottom-up) approach, which enlarges the ring or elongates the chain with careful design of its protective terminal groups.<sup>3–6</sup> The other is the physics (top-down) approach, which aims at high-pressure polymerization of solid or liquid  $N_2$ , followed by lifting of the pressure to kinetically trap the metastable polymers.<sup>4,21,198–200</sup> In this context, “polymer” refers to a nonmolecular solid including two- or three-dimensional covalently-bonded networks. In both approaches, synthetic and computational studies played essential and complementary roles.

In the chemistry approach, successful syntheses<sup>201–212</sup> of nitrogen allotropes were piloted by



computations such as those on  $N_4$ ,<sup>213–215</sup>  $N_5$ ,<sup>215,216</sup>  $N_6$ ,<sup>213,214,216–223</sup>  $N_8$ ,<sup>213,214,224,225</sup>  $N_{10}$ ,<sup>226</sup>  $N_{12}$ ,<sup>227</sup> and even  $N_{20}$ ,<sup>228</sup> often using such highly accurate methods as CCSD(T) (coupled-cluster singles and doubles with noniterative triples).<sup>229,230</sup> Christie *et al.*<sup>201</sup> reported the synthesis and detection of a bent open-chain structure of  $N_5^+$ . See also Vij *et al.*<sup>202</sup> Cacace *et al.*<sup>203</sup> synthesized an open-chain  $N_4$ . These were followed by the synthesis and isolation of the pentazole anion or cyclo- $N_5^-$  by Vij *et al.*,<sup>204</sup> by Barazov *et al.*,<sup>209</sup> and by Zhang *et al.*<sup>210</sup> Subsequently, Bi *et al.*<sup>205</sup> synthesized  $N_6H_2$ , consisting of cyclo- $N_5$  appended with another nitrogen atom. Zhang *et al.*<sup>211</sup> constructed stable zeolitic clusters composed of  $Na^+$  and cyclo- $N_5^-$ , containing as many as 60 nitrogen atoms.

Among these, the most salient may be hexazine, all nitrogen analog<sup>231</sup> of benzene; hexazine is to polyazene as benzene is to polyacetylene. Previous computational studies<sup>213,217,219–221</sup> (with the exception of Ref.<sup>218</sup>) indicated that its planar  $D_{6h}$  structure is a saddle point on its potential energy surface and is, therefore, unstable either towards dissociation into  $N_2$  (without an activation barrier<sup>232</sup>) or towards structural relaxations. Lauderdale *et al.*<sup>213</sup> showed that it has an out-of-plane bending vibration with an imaginary frequency and thus spontaneously transforms to either a twist or boat structure and eventually to hexaazaprismane (which is bound by N–N single bonds). The most stable isomer, however, seems to be a (twisted) open chain,<sup>219–221,227,233</sup> which may be further stabilized in condensed phase.<sup>223</sup> These findings suggest that polyazene (either in the planar *trans-transoid*, *cis-transoid*, or *trans-cisoid* conformation) may not be sufficiently stabilized by aromaticity to withstand an out-of-plane structural distortion or even dissociation. It was also pointed out that B3LYP and CCSD(T) give largely consistent structural predictions for  $N_6$ .<sup>221</sup>

Li *et al.*<sup>206</sup> reported the synthesis of a molecule containing a catena-8 nitrogen chain in the all-*trans* polyazene conformation. Its termini are protected by five-membered rings, in much the same way all-*trans* polyenes need to be stabilized by terminal phenyl rings.<sup>234</sup> They furthermore observed reversible *trans-cis* photoisomerization, although the same isomerization in polyacetylene primarily occurs thermally or by doping.<sup>235</sup> Tang *et al.*<sup>207,208</sup> extended the all-*trans* polyazene motif to catena-10 and 11 nitrogen chains. Unlike hexazine, that these can be synthesized and isolated may be taken as supportive evidence for the potential existence of infinite

all-*trans* polyazene.  $C_2N_{14}$  (1-diazidocarbamoyl-5-azidotetrazole) is one of the most sensitive explosives ever made.<sup>236–238</sup> Its central motif is a catenated  $N_5$  chain in a *cis*-polyazene-like conformation, also supporting the metastable existence of *cis*-transoid or *trans*-cisoid polyazene (see below for potential high-pressure polymerization of *cis*-polyazene). Open-chain  $N_7$  detected by Huang *et al.*,<sup>212</sup> in contrast, is wire-like and looks more like polyynes.

Turning to the physics approach, Nellis *et al.*<sup>239</sup> is the first to computationally explore the possibility of infinitely catenated nitrogen under high pressure, predicting a polymeric liquid nitrogen. McMahan and LeSar<sup>20</sup> proposed the *cubic gauche* (cg) form of solid nitrogen under 1 Mbar, the pressure achievable by diamond anvil cells, spurring both experimental and computational searches. Mailhoit *et al.*<sup>21</sup> refined the computational characterization of the cg form and also discovered other polymeric forms including a two-dimensional black phosphorous structure (stable above 210 GPa) and one-dimensional bond-alternating chain. The latter was predicted to be metastable, likely transforming to a tri-coordinated solid. A one-dimensional chain was also studied with crystal-orbital theory by Pohl *et al.*,<sup>240</sup> using DFT in the local density approximation (LDA). The method displayed a severe underestimation of the bond-length alternation, also predicting a metallic electronic structure. This is well established to be due to the self-interaction error in LDA, causing the identical problem for isoelectronic *trans*-polyacetylene<sup>48,106,161,163,164,166</sup> (see Sec. 3.2). These results clearly indicate that DFT without a hybrid of the HF exchange is fundamentally incapable of describing Peierls' systems, which are bond-alternating insulators at 0 K. Subsequent DFT studies by Alemany and Martin<sup>241</sup> and by Mattson *et al.*<sup>242</sup> seem to suffer from the same qualitative error of LDA, predicting a metallic zigzag chain.

The first experimental report of infinitely catenated nitrogen under high pressure (150 GPa) came from Goncharov *et al.*,<sup>243</sup> who observed the disappearance of the  $N\equiv N$  stretching vibration of  $2300\text{--}2500\text{ cm}^{-1}$  and concomitant emergence of lattice vibrations in the range of  $200\text{--}600\text{ cm}^{-1}$ . This phase is found to be a semiconductor and believed to be amorphous. Erements *et al.*<sup>244</sup> were able to release pressure and bring this phase to a metastable state under ambient conditions. Gregoryanz *et al.*<sup>245,246</sup> determined the phase diagrams of the relevant phases spectroscopically. The first

crystalline phase of catenated nitrogen was achieved by Eremet *et al.*<sup>22,23,198</sup> in the cg form at high temperature and pressure. Whereas this phase could not be quenched at ambient conditions, this synthetic achievement spurred further computational predictions of new polymeric phases.<sup>199,200</sup> Tomasino *et al.*<sup>247</sup> synthesized a two-dimensional layered-polymeric form of nitrogen at 120–180 GPa, well above the stability range of the cg form. See Sontising and Beran<sup>248,249</sup> for more recent, high-accuracy computational studies of solid nitrogen phases.

The past decade has seen a combination of the chemistry and physics approaches: high-pressure polymerization of shorter catenated nitrogen rings or chains. Li *et al.*<sup>250</sup> computationally predicted high-pressure condensation of  $\text{KN}_3$  into benzene-like rings or polymer chains. Prasad *et al.*<sup>251</sup> performed an evolutionary crystal structure exploration of  $\text{LiN}_3$  under high pressure up to 300 GPa, and found the formation of benzene-like  $\text{N}_6$  rings and *cis*-polyacetylene-like infinite one-dimensional chains, which are furthermore predicted to be metastable under ambient conditions. They are both metallic as they are negatively charged (the authors used a hybrid DFT functional to guard against the aforementioned problem<sup>48,106,161,163,164,166</sup>). This is perhaps the most supportive study yet of the existence of polyazene, albeit in the *cis* conformation. Shen *et al.*<sup>252</sup> reported a similar study, exploring a larger pool of high-pressure structures of  $\text{LiN}_x$  including *cis*-polyacetylene-like chains. In their DFT-based crystal-structure search, Peng *et al.*<sup>253</sup> discovered that, under high pressure,  $\text{CsN}_2$  transforms to infinite helical chains of nitrogen. Since the chain is doped with Cs, it is said to adopt a similar conformation as helical polyoxane<sup>254</sup> (see Sec. 3.7), although it contradicts the observed effect of chemical doping on the structure of polyacetylene.<sup>136–140</sup> Steele and Oleynik,<sup>255</sup> on the other hand, found the chain structure of nitrogen in the high-pressure phase of  $\text{KN}_x$  to be unstable. Williams *et al.*<sup>256</sup> studied complexes of rubidium and catenated nitrogen under high pressures, again causing the nitrogen atoms to form *cis*-polyazene chains. These ideas have been recently realized synthetically by Bykov *et al.*<sup>257–259</sup> Some of the high-pressure structures indeed feature *cis*-polyazene chains chelating metals, which are metastable under ambient conditions.

Table 10 lists the calculated structural parameters of a planar zigzag chain of all-*trans* polyazene.

Table 10: Structural parameters of  $(\text{N}_2)_x$  and  $\text{N}_2$ .

Method	$(\text{N}_2)_x$			$\text{N}_2$
	$r(\text{N}=\text{N})^a$	$r(\text{N}-\text{N})^a$	$a(\text{NNN})$	$r(\text{N}\equiv\text{N})$
B3LYP/6-31G**	1.249 Å	1.432 Å	106.1°	1.106 Å
B3LYP/cc-pVDZ	1.248 Å	1.434 Å	106.0°	1.105 Å
Observed <sup>b</sup>	(1.205 Å)	(1.429 Å)	(109.2°)	1.098 Å

<sup>a</sup>Peierls' distortion. <sup>b</sup>The *trans*-tetrazene-(2) structure (in parentheses) from Veith and Schlemmer.<sup>260</sup> The  $\text{N}_2$  structure from Huber and Herzberg.<sup>261</sup>

It is predicted to display a bond-length alternation of 0.18–0.19 Å, obeying Peierls' theorem. The same B3LYP method reproduces the observed  $\text{N}_2$  bond length within 0.01 Å. The calculated  $\text{N}=\text{N}$  and  $\text{N}-\text{N}$  bond lengths of polyazene are much longer and slightly longer, respectively, than the corresponding bond lengths of *trans*-tetrazene-(2),  $\text{H}_2\text{N}-\text{N}=\text{N}-\text{NH}_2$ , which is not conjugated (see also Sec. 3.5). That the  $\text{N}-\text{N}$  bond in polyazene is not shorter, but instead longer than the non-conjugated  $\text{N}-\text{N}$  bond in tetrazene underscores the severity of the lone-pair-lone-pair repulsion, destabilizing polyazene.

Table 11: Vibrational frequencies (in  $\text{cm}^{-1}$ ) of  $(\text{N}_2)_x$ .

Irrep. <sup>a</sup> ; phase; activity	B3LYP/6-31G**
$A_g$ ; $\theta = 0$ ; Raman	948.3
	1570.2

<sup>a</sup>Isomorphic to the  $C_{2h}$  point group.

Figure 14 plots the phonon dispersion curves and phonon DOS, which consist of two optical (green) and four acoustic (red) branches. Table 11 gives the frequencies of the optical phonons at the zone center ( $\theta = 0$ ), which are predicted to be Raman active. The high-pressure (150-GPa) synthesis<sup>243</sup> of a catenated form of nitrogen was accompanied by the disappearance of IR and Raman bands at 2300–2500  $\text{cm}^{-1}$  and the concomitant emergence of bands in the range of 200–600  $\text{cm}^{-1}$ . While the disappearance of the  $\text{N}\equiv\text{N}$  stretching bands at 2300–2500  $\text{cm}^{-1}$  clearly indicates an extended chain formation and is not inconsistent with all-*trans* polyazene, both the number and frequencies of the lattice vibrations contradict such an interpretation, even after considering the immense pressure difference between theory and experiment.

However, more alarming is the fact that the lowest acoustic branch has an imaginary frequency

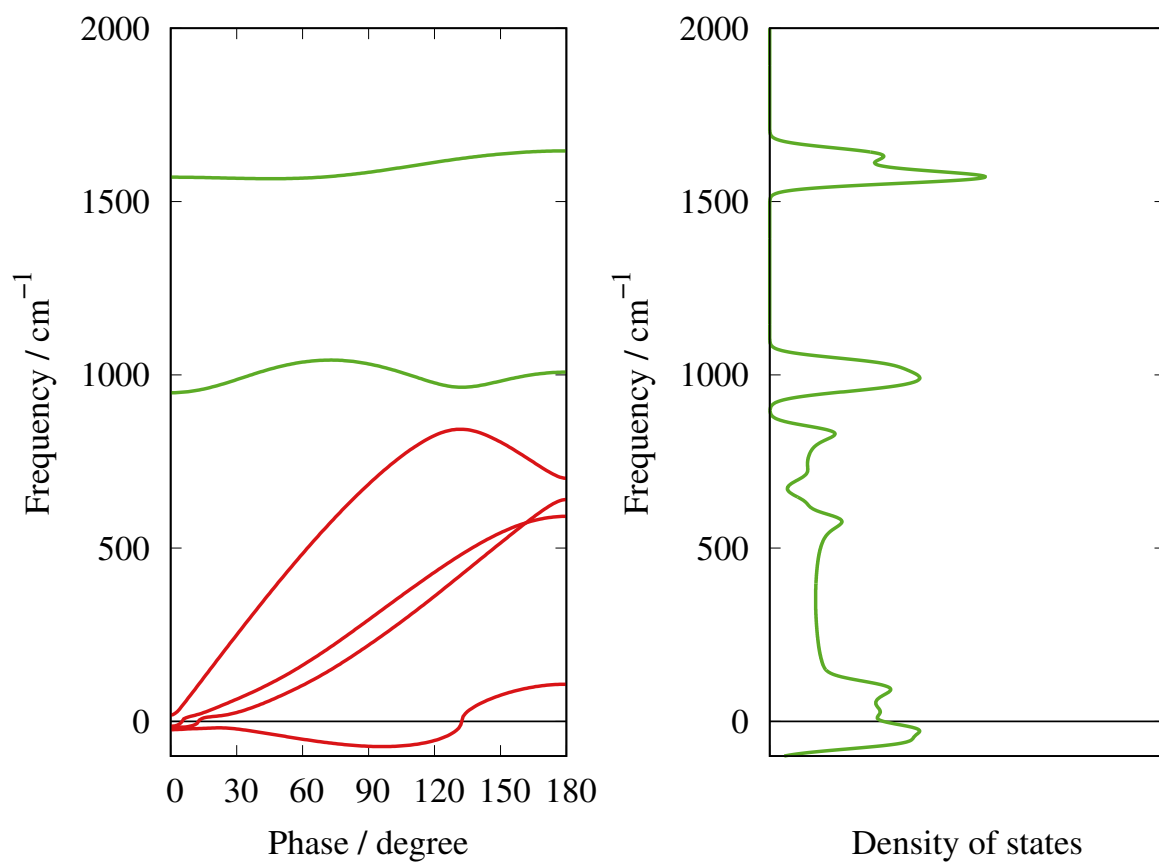


Figure 14: Phonon dispersion curves and DOS of  $(\text{N}_2)_x$  computed by B3LYP/6-31G\*\*. The DOS is convoluted with a Gaussian of a FWHM of  $40 \text{ cm}^{-1}$ .

(reaching  $73i\text{ cm}^{-1}$  at  $\theta = 96^\circ$ ) in a wide range of the phase angle  $\theta$ . This cannot be ascribed to an inevitable numerical error caused by the lack of strict translational and rotational invariance as it occurs at phase angles far from  $\theta = 0$  (the calculation included force-constant matrices up to the fifth nearest neighbor  $\text{N}_2$  units). It indicates that the planar zigzag structure is a saddle point on the potential energy surface, which is reminiscent of the planar hexagonal structure of hexazine being also a saddle point.<sup>213,217,219–221</sup>

Hence, we sought other stable structures including the planar *cis*-transoid, planar *trans*-cisoid, helical *trans*-transoid, corrugated *trans*-transoid, Ni-chelated *cis*-transoid, and Ni-chelated *trans*-cisoid structures. All of them tended to rearrange into separate  $\text{N}_2$  fragments during the course of geometry optimization. This by no means rules out the existence of local minima for these structures, but it strongly suggests that they are too unstable to exist as metastable species under ambient conditions.

Table 12: Binding energy (in kcal/mol) of  $(\text{N}_2)_x$ .

Method	Binding energy <sup>a</sup>
B3LYP/cc-pVDZ	−58.4
MBPT(2)/cc-pVDZ	−70.3

<sup>a</sup>The energy difference between the unit-cell energy of  $(\text{N}_2)_x$  and the energy of  $\text{N}_2$  in their respective B3LYP/cc-pVDZ-optimized geometries.

The large negative binding energies in Table 12 indicate that all-*trans* polyazene is unstable towards dissociation into  $\text{N}_2$ . The unrelaxed dissociation reaction energy profile in Fig. 15 exhibits a low activation barrier of *ca.* 12.5 kcal/mol for the exothermic reaction. The barrier may not exist once the  $\text{N}_2$  structure is relaxed along the reaction coordinate, but even if the barrier persists, it may be low enough for the polymer to dissociate thermally. The low barrier may, in turn, be partly due to the similarity of the unit-cell and monomer structures. The energy profile is completely different from those of the stable organic polymers (Figs. 4, 8, and 12).

We, therefore, conclude that all-*trans* polyazene is unlikely to exist under ambient conditions or even at low temperatures.

For completeness, we document in Fig. 16 the quasiparticle energy bands and electronic DOS

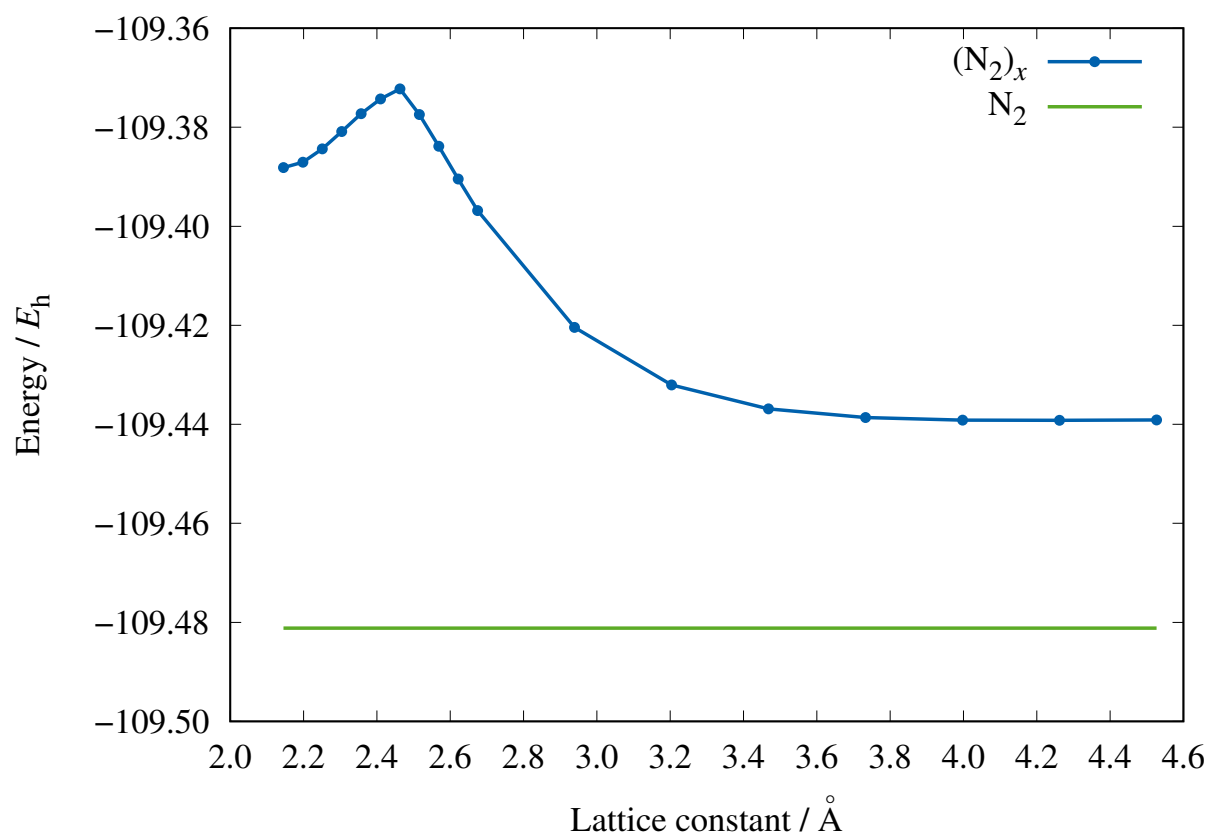


Figure 15: Unit-cell energy of  $(\text{N}_2)_x$  as a function of the lattice constant computed by B3LYP/cc-pVDZ.

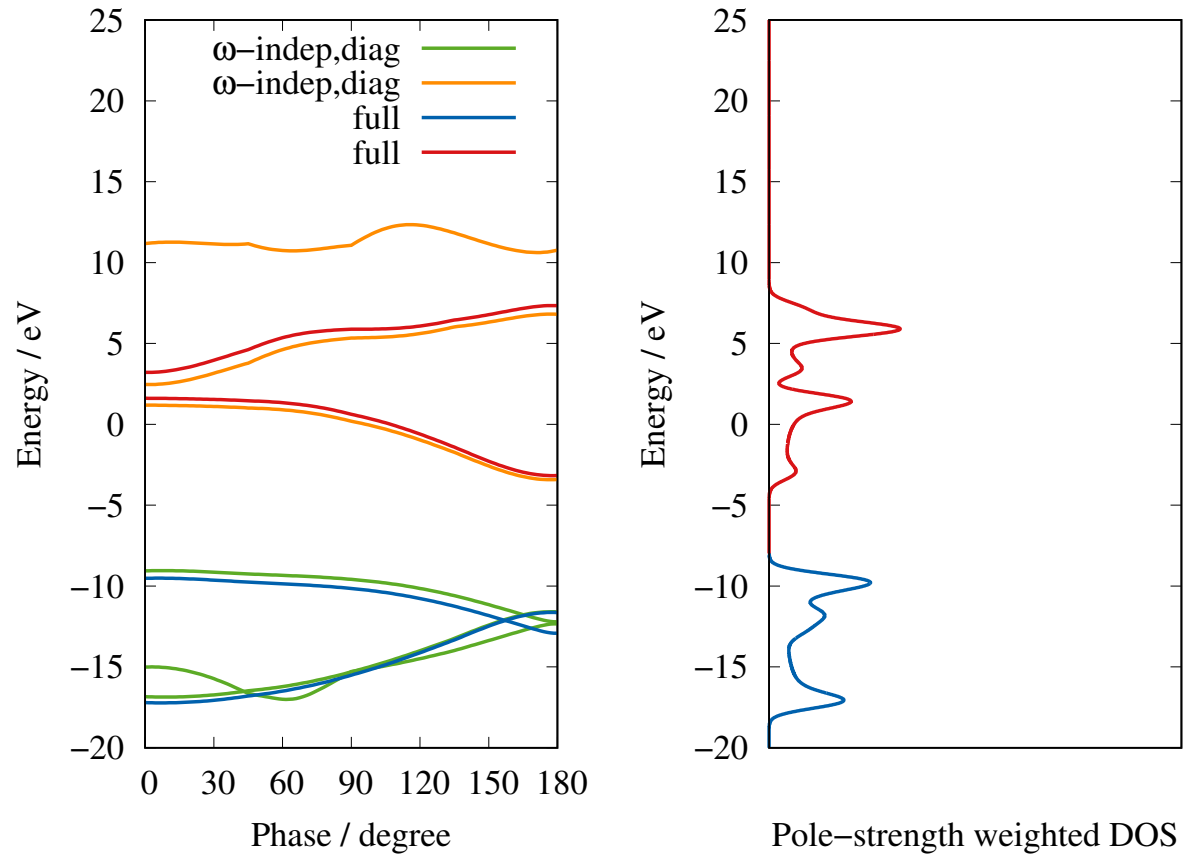


Figure 16: Electronic energy bands and DOS of  $(N_2)_x$  computed by MBGF(2)/cc-pVDZ. The DOS is weighted by the pole strength of Eq. (27) and convoluted with a Gaussian of a FWHM of 1 eV.



calculated by the MBGF(2)/cc-pVDZ method. The energy bands of polyazene differ strikingly from those of isoelectronic polyacetylene. In polyazene, the valence band is roughly parallel with the conduction band, and has the opposite dispersion from the valence band of polyacetylene. This is due to the fact that the valence band of polyazene consists of in-plane  $\sigma$  orbitals accommodating lone pairs, whereas the valence and conduction bands of polyacetylene are  $\pi$  and  $\pi^*$  orbitals, respectively. The predicted UPS from polyazene has a peak at the ionization onset owing to the nearly flat valence band at its top. The HF energy bands (not shown) are qualitatively the same as the MBGF(2) energy bands (which is a prerequisite for smooth energy-band interpolation in the mod- $n$  approximation<sup>110,111</sup>). Quantitatively, HF valence (conduction) bands are lower (higher) by a few electronvolts than the MBGF(2) counterparts, and the correlation effect has a greater impact on the  $\pi$  and  $\pi^*$  bands than on the  $\sigma$  band.

### 3.5 Isotactic polyazane, $(\text{NH})_x$

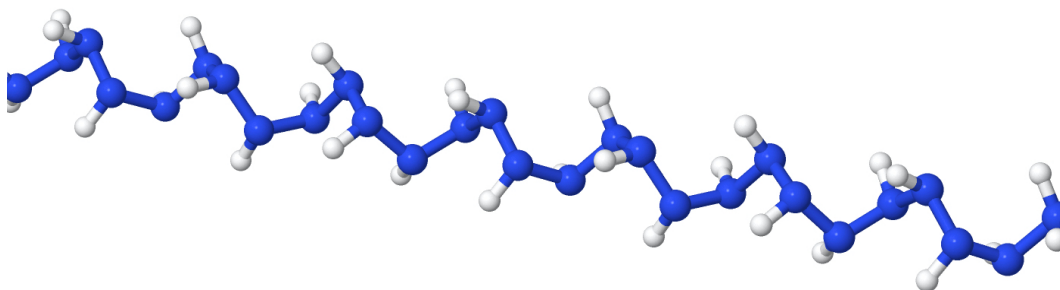


Figure 17: Isotactic polyazane,  $(\text{NH})_x$ .

While polyazene (Sec. 3.4) may be deemed too unstable to exist under ambient conditions, stability of a catenated nitrogen chain can be enhanced generally by introducing heteroatoms in its structure.<sup>3</sup> For instance, hexazine (see also Sec. 3.4) becomes stable in the planar hexagonal structure when one or more oxygen atoms are attached to nitrogens by dative bonds.<sup>222</sup> The repulsions between the lone pairs of adjacent nitrogen atoms, which are responsible for the instability, are alleviated by the lone pairs being consumed by these dative bonds.

In this subsection, we explore the stabilization of catenated nitrogen bonds by hydrogen-

tion. We thus consider isotactic polyazane  $(\text{NH})_x$  (Fig. 17), which is helical and isoelectronic with polyethylene (Sec. 3.1). Intrachain hydrogen bonds might further stabilize it,<sup>24</sup> although this has been disputed.<sup>25</sup> We performed B3LYP/cc-pVDZ and 6-31G\*\* geometry optimization with  $S = 12$ ,  $L = 24$ , and  $K = 48$  using a NH group as the rototranslational (physical) repeat unit. This was followed by phonon dispersion and phonon DOS calculations in the ninth nearest neighbor approximation. We then carried out the MBGF(2)/cc-pVDZ calculations for the quasiparticle energy bands and electronic DOS in the frozen-core and mod-6 approximations.<sup>110,111</sup>

There are five stable isomers of  $\text{N}_3\text{H}_3$ .<sup>262</sup> The most stable *trans*-triazene is already too unstable towards rapid acid-catalyzed decomposition to be isolated (see Förstel *et al.*<sup>263</sup> for time-of-flight mass-spectrometry detection of its isomers), despite the utility of synthetic reagents containing the triazene moiety.<sup>11</sup> Cyclo- $\text{N}_3\text{H}_3$  or triaziridine is isoelectronic with cyclopropane; cyclo- $\text{N}_3\text{H}_3$  is to polyazane as cyclopropane is to polyethylene. It is predicted<sup>262</sup> to be the least stable isomer, yet has been isolated for structural determination by Kim *et al.*<sup>264</sup> and by Heo *et al.*,<sup>265</sup> hinting at an unknown factor stabilizing it. Kim *et al.*<sup>264</sup> and Heo *et al.*<sup>265</sup> also isolated triazane  $\text{N}_3\text{H}_5$  in its complexes with  $\text{Ag}^+$ , whereas Förstel *et al.*<sup>266</sup> detected it in the gas phase. See Richard and Ball,<sup>267</sup> and Dana *et al.*<sup>268</sup> for computation studies of triazane.

Tetrazene,<sup>5</sup>  $\text{H}_2\text{N}-\text{N}=\text{N}-\text{NH}_2$ , first isolated by Wiberg *et al.*<sup>269</sup> in 1975, was shown<sup>260</sup> to adopt a planar *trans* conformation. It is unstable and prone to thermolysis into  $\text{NH}_4$  and  $\text{N}_3$  or into  $\text{N}_2$  and hydrazine ( $\text{N}_2\text{H}_4$ ) above  $0^\circ\text{C}$ , which may be taken as a more discouraging finding for polyazene (Sec. 3.4) than for polyazane. Hydrazine itself is also thermodynamically unstable, but it is kinetically stable, and because of that, it is an excellent rocket fuel with the second highest thrust per mass per time (the highest is liquid hydrogen).<sup>268</sup> Cyclo- $(\text{NH})_4$  (tetrazetidine) and  $\text{N}_4\text{H}_6$  (tetrazane) are structurally more salient to polyazane and have been studied computationally.<sup>270-272</sup> Ritter *et al.*<sup>270</sup> concluded that despite its instability towards diazene dissociation, “the tetrazetidine seems to be trapped kinetically by rather high energy barriers.” Larger  $(\text{NH})_x$  rings and longer  $\text{H}(\text{NH})_x\text{H}$  chains were studied by Zhao and Gimarc,<sup>25</sup> focusing on their strain energies. Experimentally, triazane  $\text{N}_3\text{H}_5$  and terazane  $\text{N}_4\text{H}_6$  were detected in a microwave discharge of hydrazine.<sup>273</sup> A molecule

containing the triazane moiety was also formed in an environment of astrophysical relevance.<sup>274</sup>

These are supportive of the metastable existence of polyazane.

Table 13: Structural parameters of  $(\text{NH})_x$  and  $\text{N}_2\text{H}_2$ .

Method	$(\text{NH})_x$						$\varphi^b$	<i>trans</i> - $\text{N}_2\text{H}_2^a$		
	$r(\text{NN})$	$r(\text{NH})$	$a(\text{NNN})$	$a(\text{HNN})$	$d(\text{NNNN})$	$d(\text{HNNH})$		$r(\text{NN})$	$r(\text{NH})$	$a(\text{HNN})$
B3LYP/6-31G**	1.431 Å	1.025 Å	109.9°	105.9°	73.7°	75.5°	98.1°	1.246 Å	1.040 Å	106.1°
B3LYP/cc-pVDZ	1.429 Å	1.029 Å	110.0°	105.8°	73.7°	75.5°	98.1°	1.245 Å	1.045 Å	105.8°
Observed <sup>a</sup>							(98.2°) <sup>c</sup>	1.252 Å	1.028 Å	106.9°

<sup>a</sup>The *trans*-diazene structure from Carloti *et al.*<sup>275</sup> <sup>b</sup>The helical angle [Eqs. (1)–(3)]. <sup>c</sup>The helical angle for a 11/3 helix (not observed) is given in parentheses.

Table 13 compiles the predicted structural parameters of isotactic polyazane. Given the good agreement between the calculated and observed structures of its monomer (*trans*-diazene), we expect them to be within a few hundredths of one Ångstrom and a few degrees of the exact values. The optimized helical angle is 98.1°. A commensurable helix that has a similar helical angle is 11/3 ( $\varphi = 98.2^\circ$ ). The N–N bond length in cyclo- $\text{N}_3\text{H}_3$  was measured to be 1.49 Å.<sup>264</sup> That this is slightly longer than the predicted N–N bond length (1.43 Å) in polyazane is reasonable given the presence of ring strain in cyclo- $\text{N}_3\text{H}_3$ . The observed N–N bond length (1.46 Å) of hydrazine<sup>276</sup> is closer to the calculated N–N bond length of polyazane.

The NNNN dihedral angle in polyazane is predicted to be 73.7°, which is less than half of the CCCC dihedral angle of 180° in isoelectronic polyethylene. It is smaller still than the corresponding angle of 166° in polytetrafluoroethylene, which suffers from the fluorine-fluorine repulsion. Zhao and Gimarc<sup>25</sup> also observed the dihedral angle of about 90° subtended by adjacent lone pairs in the  $(\text{NH})_x$  rings or long  $\text{H}(\text{NH})_x\text{H}$  chains. They invoked the *gauche* effect<sup>14–16</sup> to rationalize the conformation qualitatively. The predicted structure furthermore suggests that there is no extra stabilization due to intrachain hydrogen bonds between adjacent NH bonds because they are not oriented appropriately.

Figure 18 plots the phonon dispersion curves and phonon DOS. They consist of four optical (green) and two acoustic (red) branches. The N–H stretching optical modes above 3000  $\text{cm}^{-1}$  are not shown in this figure. Since this is a helix, two acoustic (longitudinal and spinning) modes have zero frequencies at  $\theta = 0$  and one acoustic (transverse) mode also has null energy at  $\theta = \varphi$ .

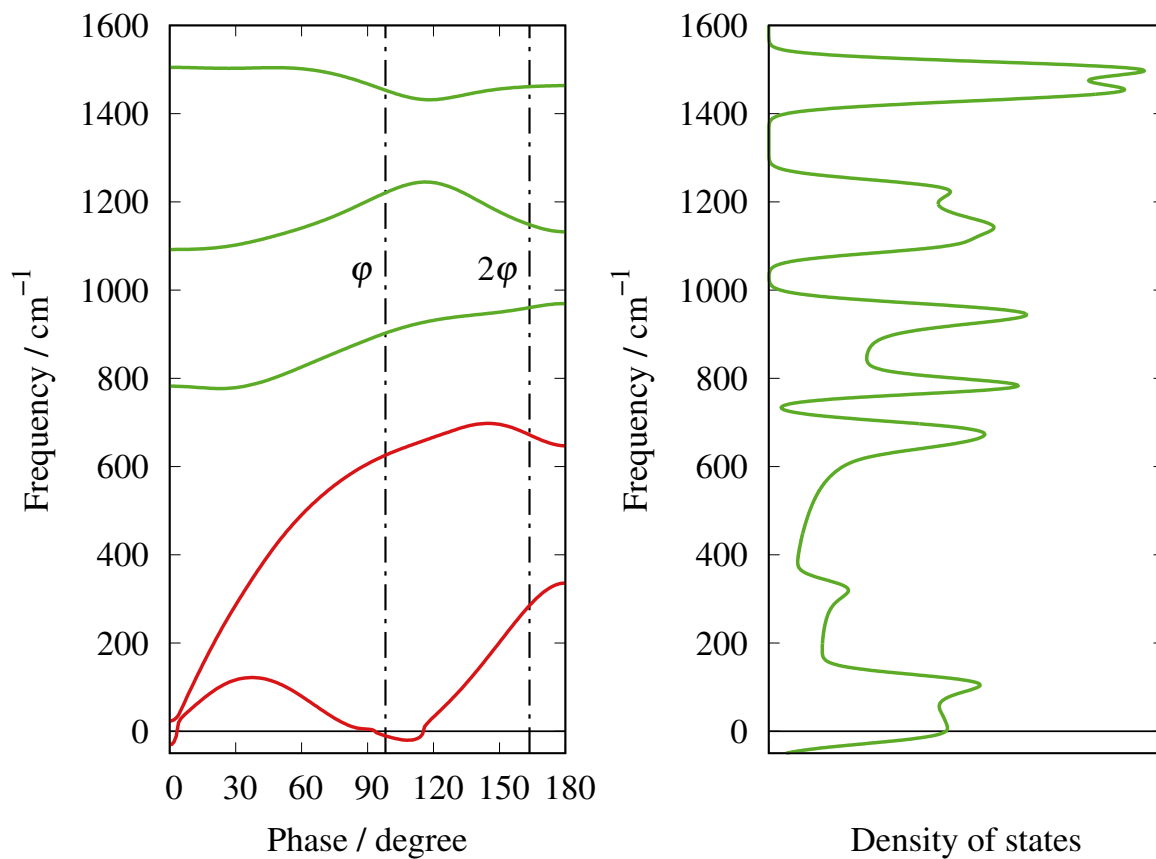


Figure 18: Phonon dispersion curves and DOS of  $(\text{NH})_x$  computed by B3LYP/6-31G\*\*. The DOS is convoluted with a Gaussian of a FWHM of  $40 \text{ cm}^{-1}$ .

Table 14: Vibrational frequencies (in  $\text{cm}^{-1}$ ) of  $(\text{NH})_x$ .

Irrep. <sup>a</sup> ; phase; activity	B3LYP/6-31G**
$A$ ; $\theta = 0$ ; IR, Raman	3425.7
	1504.9
	1092.1
	782.2
$E_1$ ; $\theta = \varphi$ ; IR, Raman	3419.2
	1453.1
	1220.7
	902.4
	625.7
$E_2$ ; $\theta = 2\varphi$ ; Raman	3420.7
	1461.2
	1148.3
	960.3
	671.8
	285.1

<sup>a</sup>Isomorphic to the  $C_{11}$  point group.  $\varphi$  is the helical angle.

This expected behavior is reproduced with the maximum deviation from zero frequencies being  $31i$   $\text{cm}^{-1}$ . These imaginary-frequency modes are observed only at  $\theta \approx 0$  and  $\varphi$  and their magnitudes are small, indicating that they are numerical errors due to the distance-based truncation of the force-constant matrices. The structure given in Table 13 is, therefore, a local minimum, and isotactic polyazane can exist at zero temperature and pressure (ignoring the zero-point vibrational energy). The predicted frequencies of the IR and Raman bands in Table 14 are expected to overestimate the (unavailable) experimental results by a few percent, judging from the results for the organic polymers (Secs. 3.1–3.3).

Table 15: Binding energy (in kcal/mol) of  $(\text{N}_2\text{H}_2)_x$ .

Method	<i>trans</i> - $\text{N}_2\text{H}_2^a$	<i>cis</i> - $\text{N}_2\text{H}_2^b$	$\text{N}_2 + \text{NH}_3^c$
B3LYP/cc-pVDZ	7.5	12.4	-42.1
MBPT(2)/cc-pVDZ	7.7	13.2	-50.1

<sup>a</sup>The energy difference between the unit-cell energy of  $(\text{N}_2\text{H}_2)_x$  and the energy of *trans*- $\text{N}_2\text{H}_2$  in their respective B3LYP/cc-pVDZ-optimized geometries. <sup>b</sup>The energy difference between the unit-cell energy of  $(\text{N}_2\text{H}_2)_x$  and the energy of *cis*- $\text{N}_2\text{H}_2$  in their respective B3LYP/cc-pVDZ-optimized geometries. <sup>c</sup>The energy difference between the unit-cell energy of  $(\text{N}_2\text{H}_2)_x$  and two thirds of the energy of  $\text{N}_2 + \text{NH}_3$  in their respective B3LYP/cc-pVDZ-optimized geometries.

Table 15 summarizes the binding energy of polyazane relative to its monomer (diazene) or to  $\text{N}_2$  and  $\text{NH}_3$ . The diazene molecule exists in either the *trans* or *cis* isomers with the former being slightly more stable. The positive binding energies mean that polyazane is stable against dissociation into diazenes. In contrast, the dissociation into  $\text{N}_2$  and  $\text{NH}_3$  is highly exothermic. This underscores the disproportionate strength of the  $\text{N}\equiv\text{N}$  bond as compared with the  $\text{N}=\text{N}$  and  $\text{N}-\text{N}$  bonds.

Figure 19 plots the unrelaxed reaction energy profile of polyazane’s dissociation into monomers. The unit-cell structure has the *gauche* conformation<sup>15,16</sup> with the predicted HNNH dihedral angle of  $75.5^\circ$ . Therefore, an considerable amount of internal rotation must take place during the dissociation into either *trans*- or *cis*-diazenes, causing the energy profile to rise to a much higher level than that of either diazene isomer, adding to the kinetic stability of polyazane. The dissociation into  $\text{N}_2$  and  $\text{NH}_3$  should involve even more significant rearrangements of atoms, including  $\text{N}-\text{H}$

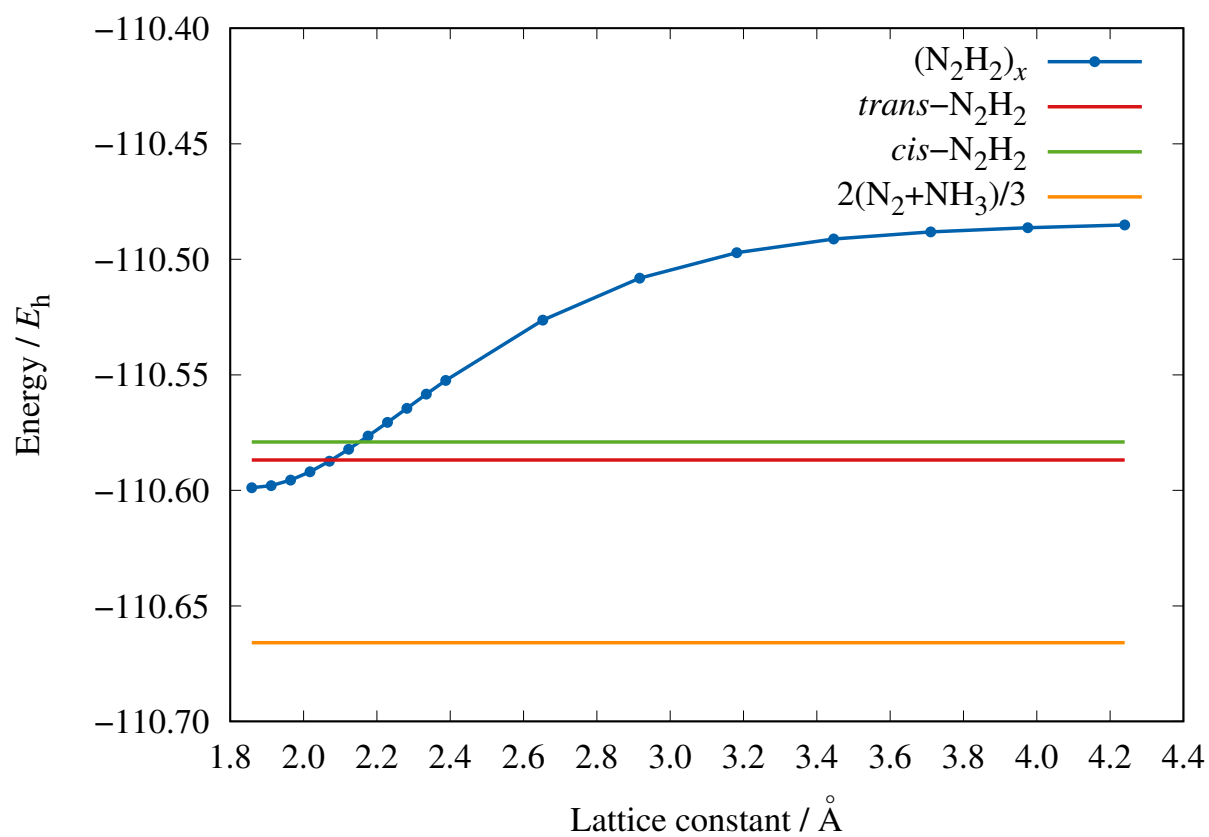


Figure 19: Unit-cell energy of  $(\text{N}_2\text{H}_2)_x$  as a function of the lattice constant computed by B3LYP/cc-pVDZ.

bond breaking and formation, likely creating a steeper activation barrier. We, therefore, expect polyazane to be kinetically stable, while unstable toward thermolysis. Theoretically, it can exist as a metastable species at low temperatures if not under ambient conditions.

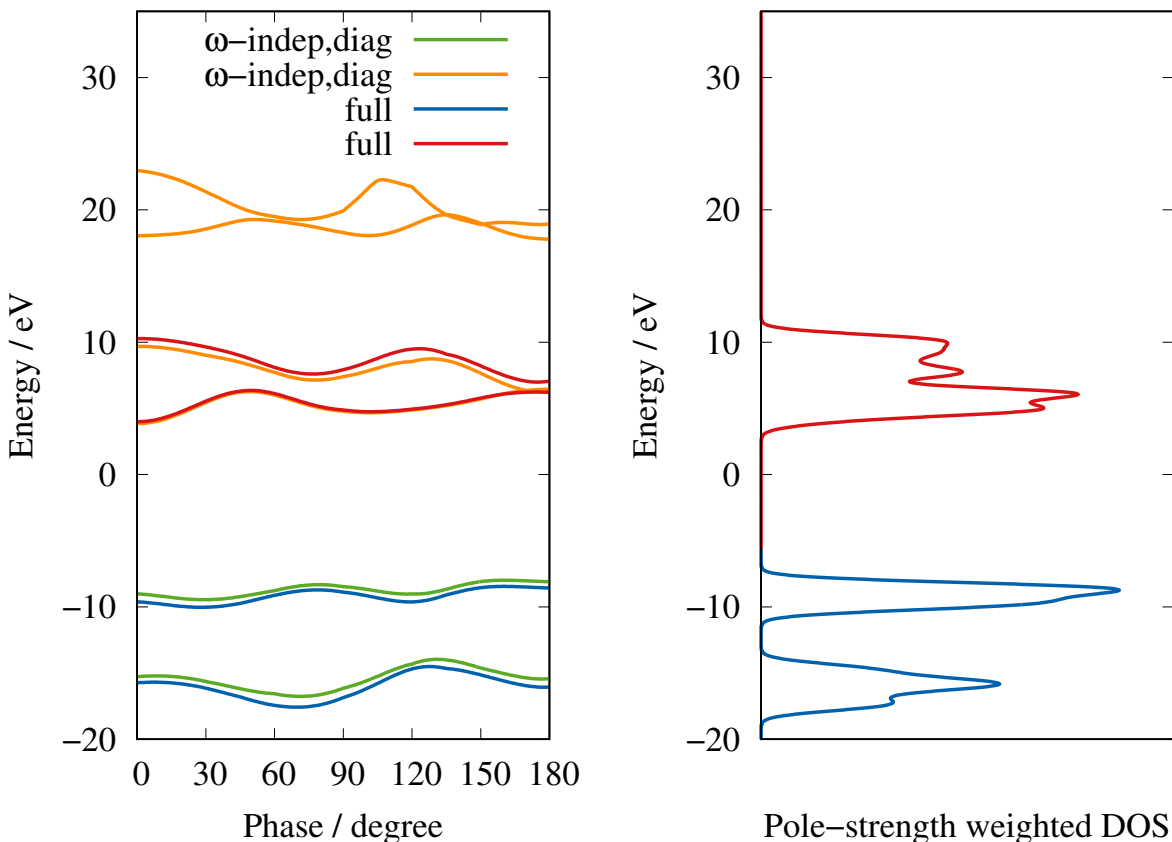


Figure 20: Electronic energy bands and DOS of  $(\text{NH})_x$  computed by MBGF(2)/cc-pVDZ. The DOS is weighted by the pole strength of Eq. (28) and convoluted with a Gaussian of a FWHM of 1 eV.

The calculated energy bands and electronic DOS are shown in Fig. 20. The top two valence bands have small dispersions and, therefore, the UPS of polyazane is predicted to have two sharp peaks in the range of 0–20 eV. The valence band edge occurs at  $-8.5$  eV at  $\theta = 160^\circ$ , which should be within a few tenths of an electronvolt of the exact value. Owing to this relatively large ionization energy, polyazane is expected to be stable in the air, but will likely undergo an acid-catalyzed decomposition in solutions.

### 3.6 Isotactic polyfluoroazane, $(\text{NF})_x$

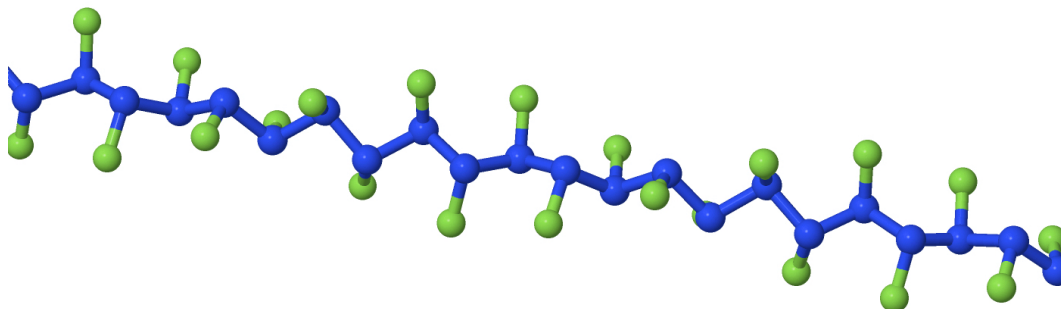


Figure 21: Isotactic polyfluoroazane,  $(\text{NF})_x$ .

In addition to hydrogenation (Sec. 3.5), we consider fluorination to stabilize the catenated nitrogen bonds,<sup>277</sup> leading to isotactic polyfluoroazane  $(\text{NF})_x$  (Fig. 21). It is a nitrogen analog of polytetrafluoroethylene (Sec. 3.3) and adopts a helical conformation. The logic underlying the expected stability of fluorinated nitrogen chains is concisely summarized by Krumm *et al.*,<sup>278</sup> who synthesized hexakis(trifluoromethyl)tetrazane  $\text{N}_4(\text{CF}_3)_6$ : “While no element can compete with carbon in the number of contiguous atoms in saturated chemical compounds, stable straight-chain species composed of other elements are known, especially if fluorine atoms, fluorinated groups, or other electronegative species are present in the molecule, for example  $\text{CF}_3(\text{O})_n\text{CF}_3$  ( $n = 1 - 3$ ) and  $\text{O}_n\text{F}_2$  ( $n = 1, 2, 4$ ). Fluorinated  $\text{N}_n$  compounds do exist and do exhibit surprising hydrolytic, thermal, and chemical stabilities. In contrast, the hydrogen-substituted analogues such as diazane, triazane, and tetrazane are increasingly unstable with increasing chain length.”<sup>278</sup> Employing the same strategy, Criton *et al.*<sup>17</sup> synthesized helical polyazanes up to pentazane substituted by electron-withdrawing carbamate groups. Other substituted triazane<sup>279,280</sup> and tetrazane<sup>281–283</sup> were also reported.

In this study, we applied B3LYP/cc-pVDZ and 6-31G\*\* for geometry optimization, phonon dispersion and phonon DOS calculations with  $S = 8$ ,  $L = 12$ , and  $K = 48$  using a NF group as the rototranslational (physical) repeat unit. The subsequent MBGF(2)/cc-pVDZ calculation for the quasiparticle energy bands and electronic DOS invoked the frozen-core and mod-6 approximations. The force-constant matrices extending to the ninth nearest neighbor NF groups were included in



the normal-mode analysis.

Table 16: Structural parameters of  $(\text{NF})_x$  and  $\text{N}_2\text{F}_2$ .

Method	$(\text{NF})_x$						$\varphi^b$	<i>cis</i> - $\text{N}_2\text{F}_2$		
	$r(\text{NN})$	$r(\text{NF})$	$a(\text{NNN})$	$a(\text{FNN})$	$d(\text{NNNN})$	$d(\text{FNNF})$		$r(\text{NN})$	$r(\text{NF})$	$a(\text{FNN})$
B3LYP/6-31G**	1.509 Å	1.396 Å	102.0°	103.0°	153.7°	156.6°	159.6°	1.220 Å	1.392 Å	114.3°
B3LYP/cc-pVDZ	1.510 Å	1.395 Å	102.0°	103.4°	152.0°	155.3°	158.3°	1.219 Å	1.392 Å	114.6°
Observed <sup>a</sup>							(160.0°) <sup>c</sup>	1.214 Å	1.384 Å	114.5°

<sup>a</sup>The *cis*-difluorodiazene structure from Hellwege and Hellwege.<sup>176</sup> <sup>b</sup>The helical angle [Eqs. (1)–(3)]. <sup>c</sup>The helical angle for a 9/4 helix (not observed) is given in parentheses.

The optimized equilibrium structure of isotactic polyfluoroazane is given in Table 16. The calculated helical angle is 158–160°. A commensurable helix with a similar helical angle (160°) is 9/4. It may be recalled that polytetrafluoroethylene also has a similar helical angle of 166°. As before, we can safely expect the predicted structural parameters to be accurate to within a few hundredths of one Ångstrom and a few degrees. However, the observed N–N bond length of hexakis(trifluoromethyl)tetrazane,  $\text{N}_4(\text{CF}_3)_6$ , is 1.379 Å,<sup>278</sup> which is considerably shorter than the calculated N–N bond length (1.51 Å) of polyfluoroazane. This is in spite of the bulkier  $\text{CF}_3$  substituent on every nitrogen in the former. Thus, these two sets of results may be considered incompatible with each other. Note that the observed N–N bond lengths in cyclo- $\text{N}_3\text{H}_3$ <sup>264</sup> and hydrazine<sup>276</sup> are 1.49 Å and 1.46 Å, respectively, which seem more in line with our calculated N–N bond length (1.51 Å) of polyfluoroazane.

The calculated NNNN and FNNF dihedral angles fall in the range of 152–157°. The same dihedral angle is subtended by the adjacent lone pairs. This is consistent with the rationalization in terms of the *gauche* effect,<sup>14–16</sup> although such a qualitative explanation may be less pertinent in light of the present quantitative calculations. The measured NNNN dihedral angle in hexakis(trifluoromethyl)tetrazane,  $\text{N}_4(\text{CF}_3)_6$ , is 95.2°,<sup>278</sup> which is considerably smaller than the corresponding predicted value (152–154°) in polyfluoroazane. The cause of this disparity is also unknown.

Figure 22 presents the calculated phonon dispersion curves and phonon DOS. There are four optical (green) and two acoustic (red) branches. The frequencies of the latter should become zero at  $\theta = 0$  (longitudinal and spinning) and  $\theta = \varphi$  (transverse), which is borne out numerically with

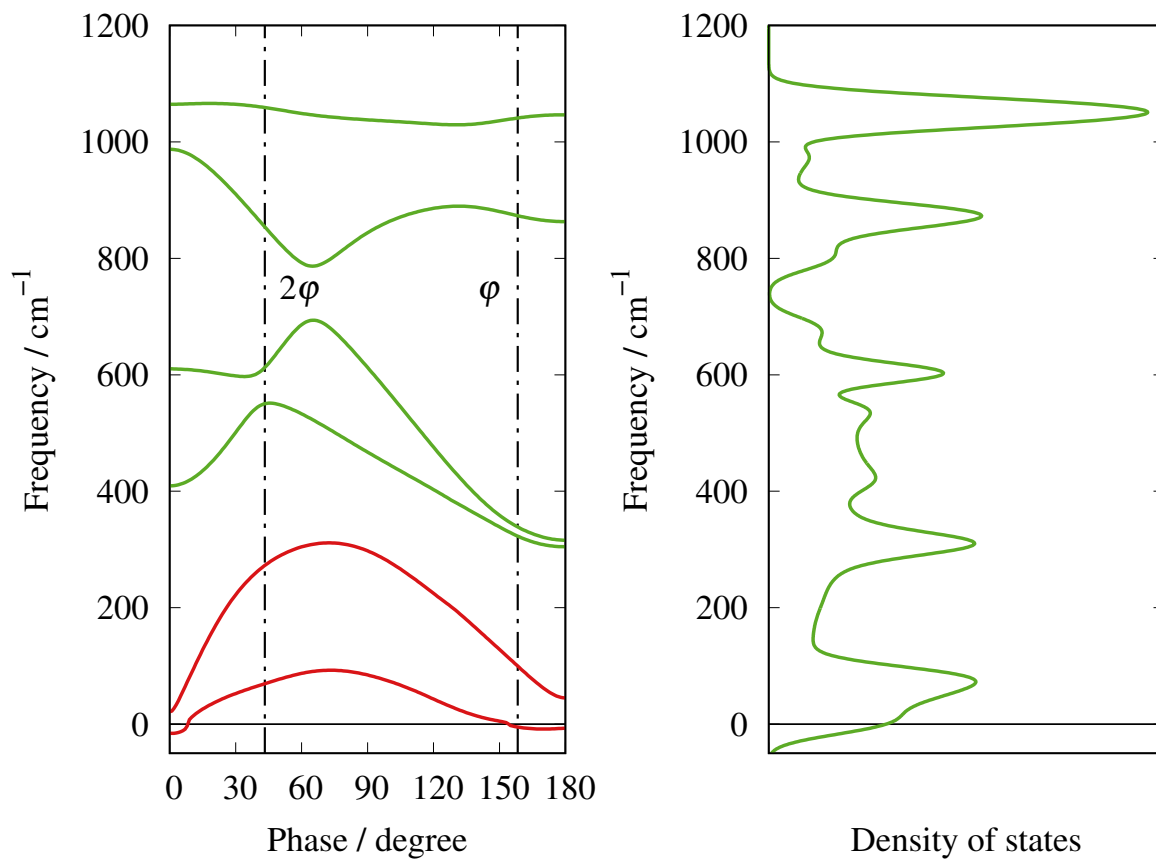


Figure 22: Phonon dispersion curves and DOS of  $(\text{NF})_x$  computed by B3LYP/6-31G\*\*. The DOS is convoluted with a Gaussian of a FWHM of  $40 \text{ cm}^{-1}$ .

Table 17: Vibrational frequencies (in  $\text{cm}^{-1}$ ) of  $(\text{NF})_x$ .

Irrep. <sup>a</sup> ; phase; activity	B3LYP/6-31G**
$A$ ; $\theta = 0$ ; IR, Raman	1064.5
	987.4
	610.2
	409.3
$E_1$ ; $\theta = \varphi$ ; IR, Raman	1041.0
	873.1
	338.6
	322.8
	99.6
$E_2$ ; $\theta = 2\varphi$ ; Raman	1059.0
	854.0
	612.5
	550.3
	272.6
	69.5

<sup>a</sup>Isomorphic to the  $C_9$  point group.  $\varphi$  is the helical angle.

errors of only 16i, 21, and 5i cm<sup>-1</sup>. Clearly, they are caused by the distance-based truncation of force-constant matrices. Imaginary-frequency modes occurring in the range of 160° ≤ θ ≤ 180° are due to the zero-frequency acoustic mode at θ = φ and the periodic nature of the phonon dispersion, and do not imply an instability of the structure. In fact, the same numerical errors with similar magnitude are detected in the phonon dispersion of polytetrafluoroethylene (Fig. 10). Therefore, the structure of Table 16 is a local minimum, and polyfluoroazane exists at zero temperature in a vacuum, ignoring the zero-point vibrations.

The frequencies of the IR- and/or Raman-active modes, occurring at θ = 0, φ, and 2φ, are compiled in Table 17. They should be reliable with a tendency of systematic overestimation by a few percent.

Table 18: Binding energy (in kcal/mol) of (N<sub>2</sub>F<sub>2</sub>)<sub>x</sub>.

Method	<i>trans</i> -N <sub>2</sub> F <sub>2</sub> <sup>a</sup>	<i>cis</i> -N <sub>2</sub> F <sub>2</sub> <sup>b</sup>	N <sub>2</sub> +NF <sub>3</sub> <sup>c</sup>
B3LYP/cc-pVDZ	-30.1	-33.0	-64.5
MBPT(2)/cc-pVDZ	-31.4	-34.1	-73.8

<sup>a</sup>The energy difference between the unit-cell energy of (N<sub>2</sub>F<sub>2</sub>)<sub>x</sub> and the energy of *trans*-N<sub>2</sub>F<sub>2</sub> in their respective B3LYP/cc-pVDZ-optimized geometries. <sup>b</sup>The energy difference between the unit-cell energy of (N<sub>2</sub>F<sub>2</sub>)<sub>x</sub> and the energy of *cis*-N<sub>2</sub>F<sub>2</sub> in their respective

B3LYP/cc-pVDZ-optimized geometries. <sup>c</sup>The energy difference between the unit-cell energy of (N<sub>2</sub>F<sub>2</sub>)<sub>x</sub> and two thirds of the energy of N<sub>2</sub>+NF<sub>3</sub> in their respective B3LYP/cc-pVDZ-optimized geometries.

Table 18 compiles the binding energies of polyfluoroazane relative to dissociation into its monomers (*trans*- or *cis*-difluorodiazenes) or into dinitrogen and nitrogen trifluoride. Note that, unlike diazenes, the *cis* isomer of difluorodiazene is more stable than the *trans* isomer by 1.4 kcal/mol at 298 K.<sup>284</sup> The negative values across the board in Table 18 mean that polyfluoroazane is thermodynamically unstable and seems even less stable than polyazane (Sec. 3.5). Contrary to the expectation that fluorination will stabilize the catenated nitrogen bonds,<sup>278</sup> it seems to have the opposite effect. This may be because perfluorination stabilizes the short nitrogen chains to a greater degree than it does longer ones.

The unrelaxed energy profile in Fig. 23 corresponds to the dissociation into highly stretched, slightly twisted *trans*-difluorodiazenes. Unlike the corresponding energy profile for polyazane

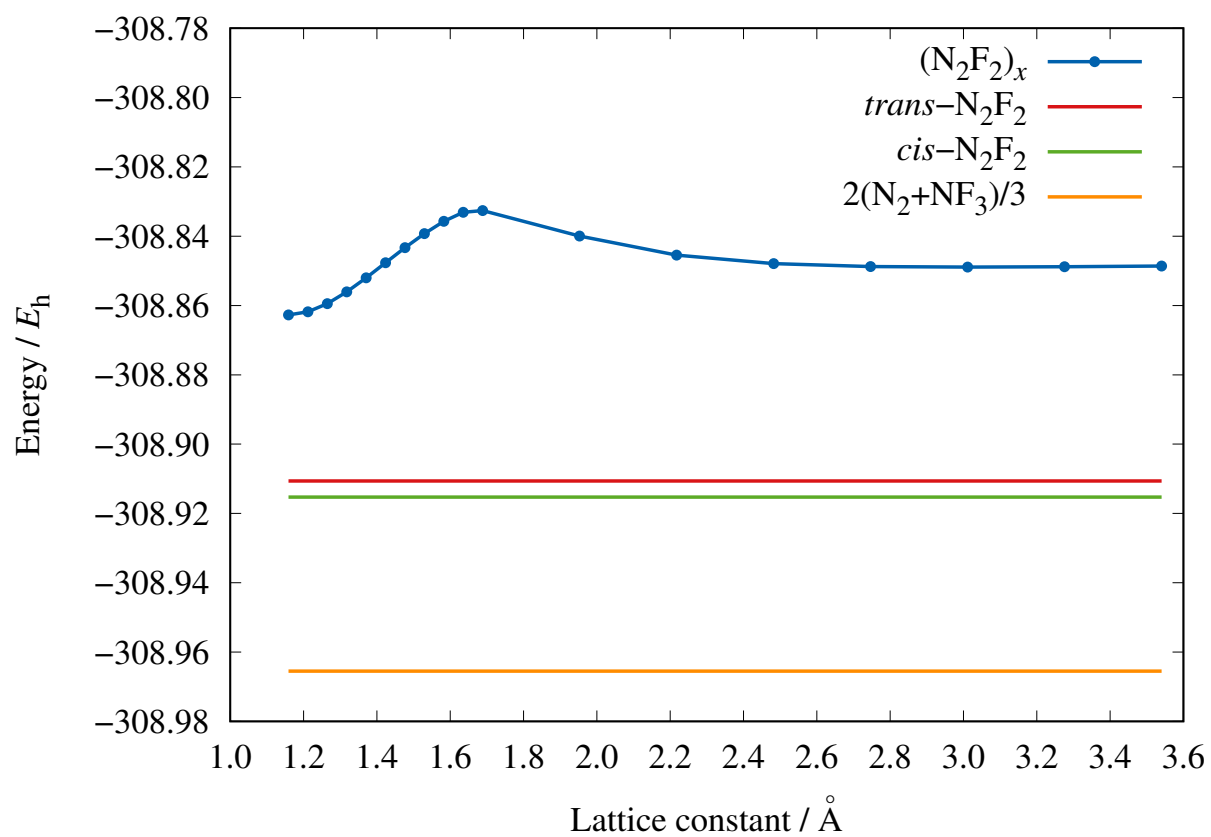


Figure 23: Unit-cell energy of  $(\text{N}_2\text{F}_2)_x$  as a function of the lattice constant computed by B3LYP/cc-pVDZ.

(Fig. 19), it is not a monotonically increasing function of the lattice constant, but displays a low activation barrier of *ca.* 20 kcal/mol, which will be made even lower by geometry optimization of the transition state. Polyfluoroazane is, therefore, expected to possess limited kinetic stability if any, and it may readily undergo thermolysis. Therefore, polyfluoroazane is unlikely to exist under ambient conditions, contrary to the theoretical expectation and experimental findings for short catenated nitrogen molecules.<sup>278</sup>

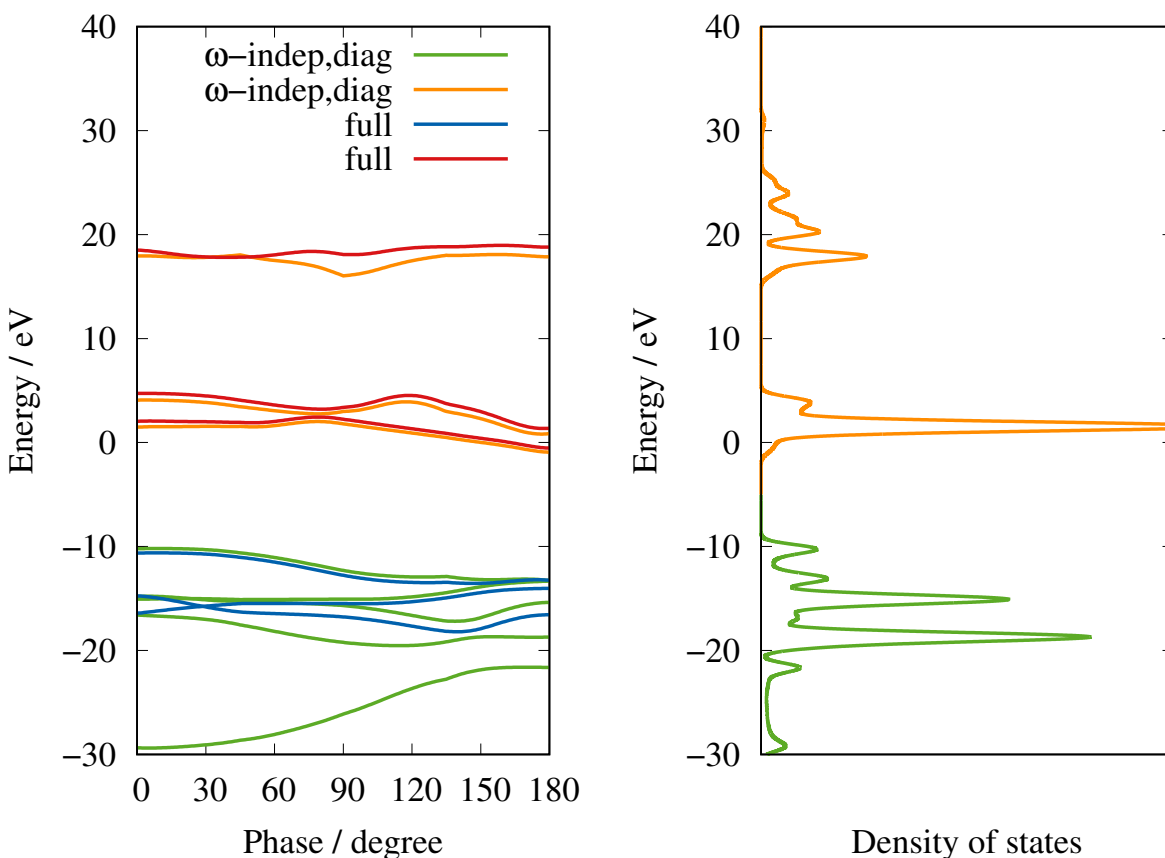


Figure 24: Electronic energy bands and DOS of  $(\text{NF})_x$  computed by MBGF(2)/cc-pVDZ. The DOS is convoluted with a Gaussian of a FWHM of 1 eV.

Figure 24 shows the quasiparticle energy bands and electronic DOS of polyfluoroazane computed by MBGF(2)/cc-pVDZ. The convoluted DOS due to valence bands is expected to be an accurate prediction of UPS with errors in peak positions being no more than a few tenths of an electronvolt.

### 3.7 Polyoxane, (O)<sub>x</sub>

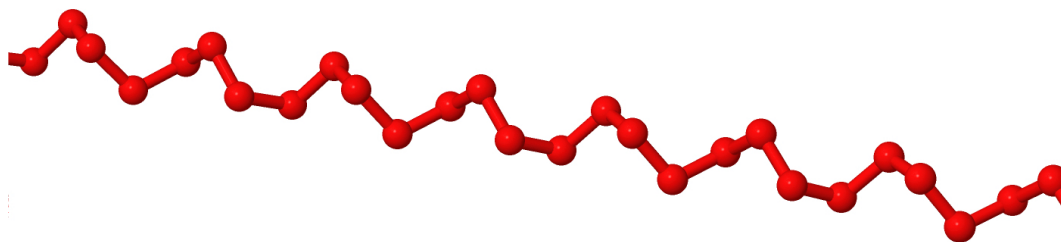


Figure 25: Polyoxane, (O)<sub>x</sub>.

A helical polymeric form of oxygen, polyoxane (Fig. 25), may be implied by its stable sulfur homologue, helical polysulfane.<sup>42</sup> Computational and experimental searches for long catenated forms of oxygen have been carried out using both the chemistry and physics approaches.

In the chemistry approach, oxygen allotropes of various structures were computationally characterized. They include O<sub>4</sub>,<sup>285–290</sup> O<sub>6</sub>,<sup>288,290,291</sup> O<sub>8</sub>,<sup>288</sup> and O<sub>12</sub>.<sup>288</sup> Among these, cyclo-O<sub>6</sub> is found to be stable in the cyclohexane-like chair conformation.<sup>290</sup> This may be auspicious for polyoxane since cyclo-(O)<sub>6</sub> is to polyoxane as cyclohexane is to polyethylene.

McKay and Wright<sup>2</sup> computationally explored longer members of the hydrogen peroxide series H(O)<sub>n</sub>H, whose sulfur homologues H(S)<sub>n</sub>H are known to exist. They found<sup>2</sup> that the bond dissociation energy reaches a minimum at H<sub>2</sub>O<sub>6</sub>, and then turns to increase for a longer chain, suggesting that an infinite chain may be relatively stable. Martins-Costa *et al.*<sup>18,292</sup> computationally studied H(O)<sub>n</sub>H with up to  $n = 10$ , revealing that longer chains adopt a helical conformation with bond-length alternation. They also showed that the heats of formation become negative for H<sub>2</sub>O<sub>6</sub> and longer, which are, therefore, metastable. See Refs.<sup>293,294</sup> for other computational studies of H<sub>2</sub>O<sub>3</sub> and H<sub>2</sub>O<sub>4</sub>.

Experimentally, H<sub>2</sub>O<sub>3</sub> has been detected by IR (Ref.<sup>295</sup>) and microwave spectroscopies<sup>296</sup> and H<sub>2</sub>O<sub>3</sub> and H<sub>2</sub>O<sub>4</sub> by Raman spectroscopy.<sup>297</sup> Substitution with electron-withdrawing fluorine terminal groups will enhance the stability considerably.<sup>277</sup> Hence, the syntheses of perfluorinated polyoxanes as long as F<sub>2</sub>O<sub>5</sub> and F<sub>2</sub>O<sub>6</sub> were reported by Streng and Grosse,<sup>298</sup> hinting at an intrin-

sic ability of oxygens to form longer consecutive bonds.

In the physics approach, Gorelli *et al.*<sup>299,300</sup> observed a pressure-induced transition to the  $\epsilon$  phase of solid oxygen. This was accompanied by a dramatic color change with strong IR bands emerging at 300–600  $\text{cm}^{-1}$ , suggesting condensation of multiple  $\text{O}_2$  molecules into a longer catenated form. These authors ruled out polymeric forms with more than four atoms.<sup>300</sup> Neaton and Ashcroft<sup>8</sup> computationally proposed a linear herringbone (zigzag chain) structure in the pressure range corresponding to the  $\epsilon$  phase. Their predicted IR and Raman band positions were said to be consistent with the observed.<sup>299,300</sup> However, Goncharov *et al.*<sup>301</sup> measured the Raman spectra of the  $\epsilon$  phase, and concluded that the results were inconsistent with the herringbone structure. A subsequent computational study by Bartolomei *et al.*<sup>302</sup> also suggested that van-der-Waals clusters of the type  $(\text{O}_2)_4$  for the  $\epsilon$  phase. Despite the well-defined  $\text{O}_2$  molecular constituents, this structure is shown to have a singlet spin multiplicity and is consistent with the observed nonmagnetic character of this phase.<sup>303</sup> This interpretation was also compatible with an inelastic X-ray scattering study of Meng *et al.*,<sup>10</sup> once again ruling out the herringbone structure for the  $\epsilon$  phase in favor of the  $\text{O}_8$  structure.

Oganov and Glass,<sup>254</sup> using their pioneering evolutionary techniques, determined a helical polymeric form of oxygen as the most stable structure at 25 GPa, which is similar to the herringbone structure of Neaton and Ashcroft.<sup>8</sup> This is not surprising given the similarity of DFT models (which consist in LDA or generalized gradient approximation) underlying both groups' simulations. Zhu *et al.*<sup>19</sup> also computationally predicted a new ( $\theta$ ) phase of solid oxygen made of 4/1-helical polymers at 2 TPa, which is structurally analogous to phase III of solid sulfur.

More recently, Hagiwara *et al.*<sup>304</sup> fashioned an antiferromagnetic one-dimensional chain of weakly interacting, non-catenated  $\text{O}_2$  molecules in a single-walled carbon nanotube (SWCNT). This may be contrasted with a long catenated metallic chain of sulfur formed in a SWCNT.<sup>305</sup>

In this study, we determined the structure, phonon dispersion, and phonon DOS of helical polyoxane at the B3LYP/cc-pVDZ or 6-31G\*\* level with  $S = 8$ ,  $L = 12$ , and  $K = 48$ . We then computed the quasiparticle energy bands and electronic DOS at the MBGF(2)/cc-pVDZ level with

the frozen-core and mod-4 approximations, using a single oxygen atom as the rototranslational (physical) repeat unit. We employed the ninth-nearest-neighbor approximation in the normal-mode analysis.

Table 19: Structural parameters of  $(\text{O})_x$  and  $\text{O}_2$ .

Method	$(\text{O})_x$				$\text{O}_2 (^1\Delta_g)$	$\text{O}_2 (^3\Sigma_g^-)$
	$r(\text{OO})$	$a(\text{OOO})$	$d(\text{OOOO})$	$\varphi^a$	$r(\text{OO})$	$r(\text{OO})$
B3LYP/6-31G**	1.422 Å	108.1°	79.4°	102.9°	1.216 Å	1.215 Å
B3LYP/cc-pVDZ	1.420 Å	108.3°	78.9°	102.5°	1.210 Å	1.209 Å
PBE (2 TPa) <sup>19</sup>	1.153 Å	98.8°		90.0°		
Observed <sup>b</sup>				(102.9°) <sup>c</sup>	1.216 Å	1.208 Å

<sup>a</sup>The helical angle. <sup>b</sup>The  $\text{O}_2$  structures from Huber and Herzberg.<sup>261</sup> <sup>c</sup>The helical angle for a 7/2 helix (not observed) is given in parentheses.

The calculated equilibrium structure of polyoxane is given in Table 19. It is predicted to have a 7/2-helical structure with the helical angle of  $\varphi = 103^\circ$ . This angle is not dissimilar from the one ( $\varphi = 90^\circ$ ) in the 4/1-helical structure predicted<sup>19</sup> under an immense pressure of 2 TPa. However, the O–O bond lengths are vastly different between these two pressures: it is 1.42 Å in our calculation under zero pressure, while 1.15 Å under 2 TPa,<sup>19</sup> the latter being even shorter than the O=O bond in the singlet or triplet  $\text{O}_2$  molecule in the gas phase.

Table 20: Vibrational frequencies (in  $\text{cm}^{-1}$ ) of  $(\text{O})_x$ .

Irrep. <sup>a</sup> ; phase; activity	B3LYP/6-31G**
$A_1$ ; $\theta = 0$ ; Raman	909.4
$E_1$ ; $\theta = \varphi$ ; IR, Raman	806.1
	654.4
$E_2$ ; $\theta = 2\varphi$ ; Raman	662.5
	350.7
	172.9

<sup>a</sup>Isomorphic to the  $D_7$  point group.  $\varphi$  is the helical angle.

The phonon dispersion curves and phonon DOS are drawn in Fig. 26. With only one atom in the rototranslational unit, there are one optical (green) and two acoustic (red) branches. The acoustic branches exhibit the expected behavior of having zero frequencies at  $\theta = 0$  and  $\varphi$  with the maximum error of  $25i \text{ cm}^{-1}$ . Therefore, the structure of Table 19 is unambiguously a local minimum, and there is no bond-length alternation<sup>18,292</sup> according to our calculation. The Raman



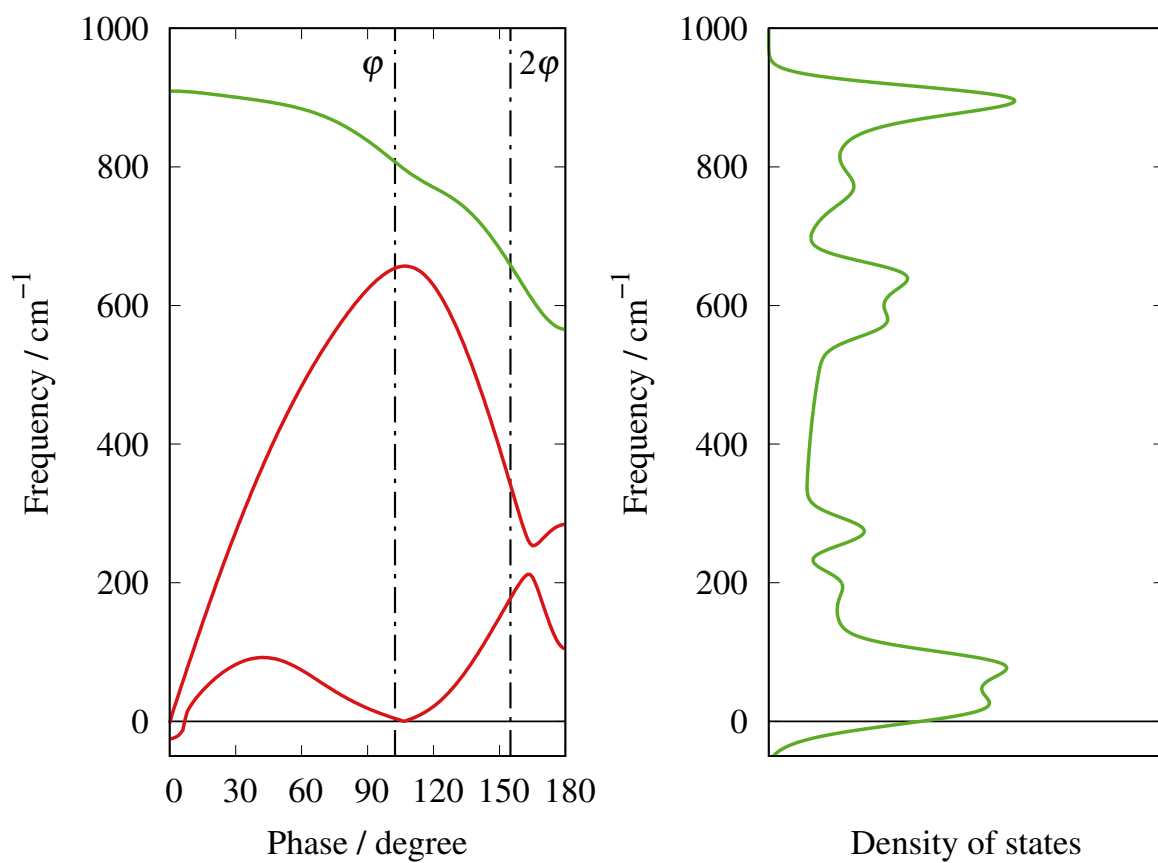


Figure 26: Phonon dispersion curves and DOS of  $(\text{O})_x$  computed by B3LYP/6-31G\*\*. The DOS is convoluted with a Gaussian of a FWHM of  $40 \text{ cm}^{-1}$ .

bands from  $\text{H}_2\text{O}_3$  are observed at 500, 756, and  $878\text{ cm}^{-1}$  and those from  $\text{H}_2\text{O}_4$  at 449, 586, 624, 827, and  $865\text{ cm}^{-1}$ .<sup>297</sup> They mostly fall on the optical branch (some possibly on the upper acoustic branch), and are consistent with our calculation.

According to Higgs' selection rules,<sup>191</sup> six modes are optically active: Two are IR active and all six are Raman active. Their calculated frequencies are given in Table 20, which are hoped to assist in future experimental identification. Goncharov *et al.*<sup>301</sup> detected seven Raman bands from the  $\epsilon$  phase at 260, 290, 580, 600, 625, 695, and  $1750\text{ cm}^{-1}$  under 65 GPa. While these frequencies must be considerably elevated by the high pressure, they are clearly incompatible with the predicted Raman band positions of polyoxane in Table 20. The phase transition to the  $\epsilon$  phase is accompanied by a strong IR absorption at  $300\text{ cm}^{-1}$  at 20 GPa.<sup>299,300</sup> This cannot be explained by the predicted IR band positions for polyoxane, either. These comparisons confirm the earlier conclusion<sup>299–301</sup> ruling out the polyoxane-like structure for the  $\epsilon$  phase. The observed Raman bands<sup>301</sup> from the  $\zeta$  phase at 260, 440, 640, 700, 760, 830, and  $1750\text{ cm}^{-1}$  under 135 GPa are also inconsistent with the polyoxane structure.

Figure 27 shows the calculated quasiparticle energy bands and electronic DOS. The valence band edge is located at  $-10.6\text{ eV}$  according to MBGF(2)/cc-pVDZ with the “full” self-energy, and this value should be accurate to within a few tenths of an electronvolt. The conduction band edge is  $0.2\text{ eV}$ , which is too high. The amount of overestimation in the conduction band edge was  $0.4\text{ eV}$  in electronegative polytetrafluoroethylene and  $4.6\text{ eV}$  in polyethylene. The corresponding value for moderately electronegative polyoxane may fall somewhere in between these two values. The fundamental band gap is, therefore, direct and in the range of  $6.1\text{--}10.8\text{ eV}$ . In comparison, the ultra-high-pressure  $\theta$  phase (a  $4/1$  helix) was predicted<sup>19</sup> to be an insulator with a band gap of  $3.2\text{ eV}$  or  $5.9\text{ eV}$  according to the nonhybrid PBE or hybrid HSE functional, respectively. The valence DOS in Fig. 27 should be predictive of the UPS of polyoxane without an energy shift.

Table 21 compiles the binding energy of polyoxane relative to its monomer  $\text{O}_2$ . Polyoxane is metastable with respect to triplet  $\text{O}_2$ . Remarkably, it is thermodynamically stable against dissociation into singlet  $\text{O}_2$  according to the electron-correlated treatments. Figure 28 indicates that the

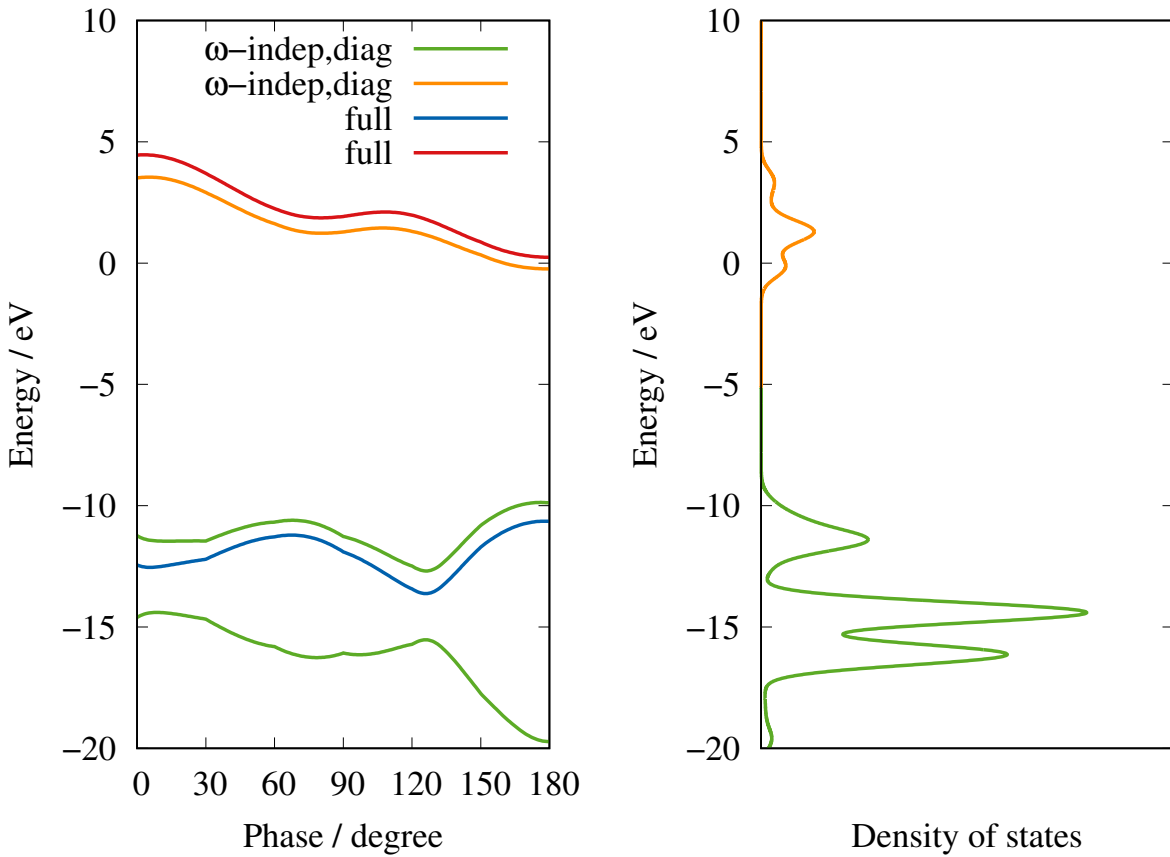


Figure 27: Electronic energy bands and DOS of  $(\text{O}_2)_x$  computed by MBGF(2)/cc-pVDZ. The DOS is weighted by the pole strength of Eq. (27) and convoluted with a Gaussian of a FWHM of 1 eV.

Table 21: Binding energy (in kcal/mol) of  $(\text{O}_2)_x$ .

Method	$\text{O}_2 (^1\Delta_g)^a$	$\text{O}_2 (^3\Sigma_g^-)^b$
B3LYP/cc-pVDZ	13.8	-25.7
MBPT(2)/cc-pVDZ	3.3	-29.3

<sup>a</sup>The energy difference between the unit-cell energy of  $(\text{O}_2)_x$  and the energy of the singlet  $\text{O}_2$  in their respective B3LYP/cc-pVDZ-optimized geometries. <sup>b</sup>The energy difference between the unit-cell energy of  $(\text{O}_2)_x$  and the energy of the triplet  $\text{O}_2$  in their respective B3LYP/cc-pVDZ-optimized geometries.

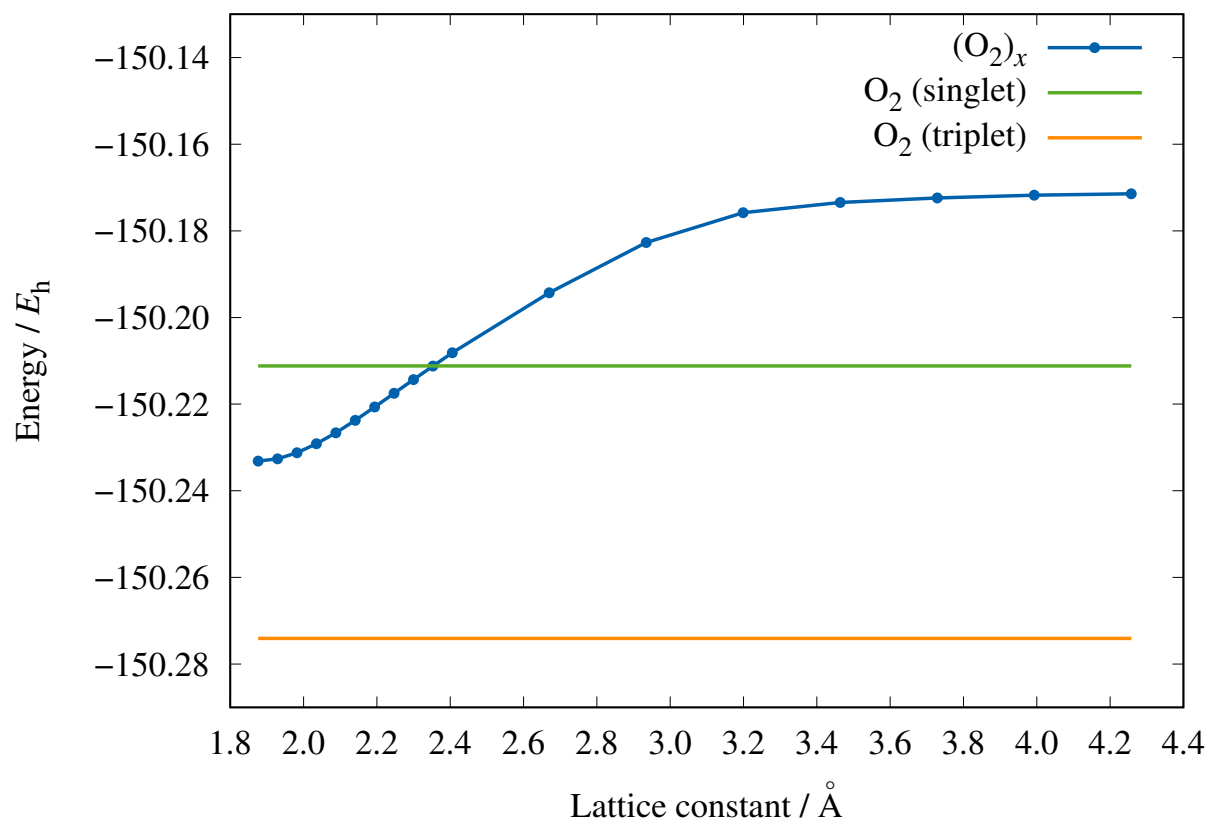


Figure 28: Unit-cell energy of  $(\text{O}_2)_x$  as a function of the lattice constant computed by B3LYP/cc-pVDZ.

unrelaxed dissociation reaction energy profile is a monotonically increasing function of the lattice constant, although this may be a computational artifact because the spin-restricted formulation compels the dissociation products to be singlet. Comparison with similar energy profiles of the organic polymers (Secs. 3.1–3.3) nonetheless suggests that polyoxane may also be kinetically stable.

## 4 Conclusions

In this article, we have reported an implementation of the *ab initio* Gaussian-basis-set MBGF(2) method for an infinite helical polymer. It can compute the quasiparticle energy bands and pole strengths in the extended-zone scheme with or without the diagonal and frequency-independent approximations to the self-energy. It simultaneously evaluates the MBPT(2) correction to the energy per the smallest rototranslational (physical) repeat unit. Together with the Gaussian-basis-set DFT method<sup>52</sup> for energy and analytical gradients with respect to atomic positions, translational period, and helical angle, it can simulate ARUPS, UPS, IR and Raman band positions, phonon dispersion curves, and INS spectra of infinite helical polymers even with incommensurable structures, which cannot be handled well by either a molecular or solid-state method.

Through applications to several well-characterized organic polymers, i.e., polyethylene, polyacetylene, and polytetrafluoroethylene, we have demonstrated the predictive accuracy of B3LYP/cc-pVDZ or 6-31G\*\* for structures, phonon dispersion curves, and phonon DOS and of MBGF(2)/cc-pVDZ for valence bands and valence DOS, if not for conduction bands or fundamental band gaps. The measured bond lengths and angles of these organic polymers are reproduced within a few hundredths of one Ångström and a few degrees. The vibrational frequencies are systematically overestimated by a few percent, but they are accurate enough for reliable band assignments of their IR, Raman, and INS spectral bands. The valence bands and DOS have negligible dependence on the diagonal and frequency-independent approximations and are within a few tenths of an electronvolt or a typical experimental error bar of the observed energy bands or photoelectron spectral peaks. The band gaps are overestimated by 0.4–4.1 eV, depending on the nature of the conduction

bands.

Armed with these predictive methods for helical polymers, we have explored the possibilities of the kinetically-trapped metastable existence of second-row-element inorganic polymers under ambient conditions, notwithstanding the obvious difficulties of their synthesis and isolation. All-*trans* polyazene ( $\text{N}_2$ )<sub>x</sub> is isoelectronic with all-*trans* polyacetylene and an insulator with bond-length alternation. Various isomers including the *trans*-transoid are both thermodynamically and mechanically unstable with a propensity to spontaneously dissociate into  $\text{N}_2$  fragments during geometry optimizations. On the other hand, isotactic polyazane ( $\text{NH}$ )<sub>x</sub>, which is a nitrogen analog of polyethylene, is thermodynamically stable in its 11/3-helical conformation against dissociation into its monomers. It is not thermodynamically stable against dissociation into  $\text{N}_2$  and  $\text{NH}_3$ , but such dissociation reaction involves N–H bond breaking and formation and likely has a high activation barrier. It may, therefore, exist at low temperatures, although it is likely unstable in solutions. Contrary to theoretical expectations and experimental findings for short chains, perfluorinated polyazane or isotactic polyfluoroazane ( $\text{NF}$ )<sub>x</sub> in its 9/4-helical conformation seems no more stable than polyazane either thermodynamically or kinetically. This may be because the fluorination stabilizes the smaller dissociation products (difluorodiazenes or trifluoroamine) more than it does the polymer. The 7/2-helical polyoxane ( $\text{O}$ )<sub>x</sub> is thermodynamically stable with respect to singlet  $\text{O}_2$ . It also seems kinetically stable against dissociation into triplet  $\text{O}_2$ . Echoing with previous computational predictions of the existence of (helical) polyoxane under high pressures,<sup>8,19,254</sup> our calculation supports its possible metastable existence at low pressures and temperatures. The IR and Raman band positions, INS spectra, and (AR)UPS of these polymers have been predicted in order to assist in their experimental detections.

## 5 Acknowledgements

SH is indebted to The Late Professor Mitsuo Tasumi of the University of Tokyo for decades of encouragements and tutelage especially in the area of polymer spectroscopy. He was supported by

the U.S. Department of Energy (DoE), Office of Science, Office of Basic Energy Sciences under Grant No. DE-SC0006028. SH is a Guggenheim Fellow of the John Simon Guggenheim Memorial Foundation. He also thanks the hospitality of University of Tsukuba, where the initial phase of this study was conducted.

SSX was supported by the Center for Scalable Predictive methods for Excitations and Correlated phenomena (SPEC), which is funded by the U.S. DoE, Office of Science, Office of Basic Energy Sciences, Division of Chemical Sciences, Geosciences and Biosciences as part of the Computational Chemical Sciences (CCS) program at Pacific Northwest National Laboratory (PNNL) under FWP 70942. PNNL is a multi-program national laboratory operated by Battelle Memorial Institute for the U.S. DoE.

RJB was supported by the Air Force Office of Scientific Research under AFOSR (Award No. FA9550-19-1-0091).

This research used resources of the National Energy Research Scientific Computing Center (NERSC), a U.S. DoE Office of Science User Facility located at Lawrence Berkeley National Laboratory, operated under Contract No. DE-AC02-05CH11231 under NERSC award m3196 (2022).

## References

- (1) Glukhovtsev, M. N.; Jiao, H. J.; Schleyer, P. v. Besides N<sub>2</sub>, what is the most stable molecule composed only of nitrogen atoms? *Inorg. Chem.* **1996**, *35*, 7124–7133.
- (2) McKay, D. J.; Wright, J. S. How long can you make an oxygen chain? *J. Am. Chem. Soc.* **1998**, *120*, 1003–1013.
- (3) Bartlett, R. J. Exploding the Mysteries of Nitrogen. *Chemistry & Industry* **2000**, *4*, 140–143.
- (4) Steele, B. A.; Oleynik, I. I. Computational Discovery of New High-Nitrogen Energetic Materials. *Computational Approaches for Chemistry under Extreme Conditions* **2019**, *28*, 25–52.

- (5) O'Sullivan, O. T.; Zdilla, M. J. Properties and Promise of Catenated Nitrogen Systems As High-Energy-Density Materials. *Chem. Rev.* **2020**, *120*, 5682–5744.
- (6) Sabin, J. R., Ed. *Advances in Quantum Chemistry*; Elsevier, 2014; Vol. 69.
- (7) Shimizu, K.; Suhara, K.; Ikumo, M.; Eremets, M. I.; Amaya, K. Superconductivity in oxygen. *Nature* **1998**, *393*, 767–769.
- (8) Neaton, J. B.; Ashcroft, N. W. Low-energy linear structures in dense oxygen: Implications for the  $\epsilon$  phase. *Phys. Rev. Lett.* **2002**, *88*, 205503.
- (9) Ma, Y. M.; Oganov, A. R.; Glass, C. W. Structure of the metallic  $\zeta$ -phase of oxygen and isosymmetric nature of the  $\epsilon$ – $\zeta$  phase transition: *Ab initio* simulations. *Phys. Rev. B* **2007**, *76*, 064101.
- (10) Meng, Y.; Eng, P. J.; Tse, J. S.; Shaw, D. M.; Hu, M. Y.; Shu, J. F.; Gramsch, S. A.; Kao, C.; Hemley, R. J.; Mao, H. K. Inelastic x-ray scattering of dense solid oxygen: Evidence for intermolecular bonding. *Proc. Natl. Acad. Sci. USA* **2008**, *105*, 11640–11644.
- (11) Kimball, D. B.; Haley, M. M. Triazenes: A versatile tool in organic synthesis. *Angew. Chem. Int. Ed.* **2002**, *41*, 3338–3351.
- (12) Wright, J. S.; McKay, D. J. Polymeric oxygen and nitrogen: why not? *Sci. Prog.* **1999**, *82*, 151–170.
- (13) Manners, I. Polymers and the periodic table: Recent developments in inorganic polymer science. *Angew. Chem. Int. Ed.* **1996**, *35*, 1602–1621.
- (14) Wolfe, S. Gauche Effect. Some Stereochemical Consequences of Adjacent Electron Pairs and Polar Bonds. *Acc. Chem. Res.* **1972**, *5*, 102–111.
- (15) Mizushima, S. *Internal Rotation*; Academic Press: New York, 1954.



- (16) Mizushima, S.; Nakagawa, I.; Ichishima, I.; Miyazawa, T. Further Evidence for the Existence of the *Gauche*-Form of 1,2-Dichloroethane. *J. Chem. Phys.* **1954**, *22*.
- (17) Criton, T.; Vilona, D.; Jacob, G.; Médebielle, M.; Dumont, E.; Joucla, L.; Lacôte, E. Synthesis and Properties of Higher Nuclearity Polyazanes. *Chem. Eur. J.* **2021**, *27*, 3670–3674.
- (18) Martins-Costa, M.; Anglada, J. M.; Ruiz-Lopez, M. F. Hyperconjugation in adjacent OO bonds: Remarkable odd/even effects. *Chem. Phys. Lett.* **2009**, *481*, 180–182.
- (19) Zhu, L.; Wang, Z. W.; Wang, Y. C.; Zou, G. T.; Mao, H. K.; Ma, Y. M. Spiral chain O<sub>4</sub> form of dense oxygen. *Proc. Natl. Acad. Sci. USA* **2012**, *109*, 751–753.
- (20) McMahan, A. K.; LeSar, R. Pressure Dissociation of Solid Nitrogen under 1 Mbar. *Phys. Rev. Lett.* **1985**, *54*, 1929–1932.
- (21) Mailhot, C.; Yang, L. H.; McMahan, A. K. Polymeric Nitrogen. *Phys. Rev. B* **1992**, *46*, 14419–14435.
- (22) Eremets, M. I.; Gavriluk, A. G.; Trojan, I. A.; Dzivenko, D. A.; Boehler, R. Single-bonded cubic form of nitrogen. *Nature Mater.* **2004**, *3*, 558–563.
- (23) Eremets, M. I.; Gavriluk, A. G.; Trojan, I. A. Single-crystalline polymeric nitrogen. *Appl. Phys. Lett.* **2007**, *90*.
- (24) Schlegel, H. B.; Skancke, A. Thermochemistry, Energy Comparisons, and Conformational-Analysis of Hydrazine, Triazane, and Triaminoammonia. *J. Am. Chem. Soc.* **1993**, *115*, 7465–7471.
- (25) Zhao, M.; Gimarc, B. M. Strain Energies of (NH)<sub>n</sub> Rings,  $n = 3 - 8$ . *J. Phys. Chem.* **1994**, *98*, 7497–7503.
- (26) Del Re, G.; Ladik, J.; Biczó, G. Self-Consistent-Field Tight-Binding Treatment of Polymers. I. Infinite three-Dimensional Case. *Phys. Rev.* **1967**, *155*, 997.

- (27) André, J. M. Self-Consistent Field Theory for Electronic Structure of Polymers. *J. Chem. Phys.* **1969**, *50*, 1536.
- (28) Mintmire, J. W.; Sabin, J. R. Local Density Functional Methods in Two-Dimensionally Periodic Systems. I. The Atomic Hydrogen Monolayer. *Int. J. Quantum Chem.* **1980**, *17*, 707–713.
- (29) Mintmire, J. W.; Sabin, J. R.; Trickey, S. B. Local Density Functional Methods in two-Dimensionally Periodic-Systems: Hydrogen and Beryllium Monolayers. *Phys. Rev. B* **1982**, *26*, 1743–1753.
- (30) Kertész, M. Electronic Structure of Polymers. *Adv. Quantum Chem.* **1982**, *15*, 161–214.
- (31) Sun, J. Q.; Bartlett, R. J. Modern correlation theories for extended, periodic systems. *Top. Curr. Chem.* **1999**, *203*, 121–145.
- (32) Hirata, S. Quantum chemistry of macromolecules and solids. *Phys. Chem. Chem. Phys.* **2009**, *11*, 8397–8412.
- (33) Nakano, T.; Okamoto, Y. Synthetic helical polymers: Conformation and function. *Chem. Rev.* **2001**, *101*, 4013–4038.
- (34) Yashima, E.; Maeda, K.; Iida, H.; Furusho, Y.; Nagai, K. Helical Polymers: Synthesis, Structures, and Functions. *Chem. Rev.* **2009**, *109*, 6102–6211.
- (35) Imamura, A. Electronic Structures of Polymers Using Tight-Binding Approximation. I. Polyethylene by Extended Hückel Method. *J. Chem. Phys.* **1970**, *52*, 3168–3175.
- (36) Fujita, H.; Imamura, A. Electronic Structures of Polymers Using Tight-Binding Approximation. II. Polyethylene and Polyglycine by CNDO Method. *J. Chem. Phys.* **1970**, *53*, 4555.
- (37) Blumen, A.; Merkel, C. Energy-Band Calculations on Helical Systems. *Phys. Stat. Solidi B* **1977**, *83*, 425–431.

- (38) Teramae, H.; Yamabe, T.; Satoko, C.; Imamura, A. Energy Gradient in the Ab initio Hartree–Fock Crystal-Orbital Formalism of One-Dimensional Infinite Polymers. *Chem. Phys. Lett.* **1983**, *101*, 149–152.
- (39) Karpfen, A.; Beyer, A. Ab Initio Studies on Polymers. VI. Torsional Potential in Regular Polyethylene Chains. *J. Comput. Chem.* **1984**, *5*, 11–18.
- (40) André, J. M.; Vercauteren, D. P.; Bodart, V. P.; Fripiat, J. G. Ab Initio Calculations of the Electronic Structure of Helical Polymers. *J. Comput. Chem.* **1984**, *5*, 535–547.
- (41) Teramae, H.; Yamabe, T.; Imamura, A. Ab Initio Studies on the Geometrical and Vibrational Structures of Polymers. *J. Chem. Phys.* **1984**, *81*, 3564–3572.
- (42) Springborg, M.; Jones, R. O. Energy Surfaces of Polymeric Sulfur: Structure and Electronic Properties. *Phys. Rev. Lett.* **1986**, *57*, 1145–1148.
- (43) Teramae, H.; Takeda, K. Ab Initio Studies on Silicon Compounds. II. On the Gauche Structure of the Parent Polysilane. *J. Am. Chem. Soc.* **1989**, *111*, 1281–1285.
- (44) Mintmire, J. W. In *Density Functional Methods in Chemistry*; Labanowski, J. K., Andzelm, J. W., Eds.; Springer-Verlag, 1991; pp 125–137.
- (45) Mintmire, J. W.; Dunlap, B. I.; White, C. T. Are Fullerene Tubules Metallic? *Phys. Rev. Lett.* **1992**, *68*, 631–634.
- (46) Mintmire, J. W.; Robertson, D. H.; White, C. T. Properties of Fullerene Nanotubes. *J. Phys. Chem. Solids* **1993**, *54*, 1835–1840.
- (47) Hirata, S.; Iwata, S. Density functional crystal orbital study on the normal vibrations of polyacetylene and polymethineimine. *J. Chem. Phys.* **1997**, *107*, 10075–10084.
- (48) Hirata, S.; Torii, H.; Tasumi, M. Density-functional crystal orbital study on the structures and energetics of polyacetylene isomers. *Phys. Rev. B* **1998**, *57*, 11994–12001.

- (49) Zhang, M. L.; Miao, M. S.; Van Doren, V. E.; Ladik, J. J.; Mintmire, J. W. Calculation of the total energy per unit cell and of the band structures of the five nucleotide base stacks using the local-density approximation. *J. Chem. Phys.* **1999**, *111*, 8696–8700.
- (50) Elizondo, S. L.; Mintmire, J. W. Ab initio study of helical silver single-wall nanotubes and nanowires. *Phys. Rev. B* **2006**, *73*.
- (51) Mintmire, J. W. Density-functional methods for extended helical systems. *Adv. Quantum Chem.* **2022**, *85*, 177–196.
- (52) Hirata, S. Nonvanishing quadrature derivatives in the analytical gradients of density functional energies in crystals and helices. *Mol. Phys.* **2022**, e2086500.
- (53) Jovanovic, M.; Michl, J. Effect of Conformation on Electron Localization and Delocalization in Infinite Helical Chains  $[X(CH_3)_2]_\infty$  ( $X = Si, Ge, Sn, \text{ and } Pb$ ). *J. Am. Chem. Soc.* **2019**, *141*, 13101–13113.
- (54) Bunn, C. W.; Howells, E. R. Structures of Molecules and Crystals of Fluorocarbons. *Nature* **1954**, *174*, 549–551.
- (55) Clark, E. S. The molecular conformations of polytetrafluoroethylene: forms II and IV. *Polymer* **1999**, *40*, 4659–4665.
- (56) D’Amore, M.; Talarico, G.; Barone, V. Periodic and high-temperature disordered conformations of polytetrafluoroethylene chains: An ab initio modeling. *J. Am. Chem. Soc.* **2006**, *128*, 1099–1108.
- (57) Weeks, J. J.; Clark, E. S.; Eby, R. K. Crystal Structure of the Low-Temperature Phase (II) of Polytetrafluoroethylene. *Polymer* **1981**, *22*, 1480–1486.
- (58) Linderberg, J.; Öhrn, Y. Improved Single-Particle Propagators in Theory of Conjugated Systems. *Proc. Roy. Soc. (London)* **1965**, A285, 445.

- (59) Hedin, L. New Method for Calculating one-Particle Green's Function with Application to Electron-Gas Problem. *Phys. Rev.* **1965**, *139*, A796.
- (60) Öhrn, Y.; Linderberg, J. Propagators for Alternant Hydrocarbon Molecules. *Phys. Rev.* **1965**, *139*, A1063.
- (61) Linderberg, J.; Öhrn, Y. Improved decoupling procedure for Green function. *Chem. Phys. Lett.* **1967**, *1*, 295–296.
- (62) Goscinski, O.; Lukman, B. Moment-conserving decoupling of Green functions via Padé approximants. *Chem. Phys. Lett.* **1970**, *7*, 573–576.
- (63) Doll, J. D.; Reinhard, W. P. Many-Body Green's Functions for Finite, Nonuniform Systems: Applications to Closed Shell Atoms. *J. Chem. Phys.* **1972**, *57*, 1169.
- (64) Pickup, B. T.; Goscinski, O. Direct Calculation of Ionization Energies. I. Closed Shells. *Mol. Phys.* **1973**, *26*, 1013–1035.
- (65) Yarlagadda, B. S.; Csanak, G.; Taylor, H. S.; Schneider, B.; Yaris, R. Application of Many-Body Green's Functions to Scattering and Bound-State Properties of Helium. *Phys. Rev. A* **1973**, *7*, 146–154.
- (66) Linderberg, J.; Öhrn, Y. *Propagators in Quantum Chemistry*; Academic Press: London, 1973.
- (67) Tsui, F. S. M.; Freed, K. F. Relationship between One-Electron Green's Function and Quantum Chemical Theories. *Chem. Phys.* **1974**, *5*, 337–349.
- (68) Paldus, J.; Čížek, J. Time-Independent Diagrammatic Approach to Perturbation Theory of Fermion Systems. *Adv. Quantum Chem.* **1975**, *9*, 105–197.
- (69) Cederbaum, L. S. One-Body Green's Function for Atoms and Molecules: Theory and Application. *J. Phys. B: At. Mol. Phys.* **1975**, *8*, 290–303.

- (70) Cederbaum, L. S.; Domcke, W. Theoretical Aspects of Ionization Potentials and Photoelectron Spectroscopy: A Green's Function Approach. *Adv. Chem. Phys.* **1977**, *36*, 205–344.
- (71) Simons, J. Theoretical Studies of Negative Molecular Ions. *Annu. Rev. Phys. Chem.* **1977**, *28*, 15–45.
- (72) Herman, M. F.; Yeager, D. L.; Freed, K. F. Analysis of Third Order Contributions to Equations of Motion Green's Function Ionization Potentials: Application to  $N_2$ . *Chem. Phys.* **1978**, *29*, 77–96.
- (73) Baker, J.; Pickup, B. T. A Method for Molecular Ionization Potentials. *Chem. Phys. Lett.* **1980**, *76*, 537–541.
- (74) Öhrn, Y.; Born, G. Molecular Electron Propagator Theory and Calculations. *Adv. Quantum Chem.* **1981**, *13*, 1–88.
- (75) Jørgensen, P.; Simons, J. *Second Quantization-Based Methods in Quantum Chemistry*; Academic Press: New York, 1981.
- (76) Schirmer, J. Beyond the Random-Phase Approximation: A New Approximation Scheme for the Polarization Propagator. *Phys. Rev. A* **1982**, *26*, 2395–2416.
- (77) Schirmer, J.; Cederbaum, L. S.; Walter, O. New Approach to the One-Particle Green's-Function for Finite Fermi Systems. *Phys. Rev. A* **1983**, *28*, 1237–1259.
- (78) von Niessen, W.; Schirmer, J.; Cederbaum, L. S. *Comput. Phys. Reports* **1984**, *1*, 57–125.
- (79) Prasad, M. D.; Pal, S.; Mukherjee, D. Some Aspects of Self-Consistent Propagator Theories. *Phys. Rev. A* **1985**, *31*, 1287–1298.
- (80) Hybertsen, M. S.; Louie, S. G. Electron Correlation in Semiconductors and Insulators: Band-Gaps and Quasi-Particle Energies. *Phys. Rev. B* **1986**, *34*, 5390–5413.
- (81) Oddershede, J. Propagator methods. *Adv. Chem. Phys.* **1987**, *69*, 201–239.

- (82) Kutzelnigg, W.; Mukherjee, D. Normal order and extended Wick theorem for a multiconfiguration reference wave function. *J. Chem. Phys.* **1997**, *107*, 432–449.
- (83) Aryasetiawan, F.; Gunnarsson, O. The GW method. *Rep. Prog. Phys.* **1998**, *61*, 237–312.
- (84) Ortiz, J. V. Toward an exact one-electron picture of chemical bonding. *Adv. Quantum Chem.* **1999**, *35*, 33–52.
- (85) Onida, G.; Reining, L.; Rubio, A. Electronic excitations: density-functional versus many-body Green’s-function approaches. *Rev. Mod. Phys.* **2002**, *74*, 601–659.
- (86) Ortiz, J. V. Electron propagator theory: An approach to prediction and interpretation in quantum chemistry. *WIREs Comput. Mol. Sci.* **2013**, *3*, 123–142.
- (87) Szabo, A.; Ostlund, N. S. *Modern Quantum Chemistry*; MacMillan: New York, NY, 1982.
- (88) Hirata, S.; Doran, A. E.; Knowles, P. J.; Ortiz, J. V. One-particle many-body Green’s function theory: Algebraic recursive definitions, linked-diagram theorem, irreducible-diagram theorem, and general-order algorithms. *J. Chem. Phys.* **2017**, *147*, 044108.
- (89) Bower, D. I.; Maddams, W. F. *The Vibrational Spectroscopy of Polymers*; Cambridge University Press: Cambridge, 1989.
- (90) Hauser, K.; He, Y. Q.; Garcia-Diaz, M.; Simmerling, C.; Coutsiyas, E. Characterization of Biomolecular Helices and Their Complementarity Using Geometric Analysis. *J. Chem. Inf. Model.* **2017**, *57*, 864–874.
- (91) Kittel, C. *Quantum Theory of Solids*, 2nd ed.; Wiley: Hoboken, 1963.
- (92) Delhalle, J.; Piela, L.; Brédas, J. L.; André, J.-M. Multipole Expansion in Tight-Binding Hartree–Fock Calculations for Infinite-Model Polymers. *Phys. Rev. B* **1980**, *22*, 6254–6267.
- (93) Obara, S.; Saika, A. Efficient recursive computation of molecular integrals over Cartesian Gaussian functions. *J. Chem. Phys.* **1986**, *84*, 3963.

- (94) Ortiz, J. V. Dyson-orbital concepts for description of electrons in molecules. *J. Chem. Phys.* **2020**, *153*, 070902.
- (95) Hirata, S.; Bartlett, R. J. Many-body Green's-function calculations on the electronic excited states of extended systems. *J. Chem. Phys.* **2000**, *112*, 7339–7344.
- (96) Suhai, S. Quasiparticle Energy-Band Structures in Semiconducting Polymers: Correlation-Effects on the Band-Gap in Polyacetylene. *Phys. Rev. B* **1983**, *27*, 3506–3518.
- (97) Sun, J. Q.; Bartlett, R. J. Second-order many-body perturbation-theory calculations in extended systems. *J. Chem. Phys.* **1996**, *104*, 8553–8565.
- (98) Sun, J.-Q.; Bartlett, R. J. Correlated prediction of the photoelectron spectrum of polyethylene: Explanation of XPS and UPS measurements. *Phys. Rev. Lett.* **1996**, *77*, 3669–3672.
- (99) Hirata, S.; Hermes, M. R.; Simons, J.; Ortiz, J. V. General-Order Many-Body Green's Function Method. *J. Chem. Theory Comput.* **2015**, *11*, 1595–1606.
- (100) Kunz, A. B. Electronic Polarons in Nonmetals. *Phys. Rev. B* **1972**, *6*, 606–615.
- (101) Liegener, C.-M. *Ab initio* Calculations of Correlation Effects in *Trans*-Polyacetylene. *J. Chem. Phys.* **1988**, *88*, 6999–7004.
- (102) Suhai, S. Bond Alternation in Infinite Polyene: Peierls Distortion Reduced by Electron Correlation. *Chem. Phys. Lett.* **1983**, *96*, 619–625.
- (103) Ye, Y. J.; Förner, W.; Ladik, J. Numerical Application of the Coupled-Cluster Theory with Localized Orbitals to Polymers. I. Total Correlation Energy Per Unit Cell. *Chem. Phys.* **1993**, *178*, 1–23.
- (104) Suhai, S. Cooperative Effects in Hydrogen Bonding: Fourth-Order Many-Body Perturbation Theory Studies of Water Oligomers and of an Infinite Water Chain as a Model for Ice. *J. Chem. Phys.* **1994**, *101*, 9766–9782.



- (105) Suhai, S. Electron Correlation in Extended Systems: Fourth-Order Many-Body Perturbation Theory and Density-Functional Methods Applied to an Infinite Chain of Hydrogen Atoms. *Phys. Rev. B* **1994**, *50*, 14791–14801.
- (106) Suhai, S. Electron Correlation and Dimerization in *trans*-polyacetylene: Many-Body Perturbation Theory Versus Density-Functional Methods. *Phys. Rev. B* **1995**, *51*, 16553–16567.
- (107) Hirata, S.; Iwata, S. Analytical energy gradients in second-order Møller–Plesset perturbation theory for extended systems. *J. Chem. Phys.* **1998**, *109*, 4147–4155.
- (108) Ayala, P. Y.; Kudin, K. N.; Scuseria, G. E. Atomic orbital Laplace-transformed second-order Møller–Plesset theory for periodic systems. *J. Chem. Phys.* **2001**, *115*, 9698–9707.
- (109) Hirata, S.; Podeszwa, R.; Tobita, M.; Bartlett, R. J. Coupled-cluster singles and doubles for extended systems. *J. Chem. Phys.* **2004**, *120*, 2581–2592.
- (110) Shimazaki, T.; Hirata, S. On the Brillouin-Zone Integrations in Second-Order Many-Body Perturbation Calculations for Extended Systems of One-Dimensional Periodicity. *Int. J. Quantum Chem.* **2009**, *109*, 2953–2959.
- (111) Hirata, S.; Shimazaki, T. Fast second-order many-body perturbation method for extended systems. *Phys. Rev. B* **2009**, *80*, 085118.
- (112) Ohnishi, Y. Y.; Hirata, S. Logarithm second-order many-body perturbation method for extended systems. *J. Chem. Phys.* **2010**, *133*, 034106.
- (113) Pireaux, J. J.; Svensson, S.; Basilier, E.; Malmqvist, P.-Å.; Gelius, U.; Gaudano, R.; Siegbahn, K. Core-Electron Relaxation Energies and Valence-Band Formation of Linear Alkanes Studied in Gas-Phase by Means of Electron Spectroscopy. *Phys. Rev. A* **1976**, *14*, 2133–2145.

- (114) Ueno, N.; Seki, K.; Sato, N.; Fujimoto, H.; Kuramochi, T.; Sugita, K.; Inokuchi, H. Energy-Band Dispersion in Oriented Thin-Films of Pentatriacontan-18-One by Angle-Resolved Photoemission with Synchrotron Radiation. *Phys. Rev. B* **1990**, *41*, 1176–1183.
- (115) Shearer, H. M. M.; Vand, V. The Crystal Structure of the Monoclinic Form of Normal-Hexatriacontane. *Acta Crystallogr.* **1956**, *9*, 379–384.
- (116) Krimm, S.; Liang, C. Y.; Sutherland, G. B. B. M. Infrared Spectra of High Polymers. II. Polyethylene. *J. Chem. Phys.* **1956**, *25*, 549–562.
- (117) Nielsen, J. R.; Woollett, A. H. Vibrational Spectra of Polyethylenes and Related Substances. *J. Chem. Phys.* **1957**, *26*, 1391–1400.
- (118) Nielsen, J. R.; Holland, R. F. Dichroism and interpretation of the infrared bands of oriented crystalline polyethylene. *J. Mol. Spectrosc.* **1961**, *6*, 394–418.
- (119) Brown, R. G. Raman Spectra of Polyethylenes. *J. Chem. Phys.* **1963**, *38*, 221.
- (120) Snyder, R. G.; Schachtschneider, J. H. Vibrational Analysis of the *n*-Paraffins. I. Assignments of Infrared Bands in the Spectra of C<sub>3</sub>H<sub>8</sub> through *n*-C<sub>19</sub>H<sub>40</sub>. *Spectrochim. Acta* **1963**, *19*, 85–116.
- (121) Parker, S. F. Inelastic neutron scattering spectra of polyethylene. *J. Chem. Soc., Faraday Trans.* **1996**, *92*, 1941–1946.
- (122) Hirata, S.; Iwata, S. Density functional crystal orbital study on the normal vibrations and phonon dispersion curves of all-*trans* polyethylene. *J. Chem. Phys.* **1998**, *108*, 7901–7908.
- (123) Becke, A. D. Density-Functional Thermochemistry. III. The Role of Exact Exchange. *J. Chem. Phys.* **1993**, *98*, 5648–5652.
- (124) Vosko, S. H.; Wilk, L.; Nusair, M. Accurate Spin-Dependent Electron Liquid Correlation Energies for Local Spin-Density Calculations: A Critical Analysis. *Can. J. Phys.* **1980**, *58*, 1200–1211.

- (125) Hirata, S. POLYMER 3.0. 2022.
- (126) The vibrational frequencies at the phase angle  $\theta = 0$  of  $(\text{NH})_x$  and  $(\text{O})_x$  were obtained by the crystal-orbital method with POLYMER<sup>125</sup> using a large unit cell of 13 NH or 13 O groups and also by the supercell method of 19 NH or 19 O groups with NWChem.<sup>127</sup> They agree with each other within  $6 \text{ cm}^{-1}$  except for the lowest optical mode whose frequencies agree within  $26 \text{ cm}^{-1}$ . Since phonons at  $\theta \neq 0$  destroy periodic symmetry, the intrinsic efficiency of the crystal-orbital method is lost. Hence, we elected to use the supercell method and molecular software for the normal-mode analysis.
- (127) Aprà, E. et al. NWChem: Past, present, and future. *J. Chem. Phys.* **2020**, *152*, 184102.
- (128) Piseri, L.; Powell, B. M.; Dolling, G. Lattice dynamics of Polytetrafluoroethylene. *J. Chem. Phys.* **1973**, *58*, 158–171.
- (129) Marshall, W.; Lovesey, S. W. *Theory of Thermal Neutron Scattering*; Oxford University Press: London, 1971.
- (130) Teare, P. W. The Crystal Structure of Orthorhombic Hexatriacontane  $\text{C}_{36}\text{H}_{74}$ . *Acta Crystallogr.* **1959**, *12*, 294–300.
- (131) Herzberg, G. *Electronic Spectra and Electronic Structure of Polyatomic Molecules*; Van Nostrand: New York, 1966.
- (132) Qin, X. Y.; Hirata, S. Anharmonic Phonon Dispersion in Polyethylene. *J. Phys. Chem. B* **2020**, *124*, 10477–10485.
- (133) Rajendran, A.; Tsuchiya, T.; Hirata, S.; Iordanov, T. D. Predicting Properties of Organic Optoelectronic Materials: Asymptotically Corrected Density Functional Study. *J. Phys. Chem. A* **2012**, *116*, 12153–12162.
- (134) Fujihira, M.; Inokuchi, H. Photoemission from Polyethylene. *Chem. Phys. Lett.* **1972**, *17*, 554–556.

- (135) Seki, K.; Tanaka, H.; Ohta, T.; Aoki, Y.; Imamura, A.; Fujimoto, H.; Yamamoto, H.; Inokuchi, H. Electronic Structure of Poly(Tetrafluoroethylene) Studied by UPS, VUV Absorption, and Band Calculations. *Phys. Scr.* **1990**, *41*, 167–171.
- (136) Shirakawa, H.; Ikeda, S. Infrared Spectra of Poly(Acetylene). *Polymer J.* **1971**, *2*, 231.
- (137) Shirakawa, H.; Ito, T.; Ikeda, S. Raman Scattering and Electronic Spectra of Poly(Acetylene). *Polym. J.* **1973**, *4*, 460–462.
- (138) Chiang, C. K.; Fincher, C. R.; Park, Y. W.; Heeger, A. J.; Shirakawa, H.; Louis, E. J.; Gau, S. C.; MacDiarmid, A. G. Electrical Conductivity in Doped Polyacetylene. *Phys. Rev. Lett.* **1977**, *39*, 1098–1101.
- (139) Chien, J. C. W. *Polyacetylene: Chemistry, Physics, and Material Science*; Academic: Orlando, 1984.
- (140) Heeger, A. J.; Kivelson, S.; Schrieffer, J. R.; Su, W. P. Solitons in Conducting Polymers. *Rev. Mod. Phys.* **1988**, *60*, 781–850.
- (141) Yoshida, H.; Tasumi, M. Infrared and Raman Spectra of *Trans,Trans*-1,3,5,7-Octatetraene and Normal-Coordinate Analysis Based on *Ab initio* Molecular Orbital Calculations. *J. Chem. Phys.* **1988**, *89*, 2803–2809.
- (142) Hirata, S.; Yoshida, H.; Torii, H.; Tasumi, M. Vibrational Analyses of *Trans,Trans*-1,3,5,7-Octatetraene and All-*Trans*-1,3,5,7,9-Decapentaene Based on *Ab Initio* Molecular Orbital Calculations and Observed Infrared and Raman Spectra. *J. Chem. Phys.* **1995**, *103*, 8955–8963.
- (143) Hirata, S.; Torii, H.; Tasumi, M. Stereostructural and vibrational analyses of cis-polyacetylene based on density functional calculations of oligoenes. *Bull. Chem. Soc. Jpn.* **1996**, *69*, 3089–3106.

- (144) Lieser, G.; Wegner, G.; Müller, W.; Enkelmann, V.; Meyer, W. H. The Structure and Morphology of *Trans*-Poly(Acetylene). *Makromol. Chem. Rapid Commun.* **1980**, *1*, 627–632.
- (145) Shimamura, K.; Karasz, F. E.; Hirsch, J. A.; Chien, J. C. W. Crystal Structure of *Trans*-Polyacetylene. *Makromol. Chem. Rapid Commun.* **1981**, *2*, 473–480.
- (146) Fincher, C. R.; Chen, C. E.; Heeger, A. J.; Macdiarmid, A. G.; Hastings, J. B. Structural Determination of the Symmetry-Breaking Parameter in *Trans*-(CH)<sub>x</sub>. *Phys. Rev. Lett.* **1982**, *48*, 100–104.
- (147) Baughman, R. H.; Hsu, S. L.; Pez, G. P.; Signorelli, A. J. Structures of *Cis*-Polyacetylene and Highly Conducting Derivatives. *J. Chem. Phys.* **1978**, *68*, 5405–5409.
- (148) Lieser, G.; Wegner, G.; Müller, W.; Enkelmann, V. On the Morphology and Structure of *Cis*-Poly(Acetylene). *Makromol. Chem. Rapid Commun.* **1980**, *1*, 621–626.
- (149) Chien, J. C. W.; Karasz, F. E.; Shimamura, K. Electron-Diffraction Study of Pristine and iodine-Doped and Iodine-Doped Poly(*Cis*-Acetylene). *J. Polym. Sci. Polym. Lett. Ed.* **1982**, *20*, 97–102.
- (150) Chien, J. C. W.; Karasz, F. E.; Shimamura, K. Crystal Structure of Pristine and Iodine-Doped *Cis*-Polyacetylene. *Macromolecules* **1982**, *15*, 1012–1017.
- (151) Kuzmany, H. Resonance Raman Scattering from Neutral and Doped Polyacetylene. *Phys. Status Solidi B* **1980**, *97*, 521–531.
- (152) Yannoni, C. S.; Clarke, T. C. Molecular Geometry of *Cis*-Polyacetylene and *Trans*-Polyacetylene by Nutation NMR Spectroscopy. *Phys. Rev. Lett.* **1983**, *51*, 1191–1193.
- (153) Takeuchi, H.; Arakawa, T.; Furukawa, Y.; Harada, I.; Shirakawa, H. Density of Vibrational States in *Trans*-Polyene: Comparison with the Infrared, Raman and Neutron Spectra of *Trans*-polyacetylene. *J. Mol. Struct.* **1987**, *158*, 179–193.

- (154) Kamiya, K.; Miyamae, T.; Oku, M.; Seki, K.; Inokuchi, H.; Tanaka, C.; Tanaka, J. Ultraviolet photoemission spectra of perchlorate-doped *cis*- and *trans*-polyacetylene. *J. Phys. Chem.* **1996**, *100*, 16213–16217.
- (155) Hirata, S.; Torii, H.; Furukawa, Y.; Tasumi, M.; Tomkinson, J. Inelastic neutron scattering from *trans*-polyacetylene. *Chem. Phys. Lett.* **1996**, *261*, 241–245.
- (156) Falk, J. E.; Fleming, R. J. Study of Electronic Band Structure of Polyacetylene and Polyfluoroethylenes. *J. Phys. C: Solid State Phys.* **1975**, *8*, 627–646.
- (157) Grant, P. M.; Batra, I. P. Band Structure of Polyacetylene,  $(\text{CH})_x$ . *Solid State Commun.* **1979**, *29*, 225–229.
- (158) Kasowski, R. V.; Hsu, W. Y.; Caruthers, E. B. Electronic Properties of Polyacetylene, Polyethylene, and Polytetrafluoroethylene. *J. Chem. Phys.* **1980**, *72*, 4896–4900.
- (159) Mintmire, J. W.; White, C. T. Theoretical Treatment of the Dielectric Response of All-*Trans*-Polyacetylene. *Phys. Rev. B* **1983**, *27*, 1447–1449.
- (160) Springborg, M. Self-Consistent Electronic Structures of Polyacetylene. *Phys. Rev. B* **1986**, *33*, 8475–8489.
- (161) Mintmire, J. W.; White, C. T. Local-Density-Functional Results for the Dimerization of *Trans*-polyacetylene: Relationship to the Band Gap Problem. *Phys. Rev. B* **1987**, *35*, 4180–4183.
- (162) von Boehm, J.; Kuivalainen, P.; Calais, J.-L. Self-Consistent Linear-Combination-of-Gaussian-Orbitals Approach for Polymers: Application to *Trans*-( $\text{CH})_x$ . *Phys. Rev. B* **1987**, *35*, 8177–8183.
- (163) Vogl, P.; Campbell, D. K. Three-Dimensional Structure and Intrinsic Defects in *Trans*-Polyacetylene. *Phys. Rev. Lett.* **1989**, *62*, 2012–2015.

- (164) Ashkenazi, J.; Pickett, W. E.; Krakauer, H.; Wang, C. S.; Klein, B. M.; Chubb, S. R. Ground State of *Trans*-Polyacetylene and the Peierls Mechanism. *Phys. Rev. Lett.* **1989**, *62*, 2016–2019.
- (165) Springborg, M.; Calais, J.-L.; Goscinski, O.; Eriksson, L. A. Linear-Muffin-Tin-Orbital Method for Helical Polymers: A Detailed Study of *Trans*-polyacetylene. *Phys. Rev. B* **1991**, *44*, 12713–12736.
- (166) Paloheimo, J.; von Boehm, J. Density-Functional Study of the Dimerization of *Trans*-polyacetylene. *Phys. Rev. B* **1992**, *46*, 4304–4307.
- (167) Hirata, S.; Torii, H.; Tasumi, M. Vibrational Analyses of *Trans*-polyacetylene Based on *Ab Initio* Second-Order Møller–Plesset Perturbation Calculations of *Trans*-Oligoenes. *J. Chem. Phys.* **1995**, *103*, 8964–8979.
- (168) Kuchitsu, K. *Structure Data of Free Polyatomic Molecules: Basic Data*; Springer: Berlin, 1998.
- (169) Aulbur, W. G.; Jonsson, L.; Wilkins, J. W. Quasiparticle calculations in solids. *Solid State Phys.* **2000**, *54*, 1–218.
- (170) Nakafuku, C.; Takemura, T. Crystal Structure of High Pressure Phase of Polytetrafluoroethylene. *Jpn. J. Appl. Phys.* **1975**, *14*, 599–602.
- (171) Lorenzen, M.; Hanfland, M.; Mermet, A. Poly(tetrafluoroethylene) under pressure: X-diffraction studies. *Nucl. Instr. Meth. Phys. Res. B* **2003**, *200*, 416–420.
- (172) Farmer, B. L.; Eby, R. K. Energy Calculations of the Crystal Structure of the Low-Temperature Phase (II) of Polytetrafluoroethylene. *Polymer* **1981**, *22*, 1487–1495.
- (173) D’Amore, M.; Auriemma, F.; De Rosa, C.; Barone, V. Disordered chain conformations of poly(tetrafluoroethylene) in the high-temperature crystalline form I. *Macromolecules* **2004**, *37*, 9473–9480.

- (174) Fatti, G.; Righi, M. C.; Dini, D.; Ciniero, A. First-Principles Insights into the Structural and Electronic Properties of Polytetrafluoroethylene in Its High-Pressure Phase (Form III). *J. Phys. Chem. C* **2019**, *123*, 6250–6255.
- (175) Grainger, D. W.; Stewart, C. W. *Fluorinated Surfaces, Coatings, and Films*; American Chemical Society, 2001; Vol. 787; pp 1–14.
- (176) Hellwege, K. H.; Hellwege, A. M. *Landolt-Bornstein: Group II: Atomic and Molecular Physics Volume 7: Structure Data of Free Polyatomic Molecules*; Springer-Verlag: Berlin, 1976.
- (177) Clark, D. T.; Kilcast, D. Study of Core and Valence Energy Levels of PTFE. *Nature Phys. Sci.* **1971**, *233*, 77–79.
- (178) Pireaux, J. J.; Riga, J.; Caudano, R.; Verbist, J. J.; André, J. M.; Delhalle, J.; Delhalle, S. Electronic Structure of Fluoropolymers: Theory and ESCA Measurements. *J. Electron Spectrosc. Relat. Phenom.* **1974**, *5*, 531–550.
- (179) Delhalle, J.; Delhalle, S.; André, J. M.; Pireaux, J. J.; Riga, J.; Caudano, R.; Verbist, J. J. Electronic Structure of Linear Fluoropolymers: Theory and ESCA Measurements Revisited. *J. Electron Spectrosc. Relat. Phenom.* **1977**, *12*, 293–303.
- (180) Seki, K.; Tanaka, H.; Ohta, T.; Aoki, Y.; Imamura, A.; Fujimoto, H.; Yamamoto, H.; Inokuchi, H. Electronic Structure of Poly(Tetrafluoroethylene) Studied by UPS, VUV Absorption, and Band Calculations. *Phys. Scr.* **1990**, *41*, 167–171.
- (181) Miyamae, T.; Hasegawa, S.; Yoshimura, D.; Ishii, H.; Ueno, N.; Seki, K. Intramolecular energy-band dispersion in oriented thin films of  $n\text{-CF}_3(\text{CF}_2)_{22}\text{CF}_3$  observed by angle-resolved photoemission with synchrotron radiation. *J. Chem. Phys.* **2000**, *112*, 3333–3338.
- (182) Ono, M.; Yamane, H.; Fukagawa, H.; Kera, S.; Yoshimura, D.; Okudaira, K. K.; Morikawa, E.; Seki, K.; Ueno, N. UPS study of VUV-photodegradation of polytetraflu-



- oroethylene (PTFE) ultrathin film by using synchrotron radiation. *Nucl. Inst. Meth. Phys. Res. B* **2005**, 236, 377–382.
- (183) Wang, C.; Duscher, G.; Paddison, S. J. Electron energy loss spectroscopy of polytetrafluoroethylene: Experiment and first principles calculations. *Microscopy* **2014**, 63, 73–83.
- (184) Yoshimura, D.; Ishii, H.; Ouchi, Y.; Miyamae, T.; Hasegawa, S.; Okudaira, K. K.; Ueno, N.; Seki, K. Simulation study of angle-resolved photoemission spectra and intramolecular energy-band dispersion of a poly(tetrafluoroethylene) oligomer film. *J. Chem. Phys.* **2004**, 120, 10753–10762.
- (185) Morokuma, K. Electronic Structures of Linear Polymers. II. Formulation and CNDO/2 Calculation for Polyethylene and Poly(Tetrafluoroethylene). *J. Chem. Phys.* **1971**, 54, 962–971.
- (186) McCubbin, W. L. Assessment of Polymer Band Structure Calculations. *Chem. Phys. Lett.* **1971**, 8, 507–512.
- (187) Delhalle, J. Influence of Chemical Substitution on Energy Band Structure of Polyfluoroethylenes. *Chem. Phys.* **1974**, 5, 306–314.
- (188) Otto, P.; Ladik, J.; Förner, W. The Energy Band Structure of Polyfluoroethylene: Influence of Chemical Substitution and Conformation. *Chem. Phys.* **1985**, 95, 365–372.
- (189) Springborg, M.; Lev, M. Electronic Structures of Polyethylene and Polytetrafluoroethylene. *Phys. Rev. B* **1989**, 40, 3333–3339.
- (190) Cain, S. R.; Matienzo, L. J. Charge Iterated Parameters for Extended Hückel Calculations on Polytetrafluoroethylene: Relevance to X-Ray Photoelectron Spectroscopy. *J. Electron Spectrosc. Relat. Phenom.* **1992**, 58, 365–373.
- (191) Higgs, P. W. The Vibration Spectra of Helical Molecules: Infra-Red and Raman Selection Rules, Intensities and Approximate Frequencies. *Proc. R. Soc. A* **1953**, 220, 472–485.

- (192) Liang, C. Y.; Krimm, S. Infrared Spectra of High Polymers. III. Polytetrafluoroethylene and Polychlorotrifluoroethylene. *J. Chem. Phys.* **1956**, *25*, 563–571.
- (193) Koenig, J. L.; Boerio, F. J. Raman Scattering and Band Assignments in Polytetrafluoroethylene. *J. Chem. Phys.* **1969**, *50*, 2823–2829.
- (194) Peacock, C. J.; Hendra, P. J.; Willis, H. A.; Cudby, M. E. A. Raman Spectrum and Vibrational Assignment for Poly(Tetrafluoro-Ethylene). *J. Chem. Soc. A* **1970**, *1970*, 2943–2947.
- (195) Twisleton, J. F.; White, J. W. Interchain Force Field and Elastic-Constants of Polytetrafluoroethylene. *Polymer* **1972**, *13*, 40–42.
- (196) LaGarde, V.; Prask, H.; Trevino, S. Vibrations in Teflon. *Discuss. Faraday Soc.* **1969**, *48*, 15–18.
- (197) Hannon, M. J.; Boerio, F. J.; Koenig, J. L. Vibrational analysis of polytetrafluoroethylene. *J. Chem. Phys.* **1969**, *50*, 2829–2836.
- (198) Eremets, M. I.; Gavriluk, A. G.; Serebryanaya, N. R.; Trojan, I. A.; Dzivenko, D. A.; Boehler, R.; Mao, H. K.; Hemley, R. J. Structural transformation of molecular nitrogen to a single-bonded atomic state at high pressures. *J. Chem. Phys.* **2004**, *121*, 11296–11300.
- (199) Ma, Y. M.; Oganov, A. R.; Li, Z. W.; Xie, Y.; Kotakoski, J. Novel High Pressure Structures of Polymeric Nitrogen. *Phys. Rev. Lett.* **2009**, *102*, 065501.
- (200) Pickard, C. J.; Needs, R. J. High-Pressure Phases of Nitrogen. *Phys. Rev. Lett.* **2009**, *102*, 125702.
- (201) Christe, K. O.; Wilson, W. W.; Sheehy, J. A.; Boatz, J. A.  $N_5^+$ : A novel homoleptic polynitrogen ion as a high energy density material. *Angew. Chem. Int. Ed.* **1999**, *38*, 2004–2009.
- (202) Vij, A.; Wilson, W. W.; Vij, V.; Tham, F. S.; Sheehy, J. A.; Christe, K. O. Polynitrogen chemistry: Synthesis, characterization, and crystal structure of surprisingly stable fluoroantimonate salts of  $N_5^+$ . *J. Am. Chem. Soc.* **2001**, *123*, 6308–6313.

- (203) Cacace, F.; de Petris, G.; Troiani, A. Experimental detection of tetranitrogen. *Science* **2002**, 295, 480–481.
- (204) Vij, A.; Pavlovich, J. G.; Wilson, W. W.; Vij, V.; Christe, K. O. Experimental detection of the pentaazacyclopentadienide (pentazolate) anion, *cyclo-N<sub>5</sub><sup>-</sup>*. *Angew. Chem. Int. Ed.* **2002**, 41, 3051–3054.
- (205) Bi, Y. F.; Liao, W. P.; Xu, G. C.; Deng, R. P.; Wang, M. Y.; Wu, Z. J.; Gao, S.; Zhang, H. J. Three *p*-*tert*-Butylthiacalix[4]arene-Supported Cobalt Compounds Obtained in One Pot Involving In Situ Formation of N<sub>6</sub>H<sub>2</sub> Ligand. *Inorg. Chem.* **2010**, 49, 7735–7740.
- (206) Li, Y. C.; Qi, C.; Li, S. H.; Zhang, H. J.; Sun, C. H.; Yu, Y. Z.; Pang, S. P. 1,1'-Azobis-1,2,3-triazole: A High-Nitrogen Compound with Stable N<sub>8</sub> Structure and Photochromism. *J. Am. Chem. Soc.* **2010**, 132, 12172–12173.
- (207) Tang, Y. X.; Yang, H. W.; Shen, J. H.; Wu, B.; Ju, X. H.; Lu, C. X.; Cheng, G. B. Synthesis and characterization of 1,1'-azobis(5-methyltetrazole). *New J. Chem.* **2012**, 36, 2447–2450.
- (208) Tang, Y. X.; Yang, H. W.; Wu, B.; Ju, X. H.; Lu, C. X.; Cheng, G. B. Synthesis and Characterization of a Stable, Catenated N<sub>11</sub> Energetic Salt. *Angew. Chem. Int. Ed.* **2013**, 52, 4875–4877.
- (209) Bazanov, B.; Geiger, U.; Carmieli, R.; Grinstein, D.; Welner, S.; Haas, Y. Detection of Cyclo-N<sub>5</sub><sup>-</sup> in THF Solution. *Angew. Chem. Int. Ed.* **2016**, 55, 13233–13235.
- (210) Zhang, C.; Sun, C. G.; Hu, B. C.; Yu, C. M.; Lu, M. Synthesis and characterization of the pentazolate anion *cyclo-N<sub>5</sub><sup>-</sup>* in (N<sub>5</sub>)<sub>6</sub>(H<sub>3</sub>O)<sub>3</sub>(NH<sub>4</sub>)<sub>4</sub>Cl. *Science* **2017**, 355, 374–376.
- (211) Zhang, W.; Wang, K.; Li, J.; Lin, Z.; Song, S.; Huang, S.; Liu, Y.; Nie, F.; Zhang, Q. Stabilization of the Pentazolate Anion in a Zeolitic Architecture with Na<sub>20</sub>N<sub>60</sub> and Na<sub>24</sub>N<sub>60</sub> Nanocages. *Angew. Chem. Int. Ed.* **2018**, 57, 2592–2595.

- (212) Huang, R. Y.; Zhang, C.; Yan, D.; Xiong, Z.; Xu, H.; Ren, X. M. Pb<sup>II</sup>-catalyzed transformation of aromatic nitriles to heptanitrogen anions *via* sodium azide: A combined experimental and theoretical study. *RSC Adv.* **2018**, *8*, 39929–39936.
- (213) Lauderdale, W. J.; Stanton, J. F.; Bartlett, R. J. Stability and Energetics of Metastable Molecules: Tetraazatetrahedrane (N<sub>4</sub>), Hexaazabenzene (N<sub>6</sub>), and Octaazacubane (N<sub>8</sub>). *J. Phys. Chem.* **1992**, *96*, 1173–1178.
- (214) Nguyen, M. T.; Ha, T. K. Azidopentazole is probably the lowest-energy N<sub>8</sub> species: A theoretical study. *Chem. Ber.* **1996**, *129*, 1157–1159.
- (215) Nguyen, M. T. Polynitrogen compounds. I. Structure and stability of N<sub>4</sub> and N<sub>5</sub> systems. *Coord. Chem. Rev.* **2003**, *244*, 93–113.
- (216) Nguyen, M. T.; Ha, T. K. Decomposition mechanism of the polynitrogen N<sub>5</sub> and N<sub>6</sub> clusters and their ions. *Chem. Phys. Lett.* **2001**, *335*, 311–320.
- (217) Huber, H. Is Hexazine Stable. *Angew. Chem. Int. Ed.* **1982**, *21*, 64–65.
- (218) Saxe, P.; Schaefer III, H. F. Cyclic *D*<sub>6h</sub> Hexaazabenzene: A Relative Minimum on the N<sub>6</sub> Potential Energy Hypersurface. *J. Am. Chem. Soc.* **1983**, *105*, 1760–1764.
- (219) Glukhovtsev, M. N.; Schleyer, P. v. Structures, Bonding and Energies of N<sub>6</sub> Isomers. *Chem. Phys. Lett.* **1992**, *198*, 547–554.
- (220) Ha, T. K.; Nguyen, M. T. The Identity of the six Nitrogen-Atoms (N<sub>6</sub>) Species. *Chem. Phys. Lett.* **1992**, *195*, 179–183.
- (221) Tobita, M.; Bartlett, R. J. Structure and stability of N<sub>6</sub> isomers and their spectroscopic characteristics. *J. Phys. Chem. A* **2001**, *105*, 4107–4113.
- (222) Wilson, K. J.; Perera, S. A.; Bartlett, R. J.; Watts, J. D. Stabilization of the pseudo-benzene N<sub>6</sub> ring with oxygen. *J. Phys. Chem. A* **2001**, *105*, 7693–7699.

- (223) Greschner, M. J.; Zhang, M.; Majumdar, A.; Liu, H. Y.; Peng, F.; Tse, J. S.; Yao, Y. S. A New Allotrope of Nitrogen as High-Energy Density Material. *J. Phys. Chem. A* **2016**, *120*, 2920–2925.
- (224) Fau, S.; Bartlett, R. J. Possible products of the end-on addition of  $\text{N}_3^-$  to  $\text{N}_5^+$  and their stability. *J. Phys. Chem. A* **2001**, *105*, 4096–4106.
- (225) Hirshberg, B.; Gerber, R. B.; Krylov, A. I. Calculations predict a stable molecular crystal of  $\text{N}_8$ . *Nature Chem.* **2014**, *6*, 52–56.
- (226) Fau, S.; Wilson, K. J.; Bartlett, R. J. On the stability of  $\text{N}_5^+\text{N}_5^-$ . *J. Phys. Chem. A* **2002**, *106*, 4639–4644.
- (227) Olah, G. A.; Prakash, G. K. S.; Rasul, G.  $\text{N}_6^{2+}$  and  $\text{N}_4^{2+}$  dications and their  $\text{N}_{12}$  and  $\text{N}_{10}$  azido derivatives: DFT/GIAO-MP2 theoretical studies. *J. Am. Chem. Soc.* **2001**, *123*, 3308–3310.
- (228) Ha, T. K.; Suleimenov, O.; Nguyen, M. T. A quantum chemical study of three isomers of  $\text{N}_{20}$ . *Chem. Phys. Lett.* **1999**, *315*, 327–334.
- (229) Raghavachari, K.; Trucks, G. W.; Pople, J. A.; Headgordon, M. A Fifth-Order Perturbation Comparison of Electron Correlation Theories. *Chem. Phys. Lett.* **1989**, *157*, 479–483.
- (230) Watts, J. D.; Gauss, J.; Bartlett, R. J. Coupled-Cluster Methods with Noniterative Triple Excitations for Restricted Open-Shell Hartree-Fock and Other General Single Determinant Reference Functions: Energies and Analytical Gradients. *J. Chem. Phys.* **1993**, *98*, 8718–8733.
- (231) Dewar, M. J. S. MO Studies of Some Nonbenzenoid Aromatic Systems. *Pure Appl. Chem.* **1975**, *44*, 767–782.
- (232) Ha, T. K.; Cimiraglia, R.; Nguyen, M. T. Can Hexazine ( $\text{N}_6$ ) Be Stable. *Chem. Phys. Lett.* **1981**, *83*, 317–319.

- (233) Huber, H.; Ha, T. K.; Nguyen, M. T. Is  $N_6$  an Open-Chain Molecule. *J. Mol. Struct. Theochem* **1983**, *105*, 351–358.
- (234) Kim, J. Y.; Furukawa, Y.; Sakamoto, A.; Tasumi, M. Infrared and Raman studies of the radical anion of  $\alpha,\omega$ -diphenyl-1,3,5,7,9-decapentaene as a model compound in polyacetylene. *Synth. Metals* **2002**, *129*, 235–238.
- (235) Tanaka, K.; Koike, T.; Ohzeki, K.; Yoshizawa, K.; Yamabe, T. Photo-Isomerization of *Cis*-Polyacetylene. *Solid State Commun.* **1983**, *47*, 127–129.
- (236) Klapötke, T. M.; Martin, F. A.; Stierstorfer, J.  $C_2N_{14}$ : An Energetic and Highly Sensitive Binary Azidotetrazole. *Angew. Chem. Int. Ed.* **2011**, *50*, 4227–4229.
- (237) Klapötke, T. M.; Krumm, B.; Martin, F. A.; Stierstorfer, J. New Azidotetrazoles: Structurally Interesting and Extremely Sensitive. *Chem. Asian J.* **2012**, *7*, 214–224.
- (238) Banert, K.; Richter, S.; Schaarschmidt, D.; Lang, H. Well Known or New? Synthesis and Structure Assignment of Binary  $C_2N_{14}$  Compounds Reinvestigated. *Angew. Chem. Int. Ed.* **2013**, *52*, 3499–3502.
- (239) Nellis, W. J.; Holmes, N. C.; Mitchell, A. C.; Vanthiel, M. Phase-Transition in Fluid Nitrogen at High-Densities and Temperatures. *Phys. Rev. Lett.* **1984**, *53*, 1661–1664.
- (240) Pohl, A.; Meider, H.; Springborg, M. On the Peierls Distortion and the Local-Density Approximation. *J. Mol. Struct. (Theochem)* **1994**, *111*, 165–173.
- (241) Alemany, M. M. G.; Martins, J. L. Density-functional study of nonmolecular phases of nitrogen: Metastable phase at low pressure. *Phys. Rev. B* **2003**, *68*, 024110.
- (242) Mattson, W. D.; Sanchez-Portal, D.; Chiesa, S.; Martin, R. M. Prediction of new phases of nitrogen at high pressure from first-principles simulations. *Phys. Rev. Lett.* **2004**, *93*, 125501.

- (243) Goncharov, A. F.; Gregoryanz, E.; Mao, H. K.; Liu, Z. X.; Hemley, R. J. Optical evidence for a nonmolecular phase of nitrogen above 150 GPa. *Phys. Rev. Lett.* **2000**, *85*, 1262–1265.
- (244) Eremets, M. L.; Hemley, R. J.; Mao, H.; Gregoryanz, E. Semiconducting non-molecular nitrogen up to 240 GPa and its low-pressure stability. *Nature* **2001**, *411*, 170–174.
- (245) Gregoryanz, E.; Goncharov, A. F.; Hemley, R. J.; Mao, H. K. High-pressure amorphous nitrogen. *Phys. Rev. B* **2001**, *64*, 052103.
- (246) Gregoryanz, E.; Goncharov, A. F.; Hemley, R. J.; Mao, H. K.; Somayazulu, M.; Shen, G. Y. Raman, infrared, and x-ray evidence for new phases of nitrogen at high pressures and temperatures. *Phys. Rev. B* **2002**, *66*, 224108.
- (247) Tomasino, D.; Kim, M.; Smith, J.; Yoo, C. S. Pressure-Induced Symmetry-Lowering Transition in Dense Nitrogen to Layered Polymeric Nitrogen (LP-N) with Colossal Raman Intensity. *Phys. Rev. Lett.* **2014**, *113*, 205502.
- (248) Sontising, W.; Beran, G. J. O. Theoretical assessment of the structure and stability of the  $\lambda$  phase of nitrogen. *Phys. Rev. Mater.* **2019**, *3*, 095002.
- (249) Sontising, W.; Beran, G. J. O. Combining crystal structure prediction and simulated spectroscopy in pursuit of the unknown nitrogen phase  $\zeta$  crystal structure. *Phys. Rev. Mater.* **2020**, *4*, 063601.
- (250) Li, J. F.; Wang, X. L.; Xu, N.; Li, D. Y.; Wang, D. C.; Chen, L. Pressure-induced polymerization of nitrogen in potassium azides. *Epl* **2013**, *104*, 16005.
- (251) Prasad, D. L. V. K.; Ashcroft, N. W.; Hoffmann, R. Evolving Structural Diversity and Metallicity in Compressed Lithium Azide. *J. Phys. Chem. C* **2013**, *117*, 20838–20846.
- (252) Shen, Y. Q.; Oganov, A. R.; Qian, G. R.; Zhang, J.; Dong, H. F.; Zhu, Q.; Zhou, Z. X. Novel lithium-nitrogen compounds at ambient and high pressures. *Sci. Rep.* **2015**, *5*, 14204.

- (253) Peng, F.; Han, Y. X.; Liu, H. Y.; Yao, Y. S. Exotic stable cesium polynitrides at high pressure. *Sci. Rep.* **2015**, *5*, 16902.
- (254) Oganov, A. R.; Glass, C. W. Crystal structure prediction using ab initio evolutionary techniques: Principles and applications. *J. Chem. Phys.* **2006**, *124*, 244704.
- (255) Steele, B. A.; Oleynik, I. I. Novel Potassium Polynitrides at High Pressures. *J. Phys. Chem. A* **2017**, *121*, 8955–8961.
- (256) Williams, A. S.; Steele, B. A.; Oleynik, I. I. Novel rubidium poly-nitrogen materials at high pressure. *J. Chem. Phys.* **2017**, *147*, 234701.
- (257) Bykov, M. et al. Fe–N system at high pressure reveals a compound featuring polymeric nitrogen chains. *Nat. Commun.* **2018**, *9*, 2756.
- (258) Bykov, M. et al. High-Pressure Synthesis of Metal-Inorganic Frameworks with  $\text{Hf}_4\text{N}_{20}\cdot\text{N}_2$ ,  $\text{WN}_8\cdot\text{N}_2$ , and  $\text{Os}_5\text{N}_{28}\cdot 3\text{N}_2$  Polymeric Nitrogen Linkers. *Angew. Chem. Int. Ed.* **2020**, *59*, 10321–10326.
- (259) Bykov, M.; Bykova, E.; Chariton, S.; Prakapenka, V. B.; Batyrev, I. G.; Mahmood, M. F.; Goncharov, A. F. Stabilization of pentazolate anions in the high-pressure compounds  $\text{Na}_2\text{N}_5$  and  $\text{NaN}_5$  and in the sodium pentazolate framework  $\text{NaN}_5\cdot\text{N}_2$ . *Dalton Trans.* **2021**, *50*, 7229–7237.
- (260) Veith, M.; Schlemmer, G. Crystal and Molecular Structure of *Trans*-Tetrazene-(2) ( $\text{N}_4\text{H}_4$ ) at  $-90^\circ\text{C}$ . *Z. Anorg. Allg. Chem.* **1982**, *494*, 7–19.
- (261) Huber, K. P.; Herzberg, G. *Molecular Spectra and Molecular Structure: Constants of Diatomic Molecules*; Van Nostrand Reinhold: New York, 1979.
- (262) Magers, D. H.; Salter, E. A.; Bartlett, R. J.; Salter, C.; Hess, B. A.; Schaad, L. J. Do Stable Isomers of  $\text{N}_3\text{H}_3$  Exist? *J. Am. Chem. Soc.* **1988**, *110*, 3435–3446.



- (263) Förstel, M.; Tsegaw, Y. A.; Maksyutenko, P.; Mebel, A. M.; Sander, W.; Kaiser, R. I. On the Formation of  $\text{N}_3\text{H}_3$  Isomers in Irradiated Ammonia Bearing Ices: Triazene ( $\text{H}_2\text{NNNH}$ ) or Triimide ( $\text{HNHNNH}$ ). *ChemPhysChem* **2016**, *17*, 2726–2735.
- (264) Kim, Y.; Gilje, J. W.; Seff, K. Synthesis and Structures of Two New Hydrides of Nitrogen, Triazane ( $\text{N}_3\text{H}_5$ ) and Cyclotriazane ( $\text{N}_3\text{H}_3$ ): Crystallographic and Mass-Spectrometric Analyses of Vacuum-Dehydrated Partially Decomposed Fully  $\text{Ag}^+$ -Exchanged Zeolite a Treated with Ammonia. *J. Am. Chem. Soc.* **1977**, *99*, 7057–7059.
- (265) Heo, N. H.; Kim, Y.; Kim, J. J.; Seff, K. Surprising Intrazeolitic Chemistry of Silver. *J. Phys. Chem. C* **2016**, *120*, 5277–5287.
- (266) Förstel, M.; Maksyutenko, P.; Jones, B. M.; Sun, B.-J.; Chen, S.-H.; Chang, A. H.-H.; Kaiser, R. I. Detection of the Elusive Triazane Molecule ( $\text{N}_3\text{H}_5$ ) in the Gas Phase. *ChemPhysChem* **2015**, *16*, 3139–3142.
- (267) Richard, R. M.; Ball, D. W. G2, G3, and complete basis set calculations on the thermodynamic properties of triazane. *J. Mol. Model.* **2008**, *14*, 29–37.
- (268) Grinberg Dana, A.; Moore, K. B.; Jasper, A. W.; Green, W. H. Large Intermediates in Hydrazine Decomposition: A Theoretical Study of the  $\text{N}_3\text{H}_5$  and  $\text{N}_4\text{H}_6$  Potential Energy Surfaces. *J. Phys. Chem. A* **2019**, *123*, 4679–4692.
- (269) Wiberg, N.; Bayer, H.; Bachhuber, H. Isolation of Tetrazene,  $\text{N}_4\text{H}_4$ . *Angew. Chem. Int. Ed.* **1975**, *14*, 177–178.
- (270) Ritter, G.; Häfelfinger, G.; Lüddecke, E.; Rau, H. Tetrazetidine: *Ab initio* Calculations and Experimental Approach. *J. Am. Chem. Soc.* **1989**, *111*, 4627–4635.
- (271) Ball, D. W. Tetrazane: Hartree–Fock, Gaussian-2 and-3, and complete basis set predictions of some thermochemical properties of  $\text{N}_4\text{H}_6$ . *J. Phys. Chem. A* **2001**, *105*, 465–470.

- (272) Ball, D. W. High-level ab initio calculations on hydrogen-nitrogen compounds. Thermochemistry of tetrazetidine,  $N_4H_4$ . *J. Mol. Struct. Theochem* **2002**, *619*, 37–43.
- (273) Fujii, T.; Selvin, C. P.; Sablier, M.; Iwase, K. Analysis of hydronitrogen species generated by a microwave discharge in  $(N_2H_4)/He$ . *J. Phys. Chem. A* **2002**, *106*, 3102–3105.
- (274) Förstel, M.; Maksyutenko, P.; Jones, B. M.; Sun, B. J.; Lee, H. C.; Chang, A. H. H.; Kaiser, R. I. On the Formation of Amide Polymers Via Carbonyl-Amino Group Linkages in Energetically Processed Ices of Astrophysical Relevance. *Astrophys. J.* **2016**, *820*, 117.
- (275) Carlotti, M.; Johns, J. W. C.; Trombetti, A.  $\nu_5$  Fundamental Bands of  $N_2H_2$  and  $N_2D_2$ . *Can. J. Phys.* **1974**, *52*, 340–344.
- (276) Collin, R. L.; Lipscomb, W. N. The Crystal Structure of Hydrazine. *Acta Cryst.* **1951**, *4*, 10–14.
- (277) Kirchmeier, R. L.; Shreeve, J. M.; Verma, R. D. Fluorinated Compounds That Contain Catenated Oxygen, Sulfur or Nitrogen Atoms. *Coord. Chem. Rev.* **1992**, *112*, 169–213.
- (278) Krumm, B.; Vij, A.; Kirchmeier, R. J.; Shreeve, J. M.; Oberhammer, H. Hexakis(Trifluoromethyl)Tetrazane. *Angew. Chem. Int. Ed.* **1995**, *34*, 586–588.
- (279) Egger, N.; Hoesch, L.; Dreiding, A. S. 3,3-Dialkyltriazene-carboxylic Derivatives by Oxidative Hydro-Acyl-Elimination from 3,3-Dialkyltriazane-1,2-Dicarboxylic Derivatives. *Helv. Chim. Acta* **1983**, *66*, 1416–1426.
- (280) Kanzian, T.; Mayr, H. Electrophilic Reactivities of Azodicarboxylates. *Chem. Eur. J.* **2010**, *16*, 11670–11677.
- (281) Hope, P.; Wiles, L. A. Action of Sulphur Monochloride on 2-Acyl-1,1-Dimethylhydrazines: Formation of Tetrazans and Oxadiazolines. *J. Chem. Soc. C* **1967**, *1967*, 2636–2638.
- (282) Pirkle, W. H.; Gravel, P. L. Persistent Cyclic Diacylhydrazyl Radicals from Urazoles and Pyrazolidine-3,5-Diones. *J. Org. Chem.* **1978**, *43*, 808–815.

- (283) Martin, K. L.; Breton, G. W. Computational,  $^1\text{H}$  NMR, and X-ray structural studies on 1-arylurazole tetrazane dimers. *Acta Crystallogr. C* **2017**, 73, 660–666.
- (284) Christe, K. O.; Dixon, D. A.; Grant, D. J.; Haiges, R.; Tham, F. S.; Vij, A.; Vij, V.; Wang, T. H.; Wilson, W. W. Dinitrogen Difluoride Chemistry. Improved Syntheses of *cis*- and *trans*- $\text{N}_2\text{F}_2$ , Synthesis and Characterization of  $\text{N}_2\text{F}^+\text{Sn}_2\text{F}_9^-$ , Ordered Crystal Structure of  $\text{N}_2\text{F}^+\text{Sb}_2\text{F}_{11}^-$ , High-Level Electronic Structure Calculations of *cis*- $\text{N}_2\text{F}_2$ , *trans*- $\text{N}_2\text{F}_2$ ,  $\text{F}_2\text{N}=\text{N}$ , and  $\text{N}_2\text{F}^+$ , and Mechanism of the *trans-cis* Isomerization of  $\text{N}_2\text{F}_2$ . *Inorg. Chem.* **2010**, 49, 6823–6833.
- (285) Seidl, E. T.; Schaefer, H. F. Theoretical Studies of Oxygen Rings: Cyclotetraoxygen,  $\text{O}_4$ . *J. Chem. Phys.* **1988**, 88, 7043–7049.
- (286) Seidl, E. T.; Schaefer, H. F. Is There a Transition-State for the Unimolecular Dissociation of Cyclotetraoxygen ( $\text{O}_4$ ). *J. Chem. Phys.* **1992**, 96, 1176–1182.
- (287) Peterka, D. S.; Ahmed, M.; Suits, A. G.; Wilson, K. J.; Korkin, A.; Nooijen, M.; Bartlett, R. J. Unraveling the mysteries of metastable  $\text{O}_4^*$ . *J. Chem. Phys.* **1999**, 110, 6095–6098.
- (288) Politzer, P.; Lane, P. Kohn–Sham studies of oxygen systems. *Int. J. Quantum Chem.* **2000**, 77, 336–340.
- (289) Ramírez-Solís, A.; Jolibois, F.; Maron, L. *Ab initio* molecular dynamics studies on the ground singlet potential energy surface of the tetraoxygen molecule,  $\text{O}_4$ . *Chem. Phys. Lett.* **2010**, 485, 16–20.
- (290) Gadzhiev, O. B.; Ignatov, S. K.; Kulikov, M. Y.; Feigin, A. M.; Razuvaev, A. G.; Sennikov, P. G.; Schrems, O. Structure, Energy, and Vibrational Frequencies of Oxygen Allotropes  $\text{O}_n$  ( $n \leq 6$ ) in the Covalently Bound and van der Waals Forms: Ab Initio Study at the CCSD(T) Level. *J. Chem. Theory Comput.* **2013**, 9, 247–262.

- (291) Xie, Y. M.; Schaefer, H. F.; Jang, J. H.; Mhin, B. J.; Kim, H. S.; Yoon, C. W.; Kim, K. S. Sulfur Clusters: Structure, Infrared, and Raman Spectra of Cyclo-S<sub>6</sub> and Comparison with the Hypothetical Cyclo-O<sub>6</sub> Molecule. *Mol. Phys.* **1992**, *76*, 537–546.
- (292) Martins-Costa, M.; Anglada, J. M.; Ruiz-Lopez, M. F. Structure, Stability, and Dynamics of Hydrogen Polyoxides. *Int. J. Quantum Chem.* **2011**, *111*, 1543–1554.
- (293) Xu, X.; Goddard, W. A. Peroxone chemistry: Formation of H<sub>2</sub>O<sub>3</sub> and ring-(HO<sub>2</sub>)(HO<sub>3</sub>) from O<sub>3</sub>/H<sub>2</sub>O<sub>2</sub>. *Proc. Nat. Acad. Sci. USA* **2002**, *99*, 15308–15312.
- (294) Denis, P. A.; Ornellas, F. R. Theoretical Characterization of Hydrogen Polyoxides: HOOH, HOOOH, HOOOOH, and HOOO. *J. Phys. Chem. A* **2009**, *113*, 499–506.
- (295) Engdahl, A.; Nelander, B. The vibrational spectrum of H<sub>2</sub>O<sub>3</sub>. *Science* **2002**, *295*, 482–483.
- (296) Suma, K.; Sumiyoshi, Y.; Endo, Y. The rotational spectrum and structure of HOOOH. *J. Am. Chem. Soc.* **2005**, *127*, 14998–14999.
- (297) Levanov, A. V.; Sakharov, D. V.; Dashkova, A. V.; Antipenko, E. E.; Lunin, V. V. Synthesis of Hydrogen Polyoxides H<sub>2</sub>O<sub>4</sub> and H<sub>2</sub>O<sub>3</sub> and Their Characterization by Raman Spectroscopy. *Eur. J. Inorg. Chem.* **2011**, *2011*, 5144–5150.
- (298) Streng, A. G.; Grosse, A. V. Two New Fluorides of Oxygen O<sub>5</sub>F<sub>2</sub> and O<sub>6</sub>F<sub>2</sub>. *J. Am. Chem. Soc.* **1966**, *88*, 169–170.
- (299) Gorelli, F. A.; Ulivi, L.; Santoro, M.; Bini, R. The  $\epsilon$  phase of solid oxygen: Evidence of an O<sub>4</sub> molecule lattice. *Phys. Rev. Lett.* **1999**, *83*, 4093–4096.
- (300) Gorelli, F. A.; Ulivi, L.; Santoro, M.; Bini, R. Spectroscopic study of the  $\epsilon$  phase of solid oxygen. *Phys. Rev. B* **2001**, *63*, 104110.
- (301) Goncharov, A. F.; Gregoryanz, E.; Hemley, R. J.; Mao, H. K. Molecular character of the metallic high-pressure phase of oxygen. *Phys. Rev. B* **2003**, *68*, 100102.

- (302) Bartolomei, M.; Carmona-Novillo, E.; Hernández, M. I.; Pérez-Ríos, J.; Campos-Martínez, J.; Hernández-Lamonedá, R. Molecular oxygen tetramer (O<sub>2</sub>)<sub>4</sub>: Intermolecular interactions and implications for the  $\epsilon$  solid phase. *Phys. Rev. B* **2011**, *84*, 092105.
- (303) Goncharenko, I. N. Evidence for a magnetic collapse in the epsilon phase of solid oxygen. *Phys. Rev. Lett.* **2005**, *94*, 205701.
- (304) Hagiwara, M.; Ikeda, M.; Kida, T.; Matsuda, K.; Tadera, S.; Kyakuno, H.; Yanagi, K.; Maniwa, Y.; Okunishi, K. Haldane State Formed by Oxygen Molecules Encapsulated in Single-Walled Carbon Nanotubes. *J. Phys. Soc. Jpn.* **2014**, *83*, 113706.
- (305) Fujimori, T.; Morelos-Gomez, A.; Zhu, Z.; Muramatsu, H.; Futamura, R.; Urita, K.; Terrones, M.; Hayashi, T.; Endo, M.; Hong, S. Y.; Choi, Y. C.; Tománek, D.; Kaneko, K. Conducting linear chains of sulphur inside carbon nanotubes. *Nature Comm.* **2013**, *4*, 2162.

## Graphical TOC Entry

